ION IMPLANTED HOMOJUNCTION CRYSTALLINE SILICON SOLAR CELLS

A THESIS SUBMITTED TO
THE GRADUATE SCHOOL OF NATURAL AND APPLIED SCIENCES
OF
MIDDLE EAST TECHNICAL UNIVERSITY

BY

GENCE BEKTAŞ

IN PARTIAL FULFILLMENT OF THE REQUIREMENTS
FOR
THE DEGREE OF DOCTOR OF PHILOSOPHY
IN
MICRO AND NANOTECHNOLOGY

JUNE 2022

Approval of the thesis:

ION IMPLANTED HOMOJUNCTION CRYSTALLINE SILICON SOLAR CELLS

submitted by **GENCE BEKTAŞ** in partial fulfillment of the requirements for the degree of **Doctor of Philosophy in Micro and Nanotechnology, Middle East Technical University** by,

Prof. Dr. Halil Kalıpçılar
Dean, Graduate School of **Natural and Applied Sciences**

Prof. Dr. Deniz Üner
Head of the Department, **Micro and Nanotechnology**

Prof. Dr. Raşit Turan
Supervisor, **Physics, METU**

Prof. Dr. H. Emrah Ünalan
Co-Supervisor, **Metallurgical and Materials Eng., METU**

Examining Committee Members:

Assoc. Prof. Dr. Selçuk Yerci
Electrical and Electronics Eng., METU

Prof. Dr. Raşit Turan
Physics, METU

Prof. Dr. Hakan Karaağaç
Physics Eng., İstanbul Technical University

Assoc. Prof. Dr. Mustafa Kulakcı
Physics, Eskişehir Technical University

Assist. Prof. Dr. Bilge İmer
Metallurgical and Materials Eng., METU

Date: 22.06.2022

I hereby declare that all information in this document has been obtained and presented in accordance with academic rules and ethical conduct. I also declare that, as required by these rules and conduct, I have fully cited and referenced all material and results that are not original to this work.

Name, Surname: Gence Bektaş

Signature :

ABSTRACT

ION IMPLANTED HOMOJUNCTION CRYSTALLINE SILICON SOLAR CELLS

Bektaş, Gence
Doctor of Philosophy, Micro and Nanotechnology
Supervisor: Prof. Dr. Raşit Turan
Co-Supervisor: Prof. Dr. H. Emrah Ünalan

June 2022, 135 pages

Process simplification is one of the requirements to reduce the workload and cost of solar cell manufacturing, especially for complex designs. In particular, the application of the ion implantation method in patterned and single side doping processes, which are the bottlenecks of the diffusion method, brings many conveniences in cell production. Flexibility in the selection of masking material during doping is another important factor that makes the ion implantation method attractive. Moreover, by varying the parameters of the ion implantation and a subsequent annealing process the desired profile can be formed for both p and n doping in silicon (Si) wafers to form an emitter and back surface field. In this thesis, we investigate the ion implantation along with the subsequent activation processes and apply them to the fabrication of various Si solar cells such as passivated emitter and rear contact (PERC), passivated emitter and rear totally diffused (PERT), and interdigitated back contact (IBC). In this context, we take advantage of its capability for single side doping, which eliminates additional processes such as single side etching or deposition and removal of a mask layer in the fabrication of PERC and PERT solar cells. In addition, we demonstrate an easy-to-apply IBC process flow with the use of hard masks in the ion implantation process for patterned doping, which is very complex for the diffusion method. Furthermore, ion implantation can be used together with the diffusion method in the manufacturing of solar cells with high efficiency and simplified process flow. By applying the optimized and simple manufacturing methods, we achieve 20.25%, 20.54% and 15.60% efficiencies for PERC, PERT and IBC solar cells, respectively.

Keywords: Ion-implantation, silicon solar cell, PERC, PERT, IBC

ÖZ

İYON İMPLANTE EDİLMİŞ HOMOEKLEM KRİSTAL SİLİSYUM GÜNEŞ HÜCRELERİ

Bektaş, Gence
Doktora, Mikro ve Nanoteknoloji
Tez Yöneticisi: Prof. Dr. Raşit Turan
Ortak Tez Yöneticisi: Prof. Dr. H. Emrah Ünalan

Haziran 2022, 135 sayfa

Proses basitleştirme, özellikle karmaşık tasarımlar için güneş hücresi üretiminde iş yükünü ve maliyetini azaltmak için gerekliliklerden biridir. Özellikle difüzyon yönteminin darboğazlarından olan desenli ve tek taraflı katkılama işlemlerinde iyon implant yönteminin uygulanması hücre üretiminde birçok kolaylığı beraberinde getirmektedir. Katkılama sırasında maskeleme malzemesinin seçimindeki esneklik, iyon implantasyon yöntemini arzu edilir kılan önemli bir faktördür. Ayrıca, iyon implantasyon ve müteakip tavlama proseslerinin parametrelerinin değiştirilmesi ile, emitör ve arka yüzey alanı (BSF) oluşturmak üzere silisyum (Si) dilimlerinde hem p hem de n katkılama için istenen profil oluşturulabilir. Bu tezde, implantasyon ve katkı aktivasyon işlemlerini çalışıyoruz ve bunları PERC, PERT ve IBC gibi çeşitli Si güneş hücrelerinin üretiminde uyguluyoruz. Bu bağlamda, PERC ve PERT güneş hücrelerinin üretiminde iyon ekme yönteminin tek taraflı aşındırma veya maske katmanının büyütülmesi ve sökülmesi gibi ek işlemleri ortadan kaldıran tek taraflı katkılama özelliğinden yararlanıyoruz. Ek olarak, difüzyon yöntemi ile çok karmaşlık olan desenli katkılama için iyon implantasyon sırasında sert maskelerin kullanımıyla uygulanması kolay IBC üretim akışlarını gösteriyoruz. Ayrıca iyon implantasyonu, yüksek verimli ve basitleştirilmiş işlem akışına sahip güneş hücrelerinin üretiminde difüzyon yöntemi ile birlikte kullanılabilir. Optimize edilmiş ve basit üretim yöntemlerini uygulayarak PERC, PERT ve IBC güneş hücreleri için sırasıyla %20.25, %20.54 ve %15.60 verimlilik sunuyoruz.

Anahtar Kelimeler: iyon implantasyon, silisyum güneş hücresi, PERC, PERT, IBC

Dedicated to my family

ACKNOWLEDGMENTS

I would like to first express my deepest gratitude to Prof. Dr. Raşit Turan for his supervision of my research. He has always been encouraging in this long journey.

In this endeavor, we have overcome many challenges thanks to my labmates, Ahmet Emin Keçeci, Hasan Asav, Hasan Hüseyin Canar, Selin Seyrek, Sümeyye Koçak Bütüner. I would like to convey my deepest gratitude for their fruitful discussion and cooperation during the fabrication and characterization of the samples.

I am very grateful to all the technical staff of ODTÜ-GÜNAM, especially Batuhan Taş, Murat Aynacıoğlu, and Furkan Çiçek, for their endless support in the processes and technical issues. I would like to thank Mehmetcan Karaman for his great effort to solve the power supply problems of the ion implanter system and enable me to complete the last experiments.

I would like to thank my colleagues Dr. Bülent Arıkan, Ayşen Elşen Aydın, Elif Sarıgül Duman, Sercan Arslan, Vahdet Özyahni that we work together in ODTÜ-GÜNAM Photovoltaic Line (GPVL). I am also thankful to Dr. Fırat Es, Emel Semiz, Gamze Kökbudak, Ezgi Genç, Efe Orhan, Dr. Gülsen Baytemir and Ege Özmen who we worked together in the past in GPVL.

I would like to extend my sincere thanks to Assoc. Prof. Dr. Selçuk Yerci and Assoc. Prof. Dr. Mustafa Kulakcı, who made invaluable contributions to this work at each thesis monitoring committee meeting, and Prof. Dr. Hakan Karaağaç and Assist. Prof. Dr. Bilge İmer, who were on the jury evaluating my thesis.

Finally, I would like to thank my family for their unending support. I am deeply indebted to them for being with me in all my decisions, both in my private and professional life.

This work was partially funded by Scientific and Technological Research Council of Turkey (TÜBİTAK) under grant numbers 118E171 and 20AG002.

TABLE OF CONTENTS

CHAPTERS

LIST OF TABLES

LIST OF FIGURES

CHAPTER 1

INTRODUCTION

With population growth and industrialization, the current sources are not sufficient to meet the increasing energy demand. The increase by 2 billion in the human population in only one generation gives a signal of raising the energy demand in the near future, as well. Since the economical growth of the countries is proportional to their energy demand, all the developing countries are seeking to increase their energy capacity however they are limited by the lack of energy reserves. Besides, they should also take into account the emission of various gases from today's dominating nonrenewable energy sources such as fossil fuels due to environmental issues. All this necessitates the development of reliable, everlasting, and cost-effective renewable energy sources. Solar energy, especially photovoltaic, is the best candidate to permanently solve the energy crisis of the future without harming our ecosystem [1]. This is because the sun is an infinite energy source that can be utilized by various means such as thermal and photovoltaic systems. The solar thermal systems heat the air, water, or any liquid. The produced steam is converted into mechanical energy in a turbine to generate electricity. The photovoltaic systems on the other hand directly convert sunlight into electricity. The power conversion efficiency of solar cells has already reached good levels and the silicon based photovoltaic industry has also caught a good trend. The researchers now work on cutting edge solar cell designs for further improvements. However, the main concerns for the industrialization of such advanced solar cell designs are the process complexities and manufacturing cost. Recently, there has been a lot of progress on this by developing alternative materials and process methods, which shows that silicon solar cells operating with efficiency close to theoretical limits will be produced with lower cost and workload in the near future.

1.1 Historical Development of Silicon Solar Cells

The first silicon based solar cell was reported by Ohl in 1941 using melt grown junctions. In 1952, the silicon solar cell having a junction created by helium ion bombardment was a huge step forward since these cells demonstrated by Kingsburg and Ohl showed a good spectral response. The evolution of the solar cell efficiencies increased with the development of diffused junctions and 4.5% and 6% efficiencies were announced by Bell Laboratories in 1953 and 1954, respectively. 10% efficiency was achieved after 18 months. In 1961, a new record efficiency of 14.5% cell efficiency, under AM1.5 conditions and at a temperature of 25°C, was measured on a commercial solar cell with the phosphorus doped substrate. Similar cell efficiency with a higher radiation tolerance in space was obtained on the boron-doped substrates in 1970. Despite the minor improvements in the following years, the 18% efficiency, which was measured on the cell fabricated by UNSW MINP, did not appear until 1983. 20% efficiency was exceeded in 1985. The passivated emitter and rear contact (PERC) solar cell, which is the dominating cell type in the photovoltaic industry today, showed 22.6% efficiency in 1989. In 1999, 25% was measured on the passivated emitter and rear locally diffused (PERL) cell, which is one of the advanced cell designs with relatively complex process steps [2]. Today, various advanced silicon solar cell concepts such as PERL, PERT, and IBC along with different designs with passivating contacts and bifacial approaches extensively studied by many research groups and companies. Additionally, the tandem structures composed of silicon and another type of solar cell with different absorber materials are also the focus of researchers to go beyond the theoretical limit by benefiting a wider range of the solar spectrum.

1.2 Application of Ion Implantation for Silicon Solar Cell Fabrication

In the fabrication of silicon solar cells, doping is a critical process step for junction formation such as emitter and back surface field. Doping can be carried out by various methods but the diffusion furnace is the most common one applied in the industry today. However, diffusion furnaces are insufficient in the fabrication of advanced silicon cells since they cannot perform single side and local doping without additional process steps such as deposition and patterning and removal of protection layers. Additionally, the high-temperature requirement for doping processes limits the use of protection materials as masking layers. On the other hand, the ion implantation method provides not only a controllable doping profile but also a single side and patterned doping with a variety of material selections for masking. The application of ion implantation to solar cell technology dates back to the 1980s. Edward et al. have utilized the ion implantation method to fabricate various p and n-type silicon solar cells in a study where the champion has shown an efficiency of 15% under AM1 conditions [3]. In 2011, 156 mm x 156 mm Al-BSF solar cells with selective emitters were produced by an ion implanter system that is capable of processing 1000 wafers per hour. Fabrication of 18.5% efficient solar cells with the size of 156 mm x 156 mm by using the ion-implanter system with such a high throughput has paved the way for the utilization of the ion implantation method in industrial photovoltaic lines [4]. Today, this method is applied for the fabrication of various cell structures such as PERC, PERT, IBC, and passivating contacts since it allows process simplification [5][6][7][8].

1.3 Organization of This Thesis

In this Ph.D. study, we have carried out a comprehensive study on the application of the ion implantation method in various crystalline Si solar cell architectures. Chapter 2 covers the theory of n and p-type doping, diffusion, and ion implantation method. The fundamental operation mechanism of homojunction Si solar cells along with the solar cell parameters are given in this chapter, as well.

In Chapter 3, the fabrication and characterization methods used in this study are briefly explained. In Chapters 4, 5, and 6, we present the ion-implanted PERC, PERT and IBC solar cells, respectively. In this context, the literature review and our experimental findings for the interested solar cell types are extensively discussed.

CHAPTER 2

FUNDAMENTALS OF DOPING, ION IMPLANTATION AND SOLAR CELLS

In this chapter, the fundamentals of semiconductor doping, ion implantation process and silicon solar cells are extensively covered. In Section 2.1, the importance of the doping process in semiconductor technology and general p and n-type dopants, which are boron and phosphorus atoms, are discussed. The physical reason behind the variation of electrical characteristics of the semiconductor with doping is also explained. In Section 2.2, the doping mechanism by the ion implantation method and subsequent defects formed by the processes are described. In Section 2.3, the diffusion of the atoms in the semiconductor is explained by continuum theory and atomic diffusion approaches. Finally, the basic operation mechanism of crystalline homojunction silicon solar cells is given in Section 2.4.

2.1 Semiconductor Doping

Doping in semiconductor technology is applied to change the electrical properties of the materials by introducing impurity atoms into them. The number of electrons in the outer shell of the impurity atoms defines the type of doping as either p-type or n-type. For silicon, the atoms in Group V such as phosphorus, arsenic, and antimony are used as n-type dopants to create free electrons to move in the silicon lattice. A dopant atom from the Group V elements is named a donor atom due to its electron donation. On the other hand, Group III elements such as boron, aluminum, gallium and indium with missing 4th valance electron in their outer shells are used as p-type dopants to create free holes. A dopant atom from the Group III elements is named an acceptor atom [9].

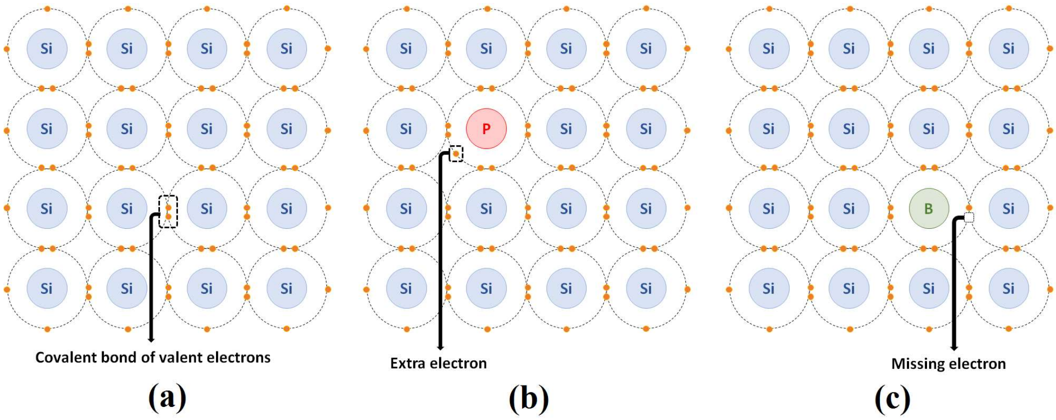

Figure 2.1 Schematic representation of covalent bond of (a) pure silicon, (b) phosphorus doped silicon, (c) boron doped silicon (Adapted from [9]).

The electronic structure of silicon is characterized by the concentration and type of dopants in it. The total resistivity (**ρ**) of the material is given by the sum of electron and hole conductivity.

$$\rho = \frac{1}{q\mu_e n + q\mu_h p} \tag{2.1}$$

where n and p are the carrier concentration and μ_e and μ_h are the mobility for electron and hole, respectively, and q is the elementary charge. μ_e and μ_h depend on doping, temperature, and electric field in semiconductors.

The number of electrons in conduction band (CB) and holes in valance band (VB) are determined by density of states. In equilibrium condition, the number of electrons in the conduction band is given by

$$n = \int_{E_C}^{\infty} N(E)F(E)dE \tag{2.2}$$

where $N(E)$: the density of states, $F(E)$: Fermi-Dirac probability function, E_C: energy of the conduction band edge.

The number of holes in the valence band is defined as

$$p = \int_{-\infty}^{E_V} N(E)(1 - F(E))dE \tag{2.3}$$

where E_V: energy of the valance band edge.

In a system with discrete energy levels, the probability of an electron to occupy any energy level, E, is calculated by Fermi-Dirac probability function:

$$F(E) = \frac{1}{1 + \exp(\frac{E - E_F}{k_B T})} \tag{2.4}$$

where k_B: Boltzmann constant, and T: temperature.

Besides the Fermi-Dirac probability function, it is necessary to know the number and position of allowed energy levels to determine n and p. According to the quantum mechanical approach, energy levels in a crystal are not continuous and no two electrons can occupy exactly the energy levels. In other words, each electron in a system should have different quantum numbers.

An approximate expression for the allowed energy levels for electrons in the conduction band at an energy level, E:

$$N(E) = \frac{4\pi}{h^3}(m_e^*)^{3/2}(E - E_C)^{1/2} \text{ (for } E > E_C) \tag{2.5}$$

An approximate expression for the allowed energy levels for holes in the valance band at an energy level, E:

$$N(E) = \frac{4\pi}{h^3}(m_h^*)^{3/2}(E_V - E)^{1/2} \text{ (for } E < E_V) \tag{2.6}$$

m_e^* and m_h^* are effective masses of the electron and hole, respectively. The effective masses are utilized since the electrons and holes are not in free space but located in a crystal.

In process physics and device physics, the main concern is the total number of electrons in the conduction band (n) and the total number of holes (p) in the valence band. If the Fermi level is located at least a few $k_B T$ away from the band edges and any other allowed energy levels in the band gap, the Fermi-Dirac distribution function can be approximated by Boltzmann distribution, and the concentration of electron in the conduction band and holes in valance band can be calculated as follows;

$$n = \int_{E_C}^{\infty} N(E)F(E)dE = N_C \exp(-\frac{E_C - E_F}{k_B T}) \quad (2.7)$$

$$p = \int_{-\infty}^{E_V} N(E)(1 - F(E))dE = N_V \exp(-\frac{E_F - E_V}{k_B T}) \quad (2.8)$$

where

$$N_C = 2(\frac{2\pi m_e^* k_B T}{h^2})^{\frac{3}{2}} \quad and\ N_V = 2(\frac{2\pi m_h^* k_B T}{h^2})^{\frac{3}{2}} \quad (2.9)$$

N_C and N_V denote the effective densities of the states in the conduction and valance bands, and they are 2.8x10^{19} cm^{-3} and 1.04x10^{19} cm^{-3}, respectively, for silicon at room temperature.

For an undoped material, the intrinsic charge carrier concentration (n_i) is defined

$$n = p = n_i \quad (2.10)$$

n_i for Si at room temperature is 1.45x10^{10} cm^{-3}.

The law of mass action holds for both doped and undoped material and given as the following;

$$n.p = {n_i}^2 \quad (2.11)$$

If Eqs. (2.7), (2.8) and (2.11) are combined, the following expression can be obtained

$$n.p = {n_i}^2 = N_C N_V \exp(-\frac{E_G}{k_B T}) \quad (2.12)$$

where E_G is energy band gap and given as

$$E_G = E_C - E_V \quad (2.13)$$

If Eqs. (2.7), (2.8) and (2.12) are combined, n and p are expressed in a more convenient form as

$$n = n_i \exp(\frac{E_F - E_i}{k_B T}) \qquad (2.14)$$

$$p = n_i \exp(\frac{E_i - E_F}{k_B T}) \qquad (2.15)$$

According to Eqs. (2.14) and (2.15), as the electron concentration increases and hole concentration decreases, E_F moves above E_i. Similarly, as the hole concentration increases and electron concentration decreases E_F moves below E_i.

The equilibrium concentrations of electrons and holes in the semiconductor vary with dopant concentration. In the case of n-type doping, $n \approx N_D$ if $N_D \gg n_i$. Similarly, $p \approx N_A$ if $N_A \gg n_i$, where N_A : n-type dopant concentration and N_D : p-type dopant concentration [9][10].

The E_C, E_V, E_F and E_g of n and p-type materials are illustrated in *Figure 2.2*.

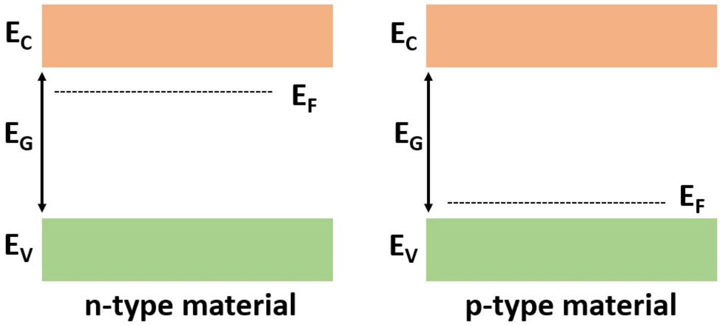

Figure 2.2 Schematic illustration of E_C, E_V, E_F and E_g of n-type (left) and p-type (right) semiconductor materials (Adapted from [11])

2.2 Doping by Ion Implantation Method

Ion implantation has played a very critical role in the rapid development of integrated circuit (IC) technology. This method provides a controllable doping process in concentration and depth, which defines the characteristics of the p-n junction. Additionally, it can simplify the complexity of device fabrication since it enables single side and patterned doping and does not require an additional process for deposition of the protection layer or etching process for doping of a patterned region without diffusion under the mask. With all these advantages, the ion implantation method has attracted an attention of photovoltaics researchers, too. This section discusses the interaction of ions with the semiconductor material and types of implantation defects.

2.2.1 Ion Stopping Mechanism

High energy ions implanted into a solid collide and interact with the nuclei and the electrons during the penetration in the lattice, which causes energy loss for ions. The energy loss depends on not only the mass, nuclear charge, and energy of the implanted ions but also the nuclear charge and the atomic density of the solid material. The energy losses can be classified under two mechanisms:

Elastic Nuclear Interaction: Energy of incoming ion is transferred to the solid material.

Inelastic Interaction: The incoming particle can either excite the electrons of host materials or ionize them. Another possibility is that energetic ions can result in a collective electron motion or lattice vibrations through plasmons and phonons in the solid material [12].

2.2.2 Ion Implantation Defects

During an ion implantation process, structural defects occur in the lattice of the solid material since the incoming ions transfer their energies to the host atoms and displace them from their ordered lattice sites. The first atom kicked from its site by the energetic ions is called the primary knock-on atom. Depending on the energy of incoming ions, the primary knock-on atom may continue to displace other atoms in the lattice and result in an atomic collision cascade, which will cease after a certain time. The host material will end up with various types of defects caused by energetic ions moving in the lattice. There are several parameters, which are related to the host material and the implantation process itself, determining the number of defects and lattice disorders caused by the ion implantation process. Firstly, the defects depend on the radiation hardness of the lattice which is specific to the solid material itself. If the threshold energy of the displacement for the host material is low, the induced damage will be heavier. Secondly, ion irradiation parameters such as energy and mass of the ions, ion current density, implantation angle, implantation fluence, and substrate temperature are highly effective in the amount and degree of the defect [13][14].

Implantation induced defects in silicon can be in different forms as depicted in *Figure 2.3*. The letter represents the host atom (Si), impurity (I), or vacancy (V); and the subscript represents it the defect is interstitial (I) or substitutional (S).

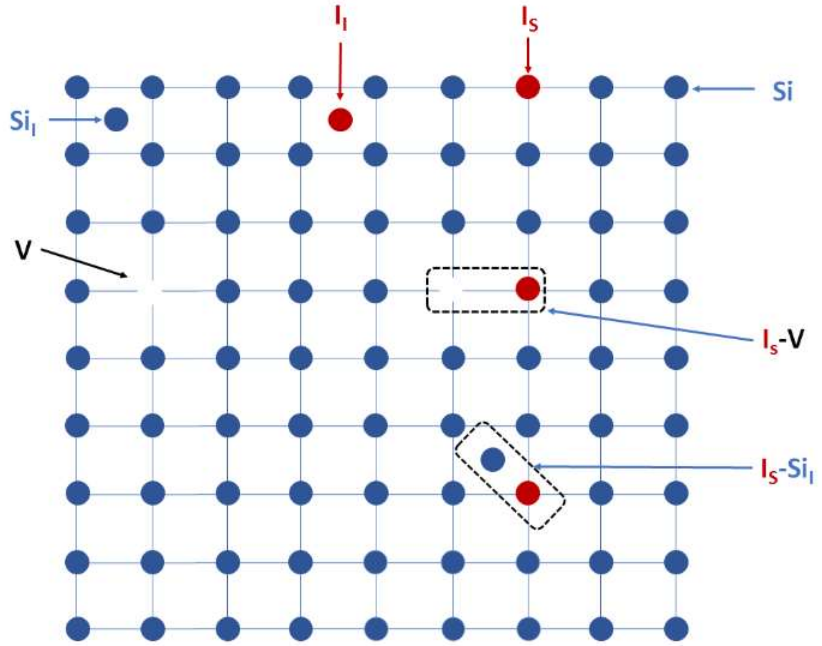

Figure 2.3 A schematic representation of point defects: a vacancy (V), a self-interstitial (Si_I), a substitutional (I_S) and an interstitial impurity (I_I), an impurity-vacancy (I_S-V) and an impurity-self-interstitial (I_S-Si_I) complex. Host atoms, impurities, and vacancies are represented by blue, red, and black colors, respectively. (Adapted from[13])

Post implant annealing process conditions are also effective in the formation of defects of various types. Interstitials and vacancies, which are formed during ion implantation, tend to recombine during the annealing process and condense to create defects, especially the extended types, which will be discussed in sections 2.2.2.2, 2.2.2.3, and 2.2.2.4. The extended defect types formed in the lattice strongly depend on the annealing temperature of implanted dopants. The point defects created by implantation are responsible for the formation of {311} rod-like defects (planar), which eventually dissolve to form dislocation loops (line defect) at higher annealing temperature and time [15]. For instance, {311} rod-like defects typically occur at temperatures of around 600-700°C and they disappear at higher temperatures. At an annealing temperature of around 900-1000°C, dislocation loops of two types, perfect dislocation loops (PDLs) and faulted dislocation loops (FDLs) are more likely to be observed [16]. It has been discussed that the dislocation loops, which are the source for enhanced junction leakage, are formed by dissolution of {311} rod-like defects as they are annealed above 800 °C [15]. On the other hand, there are two mechanisms speculated for the source of extended {311} rod-like defects:

1. interstitial chains, which are grown by interstitial clusters, elongate along <011> direction.
2. Interstitial chains elongated in <011> direction capture interstitials along <233> direction and widen [17].

2.2.2.1 Zero-dimensional defects - Point Defects:

Point defects such as vacancy (V) and interstitial (I_I and Si_I) are defined as the change in the periodicity of the lattice that is resulted from a single point. They can be either native or impurity related defects as shown in *Figure 2.3*. As its name suggests, vacancy is an empty lattice site in which an atom is supposed to reside. On the other hand, an interstitial is an unexpected atom residing in between two atomic sites. Interstitial atoms can be impurities (I_I), in which an impurity atom (I) is involved, or self-interstitial atoms (Si_I), in which the host atom is involved. When the host atom leaves its site to a vacancy and resides as an interstitial near the vacancy, then this combination is called the Frenkel pair. On the other hand, if the atom vacates its site and moves to the surface of the crystal material then it is called a Schottky defect.

Moreover, an impurity atom may replace the host atom from its atomic site, and it is named as substitutional impurity (I_S). The combination of an impurity atom and vacancy (I-V), where vacancy is next to an impurity atom, is also in the category of point defect. As a last configuration, the impurity atom can stay next to self-interstitial atom ($I\text{-}Si_I$).

2.2.2.2 One dimensional (line) defect – Dislocations

Ion implantation and subsequent annealing process may leave some extended defects, so-called line defects (dislocations) that occur in two different forms as seen in Figure 2.3. Dislocations, which act as electrical defects, are not desired in the silicon crystal since they act as sinks for metallic impurities. Additionally, they interrupt the diffusion process.

a) Edge dislocations:

Edge dislocation results from an additional row of atoms that are normally not supposed to settle into that part of the lattice. This unnatural condition creates compressive stress on the extra atoms in the lattice, whereas the atoms with the correct atoms sequence are subjected to tensile stress.

b) Screw dislocations:

Screw dislocation is formed due to the displacement of atoms in one plane of the crystal named the slip plane. The boundary between the slipped and normal atoms positioned in expected atomic sites is called the dislocation line.

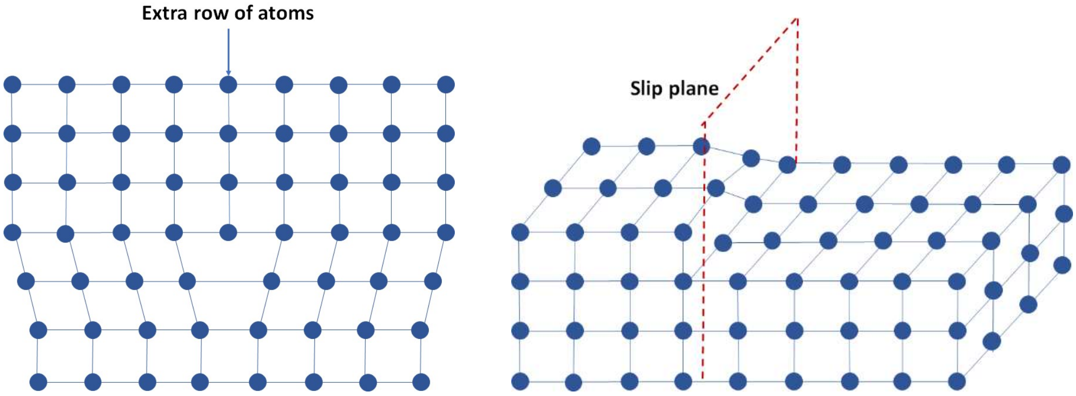

Figure 2.4 A schematic representation of linear defects: Edge dislocation (left) and screw dislocation (right) (Adapted from [18])

2.2.2.3 Two-dimensional (planar) defect

Two dimensional defects can occur in two forms named stacking faults and grain boundaries.

Grain Boundaries:

The grain boundary is the interface of crystallites (grains) with different atomic orientations. The misorientation of the gains determines the structure of the boundary structure.

Stacking Faults:

Stacking faults, on the other hand, is the disturbance of periodicity of the stacking planes of atoms in a lattice, and they may occur in three different ways. The first type is the extrinsic stacking fault in which an extra plane of atoms is inserted into stacking planes. The second one is the intrinsic stacking fault in which one plane of atoms is removed. The last one is the twin boundary that separates two volumes of crystal that are mirror images of each other. Stacking faults may form during crystal growth or evolve from other defects. When impurity atoms are located on a stacking fault, it becomes electrically active, which results in an increase in the reverse bias saturation current in the p-n junction.

Figure 2.5 illustrates two ABCABC face-centered cubic (fcc) stacking of planes; one with a perfect crystal structure (left) and one with a stacking fault (right), which is created by removing one plane of atoms.

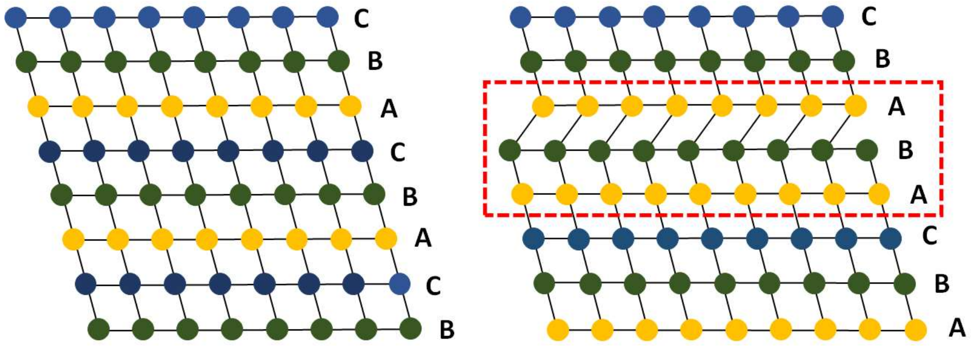

Figure 2.5 A schematic representation of a perfect planar stacking (left) with ABCABC sequence and Stacking fault (right) in fcc structure (Adapted from[19])

2.2.2.4 Three dimensional (volume) defects

Volume defects are three dimensional aggregates of atoms or vacancies and form due to the solid solubility limit of impurities. They can be either voids or precipitates which generate stress on the lattice and result in the formation of dislocations [20]. Boron (B) clustering in B-implanted silicon wafers is a typical three-dimensional defect type which requires a high thermal budget for its dissolution [21].

2.3 Diffusion

Diffusion within the crystalline solids can be defined as the spread of dopants due to thermal agitation. Point defects can be considered vehicles for the diffusion of atoms since they can migrate through the crystal. The existence of point defects disturbs the periodicity of mass and charge of periodicity of a perfect crystal. In semiconductors, point defects can be in a neutral or ionized state depending on the Fermi level position since point defects create energy levels within the bandgap [22]. There are various methods to introduce the impurity atoms into a semiconductor:

a) diffusion from a chemical source at high temperature,

b) diffusion from a doped oxide source,

c) diffusion from an ion implanted layer [23].

One of the aims of diffusion studies is to develop models from experimental data to calculate the electrical properties of doped semiconductors from the predicted doping profile of a given process parameter. In this sense, there are two major approaches:

- The continuum theory of Fick's simple diffusion equation (a second order partial differential equation)
- The atomistic theory

2.3.1 The continuum Theory of Fick's Simple Diffusion Equation

According to the continuum theory, diffusion can be explained from the solution of Fick's diffusion equation if the appropriate boundary conditions and diffusion constant (diffusivity), which can be acquired from experimental measurements such as surface concentration, junction depth, and doping profiles, are provided. If the impurity level is low, Fick's diffusion equation is well enough to approximate the doping profile since there is no need to know the detailed atomic movement at low doping concentrations. However, when doping concentration is high, diffusion profiles obtained by Fick's simple diffusion equation deviate from the experimental results. In this case, concentration-dependent diffusion constants are applied to make an accurate prediction of the doping profile. For the determination of concentration-dependent diffusivities, Boltzmann-Matano analysis is applied [23].

The content of this section is mainly based on the textbook of Helmut Mehrer [22] and VLSI Technology [23].

2.3.1.1 Fick's First Law:

The mobility of an atom, defect, or impurity in a crystal lattice is defined by the diffusion coefficient (diffusivity), D. The flux of diffusing particles for an isotropic medium in one dimension can be expressed by Fick's first law:

$$J_x = -D\frac{\partial C}{\partial x} \tag{2.16}$$

where J_x: the flux of particles (diffusion flux), C: concentration, and D: diffusion constant of species. The negative sign in the equation shows that the diffusion flux and concentration gradient are in the opposite direction. For any isotropic medium, diffusion flux and concentration gradient are antiparallel.

Einstein's relation relates diffusivity (D) to and mobility (μ) as the following:

$$D = \frac{kT}{q}\mu \tag{2.17}$$

where k is Boltzman constant, and T is temperature.

Einstein's relation shows that the kinetic energy, thus mobility and diffusivity, of dopants increases with temperature. The increase of D usually obeys the Arrhenius relation:

$$D = D_o \exp\left(-\frac{E_A}{k_B T}\right) \tag{2.18}$$

where D_o and E_A are atom or defect dependent parameters. E_A is known as the activation energy of the diffusion process and D_o is temperature independent pre-exponential function.

The diffusion flux is defined as number of particles (or moles) traversing a unit area per unit time. Concentration is the number of particles per unit volume. Based on the definition of parameters in Fick's law, the unit of diffusion constant is [cm^{2}s^{-1}] or [m^{2}s^{-1}]. Fick's first law can be written using vector notation to express three dimensions as follows:

$$J = -D\nabla C \tag{2.19}$$

The nabla symbol, ∇, is used to produce the concentration gradient on the scalar concentration field, C(x,y,z,t). The vector of the diffusion flux, J, is in the opposite direction of ∇C.

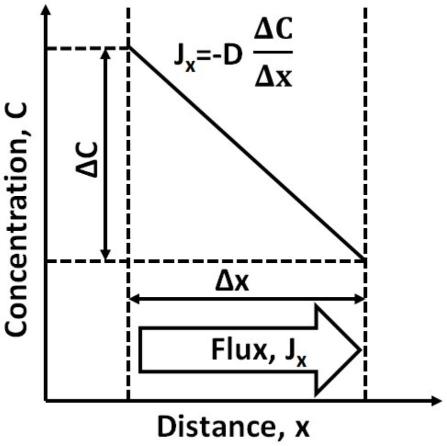

Figure 2.6 Illustration of Fick's first law (Adapted from [22]).

Fick's first law can be analogized to Fourier's law of heat flow and Ohm's law. While Fick's law describes the transport of particles, Fourier's law describes the transport of heat, and Ohm's law the transport of electric charge.

- Fourier's law of heat flow;

$$J_q = -\kappa\nabla T \tag{2.20}$$

Jq: the flux of heat, T: temperature field, κ: thermal conductivity

- Ohm's law:

$$J_e = -\sigma\nabla V \tag{2.21}$$

J_e: electric current density, V: electrostatic potential, σ: electrical conductivity.

2.3.1.2 Continuity Equation:

If diffusing particles, whose concentrations are usually conserved in a diffusion process, obey a conservation law of an equation of continuity, then they can be formulated. In a diffusion process, the flux entering, leaving, and lost can be expressed by the following equation:

$$\text{Inflow - outflow = accumulation (or loss) rate} \tag{2.22}$$

Let us define an arbitrary point, P, positioned at (x, y, z) in a test volume with the sizes of Δx, Δy, and Δz in three dimensions and diffusion flux J with the components of J_x, J_y, and J_z, across the test volume.

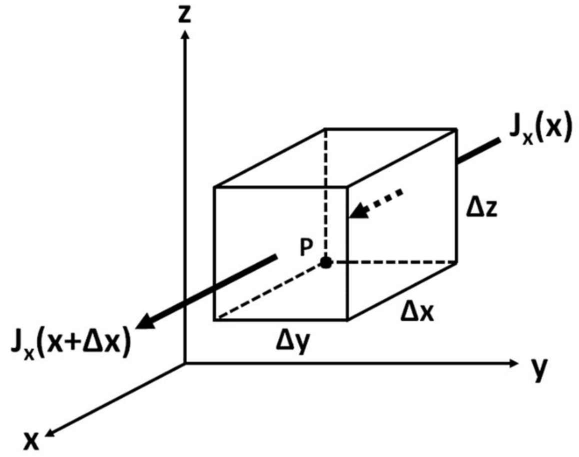

Figure 2.7 Illustration of infinitesimal test volume. J_x component of the diffusion flux entering and leaving the medium. J_y and J_z components can be analogized to J_x (Adapted from [22]).

The three components of flux in the test volume can be substituted in the Equation (2.22) as the following:

$[J_x(P) - J_x(P+\Delta x)]\Delta y\Delta z + J_y(P) - [J_y(P+\Delta y)]\Delta x\Delta z + [J_z(P) - J_z(P+\Delta z)]\Delta x\Delta y =$ accumulation (or loss) rate.

If Taylor expansions of the flux components is used to replace square brackets by $\Delta x \partial J_x/\partial x$, $\Delta y \partial J_y/\partial y$, and $\Delta z \partial J_z/\partial z$, respectively, it yields to

$$-\left[\frac{\partial J_x}{\partial x}+\frac{\partial J_y}{\partial y}+\frac{\partial J_z}{\partial z}\right]\Delta x \Delta y \Delta z=\frac{\partial C}{\partial t}\Delta x \Delta y \Delta z \tag{2.23}$$

The right-hand side of the equation stands for the loss rate. Vector operation divergence, ∇, can be used to write the equation in a compact form which is named as continuity equation:

$$-\nabla . \mathrm{J}=\frac{\partial C}{\partial t} \tag{2.24}$$

2.3.1.3 Fick's Second Law- Diffusion Equation:

Simple diffusion equation (Fick's second law) can be obtained by combining Fick's first law (2.19) and continuity equation (2.24):

$$\frac{\partial C}{\partial t}=\nabla .(\mathrm{D} \nabla \mathrm{C}) \tag{2.25}$$

The diffusion equation is non-linear second order partial differential equation if D is concentration dependent. In this case, it is not possible to solve it by Fick's simple diffusion equation. If D is independent of concentration, which is possible at low impurity concentrations, then Equation (2.25) simplifies to

$$\frac{\partial C}{\partial t}=\mathrm{D} \Delta \mathrm{C} \tag{2.26}$$

Equation (2.26) is a linear second order partial differential equations for the concentration field C(x,y,z,t) where Δ is the Laplace operator. This form of diffusion equation can be solved if the boundary and initial conditions are defined.

Note: The Laplace operator, Δ, is a scalar operator which is the dot product (inner product) of two gradient vector operators:

$$\nabla.\nabla = \nabla^2 = \left[\frac{\partial}{\partial x_1}, \dots, \frac{\partial}{\partial x_N}\right] \begin{bmatrix} \frac{\partial}{\partial x_1} \\ \cdot \\ \cdot \\ \cdot \\ \frac{\partial}{\partial x_N} \end{bmatrix} = \sum_{n=1}^{N} \frac{\partial^2}{\partial x_n^2} \tag{2.27}$$

Diffusion equation will be written in Cartesian coordinates (x, y, z) within the scope of this study, but it can be also written in cylindrical coordinates (r, Θ, z) and spherical coordinates (r, Θ, ϕ).

Experimental diffusion studies benefit from special symmetries on the diffusion field since they are helpful for analytical solutions. These special symmetries for Cartesian coordinates can be defined as follows:

Linear flow in x direction, if $\partial/\partial y = \partial/\partial z = 0$;

$$\frac{\partial C}{\partial t} = D(\frac{\partial^2 C}{\partial x^2})$$

Note: The equations mentioned above are all valid for an isotropic media. If the media is not isotropic such as non-cubic single crystals, composite materials, textured polycrystals, and decagonal quasicrystals, diffusivity will change in each direction. For such unisotropic medias, one should define D matrix for each flux component:

$$\begin{pmatrix} D_1 & 0 & 0 \\ 0 & D_2 & 0 \\ 0 & 0 & D_2 \end{pmatrix}$$

$$J_1 = D_1 \frac{\partial C}{\partial x_1}, \qquad J_2 = D_2 \frac{\partial C}{\partial x_2}, \qquad J_3 = D_3 \frac{\partial C}{\partial x_3} \tag{2.28}$$

2.3.1.4 Solutions of the Diffusion Equation in Cartesian Coordinates:

For an analytical solution of the diffusion equation, geometrically symmetrical conditions should be satisfied. The solutions can be given either in the form of Fourier series or in the form that consists of Gaussians, error functions and related integrals.

Steady-State Diffusion:

At steady state condition, the concentration does not vary with time:

$$\frac{\partial C}{\partial t} = 0 \tag{2.29}$$

If it is assumed that geometrical symmetries ($\partial/\partial y = \partial/\partial z = 0$) exist, then the solution for linear flow in one direction yields to

$$D\frac{\partial^2 C}{\partial x^2} = 0 \ and \ C(x) = a + Ax \tag{2.30}$$

Non-Steady-State Diffusion:

At non-steady state, the concentration changes with time. For the linear flow in one-dimension, initial condition at t=0 gives:

$$C(x,0) = Q\delta(x) \tag{2.31}$$

where Q is number of diffusing particles per unit area, which is called dose and $\delta(x)$ is the Dirac delta function.

The solution of the diffusion equation varies with respect to the condition defined for diffusant at the surface of the substrate. For the first case, the concentration of diffusant at the surface is constant. As the diffusant spread into the substrate, the amount of diffusant at the surface does not change. For the second case, the total amounts of diffusant are fixed. Thus, a thin layer of dopant is deposited onto the substrate with a constant amount of diffusant, then all of them flow into the substrate.

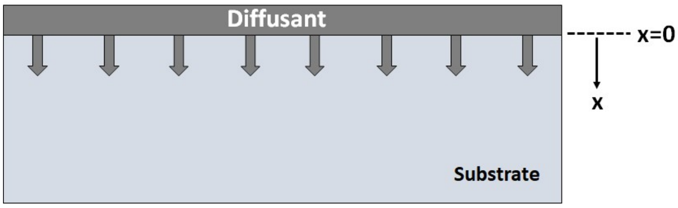

Figure 2.8 Thin film geometry with a fixed amount of diffusant (Q) at the surface of substrate

Case 1: Constant Surface Concentration:

The initial condition at $t = 0$; $C(x, 0) = 0$.

The boundary conditions; $C(0, t) = C_s$ and $C(\infty, t) = 0$,

The solution of diffusion equation is given by

$$C(x,t) = C_s erfc\left(\frac{x}{2\sqrt{Dt}}\right) \tag{2.32}$$

where C_s:surface concentration, t: diffusion time, erfc: complementary error function

Case 2: Constant Total Dopant:

The initial condition at $t = 0$; $C(x, 0) = 0$.

The boundary conditions; $\int_0^{+\infty} C(x,t)dx = Q$ and $C(\infty, t) = 0$,

The solution of the diffusion equation is given by

$$C(x,t) = \frac{Q}{\sqrt{\pi Dt}} \exp\left(-\frac{x^2}{4Dt}\right) \tag{2.33}$$

where Q is the total amount of dopant in unit area.

Diffusion process for thin film geometry obeys the conservation of the integral number of diffusing particles:

$$\int_{0}^{+\infty} \frac{\mathrm{Q}}{\sqrt{\Omega Dt}} exp\left(-\frac{x^2}{4Dt}\right) dx = \int_{0}^{+\infty} 2Q\delta(x)\mathrm{dx} = \mathrm{Q} \tag{2.34}$$

The solution given above are Gaussian equations. In the solutions, $2\sqrt{Dt}$ stands for diffusion length, which is a typical quantity for diffusion problems.

2.3.1.5 Sheet Resistance of Diffused Layer

Sheet resistance (R_S) of a diffused layer that forms a pn junction with a junction depth x_j and the impurity concentration $C(x)$ can be defined by the following equation:

$$R_S = \frac{1}{q\int_0^{x_j} \mu C(x)dx} = \frac{1}{q\mu_{eff}\int_0^{x_j} C(x)dx} \tag{2.35}$$

μ is the majority carrier mobility (cm^2/V.s) and it is concentration dependent parameter

μ_{eff} is effective mobility (cm^2/V.s), which is used when the carrier concentration is greater than 10^{16} atoms/cm^3.

The empirical expressions of μ versus C obtained;

for electron mobility in n-type silicon (μ_e):

$$\mu_e = \frac{1360 - 92}{1 + (\frac{C}{1.3 \times 10^{17}})^{0.91}} + 92 \tag{2.36}$$

for hole mobility in p-type silicon (μ_h):

$$\mu_h = \frac{468 - 49.7}{1 + (\frac{C}{1.6 \times 10^{17}})^{0.7}} + 49.7 \tag{2.37}$$

From R_S, the average resistivity, ρ, of the diffused layer can be obtained by the following expression:

$$\rho = R_S\, x_j \tag{2.38}$$

2.3.1.6 Diffusion Equation for Ion Implantation and Post Annealing

For a doping by ion implantation method with a constant energy, distribution of function (as-implanted doping profile) is given by

$$C(x,0) = \frac{Q}{\sqrt{2\pi \Delta R_p}} \exp\left(-\frac{(x-R_p)^2}{4Dt}\right) \tag{2.39}$$

where R_p is the mean projected range of implantation and ΔR_p the standard deviation of the projected range.

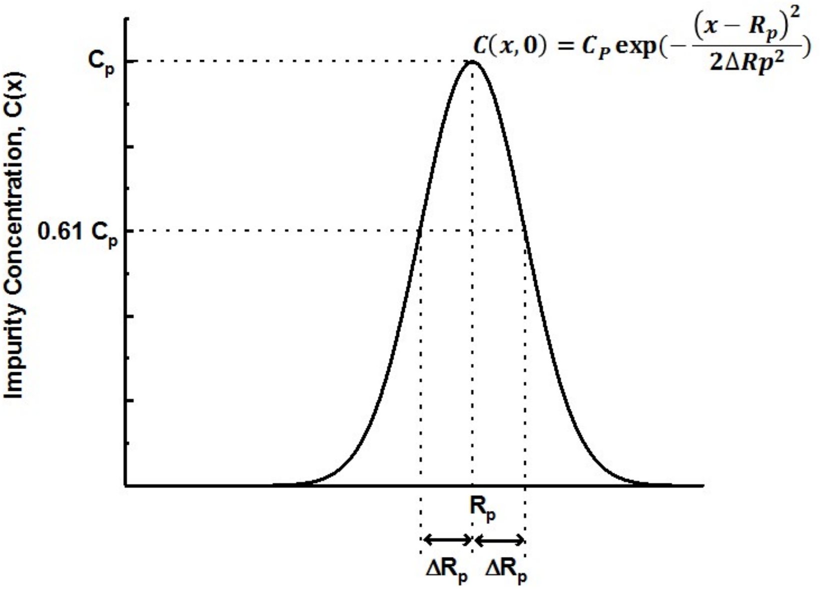

Figure 2.9 Dopant profile of ion implanted substrate (Adapted from [9])

When the implanted sample is annealed, the implant profile will broaden due to diffusion of dopants.

$$C(x,t) = \frac{Q}{\sqrt{2\pi\Delta R_p + 4Dt}} \exp\left(-\frac{(x - R_p)^2}{2\Delta R_p + 4Dt}\right) \tag{2.40}$$

Since the implantation profile after implantation is very close to the surface of the sample, the equation should be modified. The surface may act as a perfect mirror or a perfect sink for tracer atoms. The modified solution of Fick's second equation can be written as:

$$C(x,t) = \frac{Q}{\sqrt{2\pi\Delta R_p + 4Dt}} \exp\left([-\frac{\left(x - R_p\right)^2}{2\Delta R_p + 4Dt}] \pm \exp[-\frac{(x + R_p)^2}{2\Delta R_p + 4Dt}]\right) \tag{2.41}$$

The minus sign (-) in the modified equation is used for a perfect sink and plus sign (+) is for perfect reflection.

2.3.2 Atomic Diffusion Approach and Modelling

The solution of simple Fick's diffusion equation, which does not deal with the mechanism of atomic movements of impurities in the crystal, was already discussed in Section 2.3.1; however, it cannot estimate the doping profile accurately when the dopant concentration is above the intrinsic carrier concentration, n_i. For the high concentration level of impurities, atomic models of solid state are needed. Since diffusion is based on the generation, annihilation and movement of point defects and their interaction with impurities, the details of defect-impurity interaction should be understood deeply to model a diffusion process. The computer programs such as SUPREM-IV, which is applied for the simulation of implant and diffusion processes in this study, are solving continuity equations including point defect equations.

According to the atomic models, diffusion is governed by impurity-point defect interaction at different charge states. Point defects, vacancy (V) or interstitial (I), can be neutral, single charged and double charged but not more since the probability of a charge state higher than two is very low. When point defects accept or lose electrons and they become electrically active.

If a vacancy accepts an electron, it acts as an acceptor:

$$V + e \rightleftharpoons V^{-} \tag{2.42}$$

If an interstitial accepts an electron, it also acts as an acceptor:

$$I + e \rightleftharpoons I^{-} \tag{2.43}$$

The reaction of impurity atoms in a silicon crystal can take place in two different ways.

The first case: A substitutional impurity atom (I_S) can be kicked out of its substitutional site by an interstitial silicon atom (Si_I), and the impurity atom becomes interstitial atom (I_I).

$$I_S + Si_I \rightleftharpoons I_I \tag{2.44}$$

Alternatively, the first reaction could end up with the following consequences. The substitutional impurity atom could

- move to a vacancy site,
- kick out another interstitial silicon atom,
- diffuse interstitially for some distance.

The second case: A substitutional impurity atom can leave a vacancy behind and become an interstitial atom.

$$I_S \rightleftharpoons V + I_I \tag{2.45}$$

If the impurity in this reaction was a silicon atom as follows;

$$Si_S \rightleftharpoons V + Si_I \tag{2.46}$$

then the equation would stand for a Frenkel pair, that is the total numbers of vacancies and interstitials are equal.

The reaction equation for impurity and defect above are equilibrium reactions, which the law of mass action can be applied to determine equilibrium constants. According to the law of mass action, the equilibrium constants of a chemical reaction in gas phase can be written in terms of chemical activity of the reactants and products.

A simple reversible chemical reaction in gas phase is expressed as

$$\alpha A + \beta B \rightleftharpoons \gamma C \tag{2.47}$$

where α, β and γ are mole concentration of elements A, B, and C, respectively.

The equilibrium constant toward to right hand side is found as

$$K_c = \frac{a_A^{\alpha} a_B^{\beta}}{a_C^{\gamma}} \tag{2.48}$$

where a_A, a_β and a_γ are chemical activities of the elements A, B, and C, respctively and K_c is the equilibrium constant. According to Raoult's law, the chemical activities can be replaced by concentration of elements in the reaction if it is a dilute solution (near ideal solution). In this case, equilibrium constant, K_c, can be written as

$$K_c = \frac{[A]^{\alpha}[B]^{\beta}}{[C]^{\gamma}} \tag{2.49}$$

where $[A]$, $[B]$ and $[C]$ are the concentrations of elements A, B, and C, respectively.

If the mass of action is applied to the point defects in a crystal lattice where they are considered as dilute solid solution of defects in crystal lattice, vacancy and self-interstitial concentrations can be determined from statistical thermodynamics. The concentration of those defects can be expressed in terms of entropies of formation, ΔS, and formation energies, ΔH. For a neutral mono-vacancy in a silicon crystal, the concentration of vacancies C_V^x is determined by

$$C_V^x = 5.5 \times 10^{20} \exp\left(\frac{\Delta S_V^x}{k}\right) \exp\left(\frac{-\Delta H_V^x}{kT}\right) \tag{2.50}$$

where ΔS_V^x:entropy of formation of a neutral monovacancy, ΔH_V^x:formation energy of a neutral monovacancy, superscript x: neutral charge state.

For silicon, entropy of formation of a neutral monovacancy, ΔS_V^x, is 1.1 k and formation energy of a neutral monovacancy, ΔH_V^x, equals or greater than 2.5 eV. So, the intrinsic concentration of monovacancies, C_V^x, in silicon at 1000 ºC is estimated to equals 2.1×10^{11} cm^{-3}.

Based on Fermi statistics donor type mono-vacancy concentration can be expressed as

$$C_V^+ = \frac{1 + g_V \exp(\frac{E_{Fi} - E_V}{kT})}{1 + g_V \exp(\frac{E_F - E_V}{kT})} C_i(V^+) \tag{2.51}$$

where g_V is the spin degeneracy of the vacancy level and equal ½, $C_i(V^+)$: donor vacancy concentration in intrinsic silicon, E_{Fi}: Fermi level of intrinsic silicon, E_F: Fermi level of extrinsic silicon and E_V:acceptor vacancy energy level. [24]

In the same manner, the acceptor type vacancy concentration, C_V^-, for extrinsic silicon is found by

$$C_V^- = \frac{1 + \frac{1}{2} \exp(\frac{E_V - E_{Fi}}{kT})}{1 + \frac{1}{2} \exp(\frac{E_V - E_F}{kT})} C_i(V^-) \tag{2.52}$$

where $C_i(V^-)$: acceptor vacancy concentration in intrinsic silicon.

For $(E_V - E_F) \gg kT$ and $(E_V - E_{Fi}) \gg kT$, equation (2.52) yields to

$$C_V^- \cong \frac{\exp\left(\frac{E_V - E_{Fi}}{kT}\right)}{\exp\left(\frac{E_V - E_F}{kT}\right)} C_i(V^-) \tag{2.53}$$

Thus,

$$\frac{C_V^-}{C_i(V^-)} = \exp\left(\frac{E_F - E_{Fi}}{kT}\right) \tag{2.54}$$

In the case of nondegeneracy, extrinsic carrier concentration, n, for the n-type Si is expressed as

$$n = n_i exp\left(\frac{E_F - E_{Fi}}{kT}\right) \tag{2.55}$$

where n_i: intrinsic carrier concentration.

If equations (2.54) and (2.55) are combined, then it yields to

$$\frac{C_V^-}{C_i(V^-)} = \frac{n}{n_i} \tag{2.56}$$

If the impurity diffusion is dominated by acceptor monovacancy mechanism, then diffusivity (D) can be assumed to be equal to the acceptor monovacancy concentration, C_V^-. Thus,

$$\frac{D}{D_i} = \frac{n}{n_i} \tag{2.57}$$

where D: diffusivity in extrinsic Si, D_i: diffusivity in intrinsic Si. n_i can be found by the following empirical formula:

$$n_i^2 = 1.5 \times 10^{33} T^3 \exp\left[\frac{-1.21 + \Delta E_g}{kT}\right] \tag{2.58}$$

where $\Delta E_g = -7.1 \times 10^{-1} \; (\frac{n_i}{T})^{1/2}$ and assumed as 1.21 eV.

According to equation (2.57), the interaction of the impurity atoms with charged acceptor vacancies results in the dependence of diffusivities on the Fermi level at given diffusion temperature. Therefore, it is more convenient to generalize equation (2.57) to

$$D = D^x + D^-\left(\frac{n}{n_i}\right) + D^=\left(\frac{n}{n_i}\right)^2 + D^+\left(\frac{n_i}{n}\right) + \cdots \tag{2.59}$$

where D^x: intrinsic diffusivity of impurity interaction with a neutral point defect,

D^-: intrinsic diffusivity of impurity interaction with a single charged acceptor point defect,

$D^{=}$: intrinsic diffusivity of impurity interaction with a double charged acceptor point defect,

D^{+}: intrinsic diffusivity of impurity interaction with a single charged donor point defect.

Equation (2.59) expresses the concentration dependence of diffusivity, and it can be substituted into equation of Fick's second law of diffusion equation (2.25) to determine doping profile; however, it does not tell what exactly the dominating mechanism, either vacancy or interstitial. The dominating mechanism in the diffusion processes can be determined by experimental evidence or other theoretical assumptions.

The dependence of diffusion on both interstitial and vacancy, an effective diffusion coefficient, D_A is defined as

$$\frac{D_A}{D_A^*} = f_I \frac{C_I}{C_I^*} + (1 - f_I)\frac{C_V}{C_V^*} \tag{2.60}$$

where C_I and C_V are concentrations of interstitials and vacancies created by ion implantation, respectively. D_A^*, C_I^* and C_V^* are corresponding values at thermal equilibrium. f_I is the fractional interstitial component of diffusion under equilibrium [25].

2.3.2.1 Effect of Local Electric Field on Diffusion Flux

During the diffusion of impurities at high temperatures, a local electric field, which improves the diffusion flux, is created between ionized atoms and the electrons, or holes. In other words, apart from the chemical diffusion of dopants and defects in a medium, diffusion flux should include a drift term, which is resulted from local built-in electric field. Diffusion flux defined in equation (2.61) explains chemical diffusion (or diffusion under nonequilibrium conditions), which is related to spatial concentration gradients in the material, but it is insufficient for the total diffusion flux of electrically active ions within a crystal. Dopants in semiconductors carry free carriers which have greater mobility than the parent atoms. Thus, free carriers will diffuse ahead of the dopants, which will eventually create a local electric field and affect the flux of ionized dopants. This necessitates that a drift term, which is proportional to the local electric field, is needed in the flux formula:

$$J = -D\nabla \mathrm{C} + \mathrm{C}\mu \mathrm{E} \tag{2.61}$$

where C: mobile impurity concentration, μ: mobility of impurities, E: the electric field.

If we recall to Einstein's relation:

$$D = \frac{kT}{q}\mu$$

μ can be written in terms of D. If it is inserted in equation (2.18), then total flux will yield to

$$J = -D(\nabla \mathrm{C} - Z\mathrm{C}\frac{qE}{kT}) \tag{2.62}$$

where Z is particle charge which is +1 for donor and -1 for acceptor. E-field is zero for insulators and metals; but for semiconductors, it is given as

$$E = -\nabla\psi = -\frac{kT}{qn}\nabla \mathrm{n} \tag{2.63}$$

where ψ is electrostatic potential and n is electron concentration. In terms of charge neutrality, electron concentration is written as

$$n = \frac{N_D - N_A}{2} + \sqrt{\left(\frac{N_D - N_A}{2}\right)^2 + {n_i}^2} \tag{2.64}$$

where n_i is intrinsic carrier concentration. N_D and N_A are the concentration of electrically active donor and acceptor, respectively.

If drift term is included in the diffusion flux, then Eq 2.6 yields to the following on which many pair diffusion models in the literature are based on:

$$\frac{\partial C}{\partial t} = \nabla.\mathrm{D}\left(\nabla \mathrm{C} - Z\mathrm{C}\frac{qE}{kT}\right) \tag{2.65}$$

According to Eq.2.7, defect populations are in thermodynamical equilibrium and the effects of point defects on diffusion are built into the pair diffusivities (dopant-vacancy or dopant-interstitial pairs). In another word, it assumes that dopant-defect pairs diffuse together. According to models based on the concept of Pair Diffusion, dopants cannot diffuse freely by themselves whereas, point defects can do [26].

Pair Diffusion models are quite helpful for fast computation but sometimes they are very accurate due to some variable conditions, such as activation, impurity clustering and interfaces. [27]

Firstly, impurity segregation and change in transport velocity across material interfaces in multilayer structures will result in the inaccuracy of modeling of dopant diffusion. Regarding the interface of two materials such as silicon and oxide, dose loss at the interface of two is another issue in modeling.

Secondly, if the dose of dopant is very high, then some of the dopants may be electrically inactive due to solid solubility limit. In this case, electrically active concentration will be less than chemical concentration, and the excess dopants will not contribute to free carrier concentration. In addition, the inactive dopants must be assumed not to diffuse.

Thirdly, impurity clustering, which is available in the ion implantation process, are very effective in diffusion flux. Free interstitials are thermodynamically unstable in crystalline materials since they have very high free energy due to unpaired electron orbitals and induced lattice strain. When the interstitial concentration is very high, it is very likely to observe the various type of clusters such as small clusters, {311} defects, perfect and faulted loops.

2.4 Basics of Crystalline Silicon Homojunction Solar Cells

The operation of a solar cell is based on the photovoltaic effect, which is the formation of electrical current and voltage in material under illumination. When photon energy is higher than the bandgap energy of the illuminated semiconductor material, it is absorbed and creates an electron and hole pair. The generated electron and hole pair is separated by an electric field, E, which is called "drift transport". In the case of homojunction solar cells, the internal field is created by a p-n junction by adjacent p-doped and n-doped regions in the semiconductor material as illustrated in *Figure 2.10*.

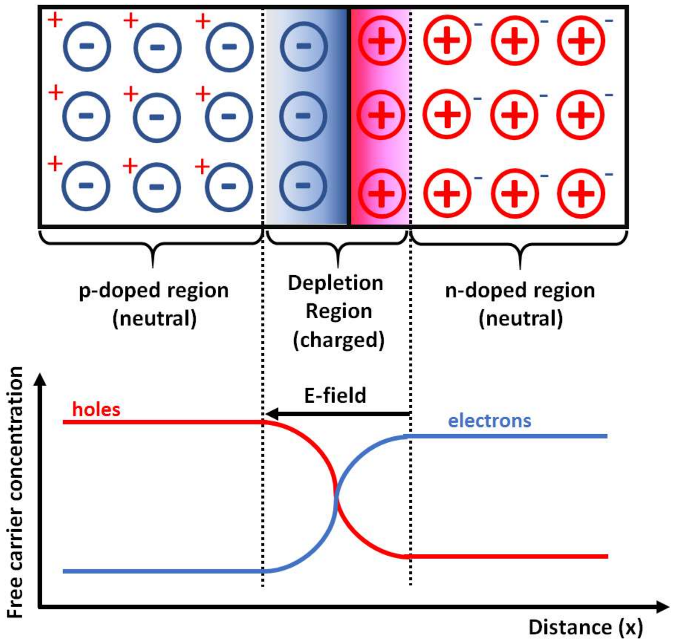

Figure 2.10 Charge distribution in a p-n junction under the dark condition (Redrawn from [28])

Due to the excess electron in the n-side and excess holes in the p-side of the material, electrons and holes will diffuse in the opposite directions leaving positively charged ions in the n-region and negatively charged ions p region, respectively. Since the electrons and holes are charged, they do not diffuse until their concentrations are equal on each side of the material due to columbic interaction with fixed ions that they leave behind. This movement results in the formation of the depletion region lacking the electron and hole since the electric field formed in the junction repels them out. The electric field results in a built-in potential, V_{bi}, in at the junction.

2.4.1 Equivalent Circuits of a Solar Cell

Solar cells are semiconductor diodes operating under the light. For the dark condition, the current-voltage characteristic of a semiconductor diode is given by

$$J_{dark} = J_0 \left[\exp\left(\frac{qV}{knT}\right) - 1\right] \tag{2.66}$$

where

q=1.6022×10^{-19} [C] is the elementary charge,

k= 1.3807×10^{-23} [m^2 kg/(s^2K)] is the Boltzmann constant,

n is the so-called "diode ideality factor",

T [K] is the absolute temperature,

J_0 is the reverse saturation current density, which depends on the recombination rate in within the diode.

Under the illumination, photo-generated current, J_{ph}, is included in the diode equation, which leads equation (2.66) to

$$J = J_{ph} - J_{dark} = J_{ph} - J_0 \left[\exp\left(\frac{qV}{knT}\right) - 1\right] \tag{2.67}$$

where J is the current density of solar cell under light. The minus sign in front of J_0 is due to the opposite direction of diode forward current and photo-generated current. The J-V curves for both dark current and photo-generated current are illustrated in

Figure 2.11. A solar cell operates at maximum power point, at which both current and voltage is generated by photovoltaic effect. When a forward bias is applied to the solar cell, built in potential within the junction is reduced, leading to the balance of light generated current and diffusion current. The forward bias at which the net current is zero, is called the open circuit condition.

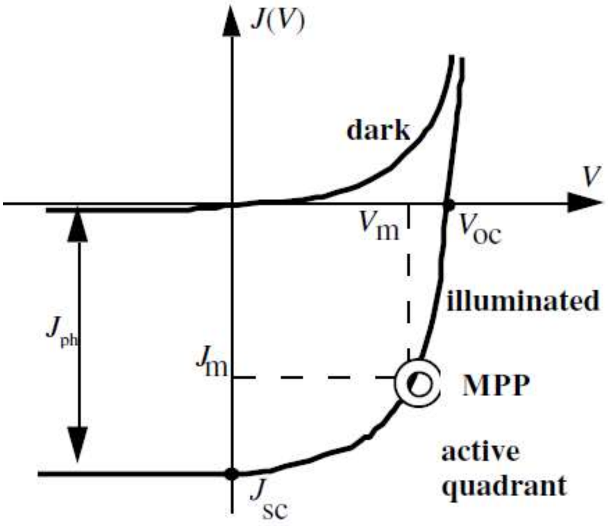

Figure 2.11 I-V characteristics of a solar cell under dark and illuminated condition [28].

Figure 2.12 illustrates an equivalent circuit diagram of the double diode model for a solar cell including illumination current density (J_{ph}), shunt resistance (R_{Shunt}), series resistance (R_S), and recombination current densities (J_o) in the bulk, surface and the junction. At high voltages meaning that the recombination is dominated by the surface and the bulk recombination, the ideality factor approaches one; however, it gets closer to two at lower voltages implying that the recombination mainly occurs in the junction.

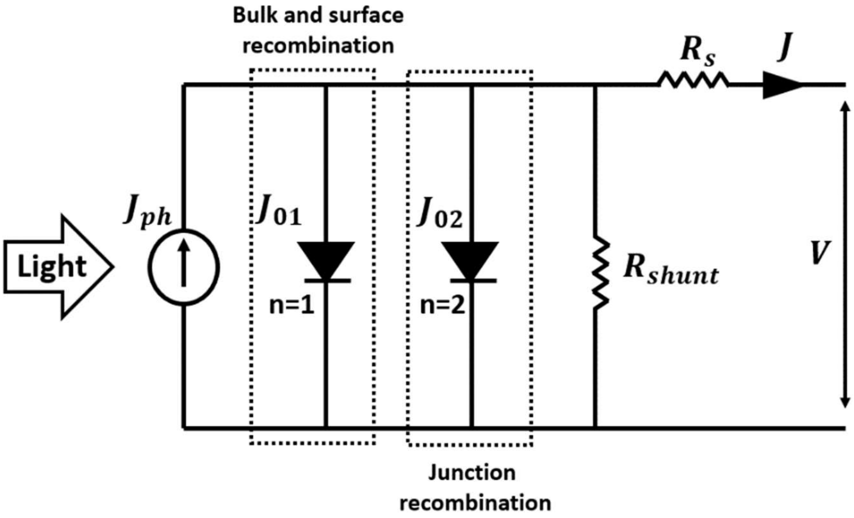

Figure 2.12 An equivalent circuit diagram of the double diode model for a solar cell (Redrawn from [29][30])

The equation for the double diode model under illumination can be written as

$$J = J_{ph} - J_{01}\left\{\exp\left[\frac{q(V + JR_S)}{kT}\right] - 1\right\} - J_{02}\left\{\exp\left[\frac{q(V + JR_S)}{2kT}\right] - 1\right\} - \frac{V + JR_S}{R_{shunt}} \qquad (2.68)$$

Since the second diode is affected by small fluctuations of the light, the analysis of the diode characteristics is typically conducted under dark conditions. Also, the -1 terms in the equation are typically omitted for easier analysis. In this case, J is simply written as

$$J = J_{01}\exp\left[\frac{q(V - JR_S)}{kT}\right] + J_{02}\exp\left[\frac{q(V - JR_S)}{2kT}\right] + \frac{V - JR_S}{R_{shunt}} \qquad (2.69)$$

2.4.2 Solar Cell Parameters

The performance of a solar cell can be analyzed by characterization of short circuit current density (J_{sc}), open circuit voltage (V_{oc}), fill factor (FF) and photoconversion efficiency (η).

Photoconversion Efficiency:

η is the ratio between the input power of illumination (P_{in}) and the electrical output power of the device (P_{out}).

$$\eta = \frac{P_{out}}{P_{in}} \tag{2.70}$$

where $P_{out} = V_{oc} \times J_{SC} \times Area\ of\ the\ solar\ cell$ [28].

The conversion efficiency of a solar cell is measured under standard conditions where the light incident is AM1.5 spectrum, thus having irradiance of 1000 W/m^2 [11].

Short Circuit Current Density:

The current is maximum current through the solar cell is the short circuit current density, J_{sc}, which is attained when the voltage across the solar cell is zero. J_{sc} of a solar cell is determined by the intensity and the spectrum of the incident light, optical properties of the Si (reflection and absorption) and the minority carrier collection probability. J_{sc} is equal to J_{ph} in an ideal solar cell, which has recombination and parasitic resistive losses. J_{ph} is given by the following equation [11]

$$J_{ph} = qG(L_n + L_p + W) \tag{2.71}$$

G: carrier generation rate

L_n: electron diffusion length

L_p: hole diffusion length

Open Circuit Voltage:

The voltage at which the current across the solar cell is zero is the open circuit voltage (V_{OC}). In other words, V_{OC} is the forward bias voltage at which the dark current density compensates the photocurrent density, and it is the maximum voltage that a solar cell can reach.

When J in equation (2.67) is zero, then V_{OC} can be expressed as

$$V_{OC} = \frac{nkT}{q} ln\left[\frac{J_{ph}}{J_0} + 1\right] \approx \frac{nkT}{q} ln\left[\frac{J_{ph}}{J_0}\right] \tag{2.72}$$

Eq (2.72) shows the dependency of V_{OC} on J_{ph} and J_0 at which J_0 is determined by the recombination in the solar cell. It should be also noted that V_{oc} does not increase linearly with temperature since J_0 also increases due to increasing intrinsic carrier concentration (n_i).

V_{OC} can also be determined as follows which is the so-called implied V_{OC}

$$V_{OC} = \frac{nkT}{q} ln\left[\frac{(N_A + \Delta n)\Delta n}{n_i^2}\right] \tag{2.73}$$

where N_A: doping concentration and Δn: excess carrier concentration, n_i: intrinsic carrier concentration.

It is clearly seen in the Eq (2.73) that V_{OC} of a solar cell increases with the increasing Δn.

The theoretical limit of V_{OC} is below the voltage (V_g) corresponding to the bandgap (E_g) which is the energy difference between above the valence band edge, E_v, and below the conduction band edge, E_c, E_c, E_v and E_g of a semiconductor are illustrated in *Figure 2.2*.

Fill Factor:

Fill factor is the ratio of the maximum power to the product of V_{OC} and J_{SC} of a solar cell.

$$FF = \frac{V_{mpp} \times J_{mpp}}{V_{oc} \times J_{SC}} \tag{2.74}$$

V_{mpp} and J_{mpp} are the voltage and current density values of a solar cell operating at maximum power output. For a solar cell with an ideal diode, FF can be written in terms of V_{oc} as

$$FF = \frac{v_{oc} - \ln(v_{oc} + 0.72)}{v_{oc} + 1} \tag{2.75}$$

where v_{oc} is the normalized voltage and expressed as

$$v_{oc} = V_{oc}\frac{q}{k_B T} \tag{2.76}$$

FF is affected by parasitic resistances, which are R_S and R_{Shunt}. The R_s should be minimized while the R_{shunt} should be maximized as much as possible for higher FF, thus improving solar cell efficiency. R_S can be caused by the emitter, back surface field (BSF), the base of the wafer, the metal, and contacts between the metal and the silicon (Si). On the other hand, low R_{shunt} is caused by alternative current paths to the junction for photocurrent in the device. The effect of shunting is more intense in the case of low light intensities due to less photo-generated current while the effect of R_s is more dominant at lower voltages thus a larger current [11].

CHAPTER 3

FABRICATION AND CHARACTERIZATION METHODS

In this chapter, fabrication and characterization methods for the fabrication of the solar cells studied in this thesis are explained.

3.1 Ion Implantation

In this thesis, the ion implantation processes were performed in ODTÜ-GÜNAM Photovoltaic Line (GPVL) located in Ankara, Turkey by Bosphorus ion implanter system, which is shown in *Figure 3.1*.

Figure 3.1 Images of Bosphorus ion implantation system from outside (left) and inside (right)

The equipment is capable of implanting P for n^{++}; B and BF_2 for p^{++} formation. The implanted ions are subsequently activated under N_2 and O_2 ambient in an atmospheric furnace.

Owing to the single side doping capability of the ion implantation method, some additional process steps such as single side etching or deposition/removal of the protection layer required for the diffusion method can be eliminated in the fabrication of PERC and PERT solar cells. Additionally, for the formation of highly doped patterned p^{++} and n^{++} region at the rear surface and lowly doped p^{+} or n^{+} at the front surface, additional processes are required in the case of doping by high temperature diffusion furnaces. However, all these additional processes can be eliminated since the implantation method allows doping through a hard mask with a variety of material selections. In this context, we designed various hard masks to form doping patterns for small and large area IBC solar cells fabrication as shown in *Figure 3.2*.

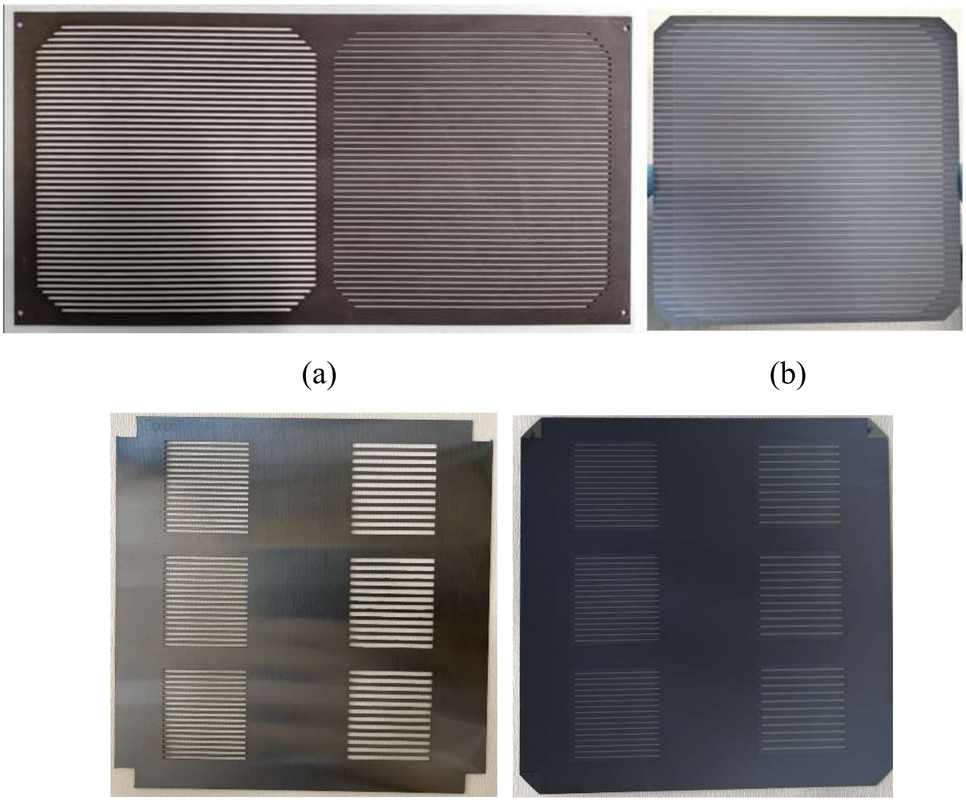
(a) (b)

(c) (d)

Figure 3.2 (a) graphite mask for large area IBC solar cell, (c) mc-Si mask for multiple small area IBC solar cells, (b) and (d) the subsequent implanted Si wafers

For the characterization of implantation and subsequent activation processes, the four-point probe and the electrochemical capacitance-voltage methods were applied for sheet resistance (R_{sheet}) and active doping profile measurements, respectively.

Also, the doping profiles of species including active and inactive ones were measured by time-of-flight secondary ion mass spectrometry (ToF-SIMS).

3.2 Deposition of Passivation Layers

For the passivation and antireflection layer or stack layer of the implanted and unimplanted wafers, alumina (Al_2O_3), silicon nitride (SiN_x), silicon oxynitride (SiO_xN_y) or a stack of these materials were deposited. While the Al_2O_3 layer was deposited by a spatial atomic layer deposition (ALD) tool, SiN_x and SiO_xN_y layers were deposited by an industrial plasma enhanced chemical vapor deposition (PECVD) system [31]. Additionally, silicon dioxide (SiO_2), which was thermally grown by an atmospheric furnace under a mixture of O_2 and N_2 gas flow, was also applied for passivation. The passivation quality of the dielectric layers on symmetrically prepared samples was measured with the photo-conductance method by the Sinton WCT-120 instrument [32]. The analysis of passivation samples was made on the implied open circuit voltage (iV_{oc}) and effective lifetime (τ_{eff}) and bulk lifetime (τ_{bulk}) values measured on the samples.

3.3 Laser Contact Openings and Metallization Processes

A picosecond laser operating at 532 nm (green) wavelength and 400 kHz pulse repetition rate (f_{rep}) was used for the ablation of dielectric layers at the rear surface of PERC and IBC solar cells. *Figure 3.3* illustrates the laser system (left) and small size ion implanted p-IBC solar cells on a M2 wafer with LCO prepared for Al/Si alloy formation by Al printing and subsequent fast firing process.

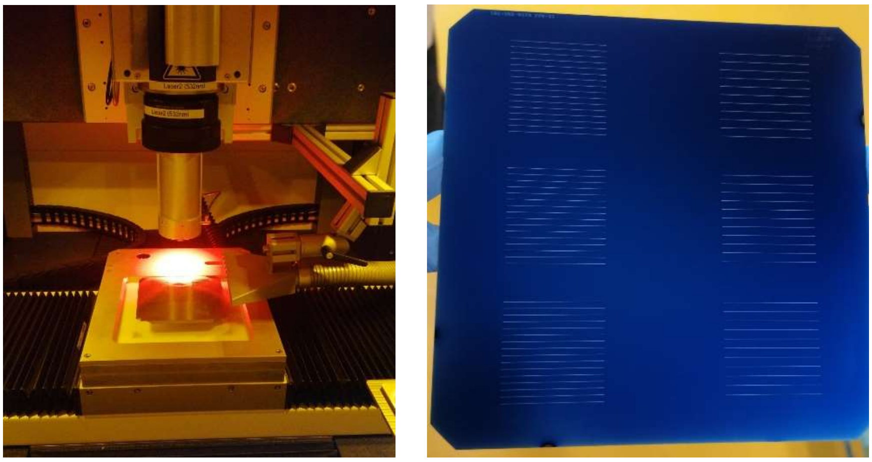

Figure 3.3 Images of the picosecond laser (left) and pattern of laser ablation on p-IBC solar cells (right) taken in ODTÜ-GÜNAM Photovoltaic Line

The metallization of the solar cells was conducted by the screen printing method. Silver and Silver/Aluminum (Ag/Al) fire through metal pastes were printed on the n^{++} side and p^{++}, respectively. Similarly, Al metal paste was used for BSF formation on the p-Si wafer in the PERC and p-IBC cell fabrication. Following the printing process, the screen printed Ag and Ag/Al were exposed to a fast firing process by a conveyor belt furnace for fire through dielectric layers and Al-Si alloy formation within the laser contact openings (LCO).

After the metallization process, I-V and SunsVoc measurements were performed on the solar cells by the Class AAA solar simulator and Sinton WCT-120 tool, respectively. Also, external quantum efficiency (EQE) measurements were conducted on the fabricated devices to analyze the photo-response at the front and rear surfaces. Additionally, the contact quality of the fire through metals with implanted regions was tested on the stripes cut from the fabricated solar cells by the transmission line method (TLM) [33][34].

CHAPTER 4

PASSIVATED EMITTER AND REAR CELL

Passivated emitter and rear cell (PERC) concept was first demonstrated as a laboratory-scale solar cell in 1989. This technology has been transferred to the industry 25 years after its first introduction. Today, it constitutes the majority of photovoltaic production lines. Before the development of PERC solar cells, the rear side of the silicon solar cells having a 90% market share was fully screen printed with aluminum (Al), the so-called aluminum back surface field (Al-BSF). Although the Al-BSF partially suppresses the recombination losses, a full area of Al causes excessive photo-generated carrier recombination at the back surface. On the other hand, local contact designs significantly reduce these losses. Moreover, it is advantageous in terms of light management since the dielectric layer can reflect the infrared light at the rear surface, which is typically absorbed by Al. The rear surfaces of the first lab-scale PERC solar cells were passivated with a silicon dioxide (SiO_2) layer, which was patterned with photolithography, and evaporated Al for local rear contact [35]. The limitation by optical and recombination losses have been suppressed with the proposed rear passivation concept. However, one of the bottlenecks for lab-scale PERC to be transferred to photovoltaic lines was the necessity of very clean conditions to grow thick thermal oxide which is not very applicable in industrial environments. Also, the oxide film did not withstand the firing process required following the metallization step. Therefore, thermal SiO_2 at the rear surface was replaced by PECVD: SiN_x soon after the introduction of the first lab-scale PERC concept. However, the positive fixed charges within SiN_x result in an induced floating junction underneath the dielectric layer, leading to a reduction in J_{sc}, V_{oc} and FF of the cell. The decrease in J_{sc} and FF was attributed to “parasitic shunting” of the floating junctions with metal contacts. This is because the electrons in the inversion layer created by the positive fixed charges at the rear surface are injected into rear contact, which in turn does not contribute to the cell current. The lower V_{oc} is due to enhanced carrier recombination within the inversion layer created by the positive fixed charges in the dielectric layer [36]. AlO_x with the negative fixed charges was found to be a suitable dielectric passivation layer to be used beneath the SiN_x at the rear side AlO_x, which was first deposited with the ALD method, was also studied with PECVD over time and started to be used in the industry. SiN_x capping layer on top of AlO_x provides not only a resistance to Al pastes during the firing process but also a back reflection of infrared light, thus improving photo-generated current. Another bottleneck for the industrialization of PERC cells was the rear side contact openings made by photolithography, which is not a feasible method for PV production lines. With the demonstration of laser ablation of the rear passivation layer, the PERC concept has been realized to be an industrial cell design [35]. A typical PERC solar cell is shown in *Figure 4.1*.

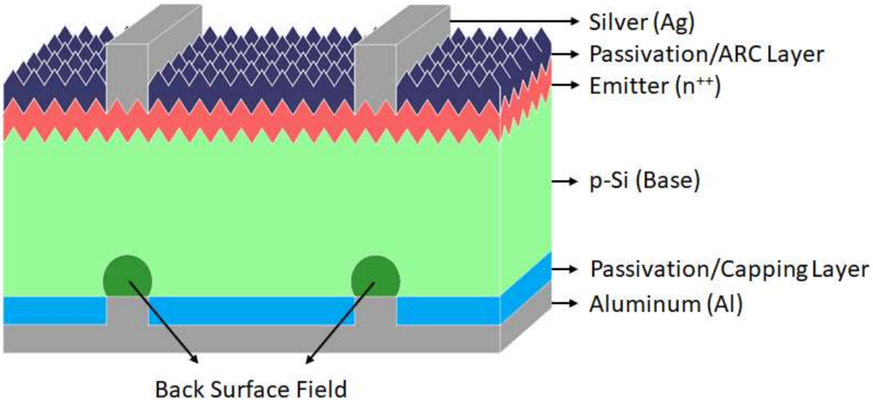

Figure 4.1 Schematic of a typical PERC solar cell

In the conventional fabrication flow of PERC solar cells, the emitter is formed by diffusion process, which ends up with double side doping and requires a subsequent single side etching (SSE) process for removal of the n^{++} region at their rear side. On the other hand, the ion implantation method for the formation of n^{++} region can eliminate the SSE process due to its capability for single side doping. In the following sections of this chapter, the ion implanted PERC solar cells are discussed.

In section 4.1, the doping profiles of the implanted P emitter are investigated as a function of implant dose and subsequent activation temperature.

In section 4.2, the ECV and ToF-SIMS profiles of P implanted Si wafers that were exposed to the annealing process are presented to determine the activated dopant concentration and the total amount of P in the wafers.

In section 4.3, we demonstrate the simplified process flow that we apply for ion implanted PERC cells with Al_2O_3/SiN_x stack passivation at the textured rear surface by eliminating the process steps such as rear surface polishing and deposition/removal of diffusion barrier layers.

In section 4.4, we show the optimization of the front and rear dielectric layers for the improvement of the ion-implanted PERC solar cell.

4.1 Optimization of Phosphorus Implant Dose and Activation Temperature for Emitter Formation of p-type Silicon Solar Cells

The ion implantation method has the capability of precise control of the doping profile, which is determined by the ion implantation parameters and subsequent annealing conditions [37][38]. Optimizing phosphorus (P) implantation dose and subsequent activation processes is crucial for a high quality emitter formation, thus a solar cell efficiency. Here, we investigate the effect of P implant dose and activation temperature on the iV_{oc} of the emitter of p-type textured Si solar wafers, which are passivated with 5 nm of thermal SiO_2 capped with PECVD:SiN_x. Our results suggest that the iV_{oc} of the relatively low dose P implanted p-Si wafers, which were passivated with SiO_2/SiN_x stack and exposed to a fast firing process, are strongly influenced by the activation temperature. We demonstrate iV_{oc} of 648 mV for implanted emitter with optimum implant dose and activation temperature.

4.1.1 Experimental Details

The industrial p-type Cz-Si solar wafers with bulk resistivity of 1-3 Ω.cm and thickness of 180±20 μm underwent potassium hydroxide (KOH) texturing to form random pyramids and ozone cleaning process to remove organic and metallic contamination. Then, the wafers were double side P implanted with two different doses (D0<D1) by the so-called Bosphorus implanter system manufactured by Dong Guan Plasma Ltd. The implanted samples were HF dipped and activated at various annealing temperatures of 850 °C, 875 °C, and 900 °C for 30 minutes under nitrogen flow. In order to ensure the same surface passivation quality, the samples were dipped into HF to remove unintentionally grown thermal oxide during activation, and approximately 5 nm of thermal oxide layers were grown by dry oxidation in an annealing furnace. After that, all the samples were coated with PECVD:SiN_x layers and fired by a conveyor belt furnace to mimic solar cell fabrication steps. Finally, the samples were annealed under forming gas for further improvement of iV_{oc} of the samples. The sheet resistances (R_{sheet}) and active dopant profiles of the samples were measured by the four-point probe (4PP) and electrochemical capacitance-voltage (ECV) methods, respectively. For the determination of the implied open circuit voltage (iV_{oc}) values, the symmetrical emitter samples were measured by the quasi-steady state photoconductance (QSSPC) method using a Sinton WCT-120 instrument. The schematic of our process flow and characterization steps are given in *Figure 4.2*.

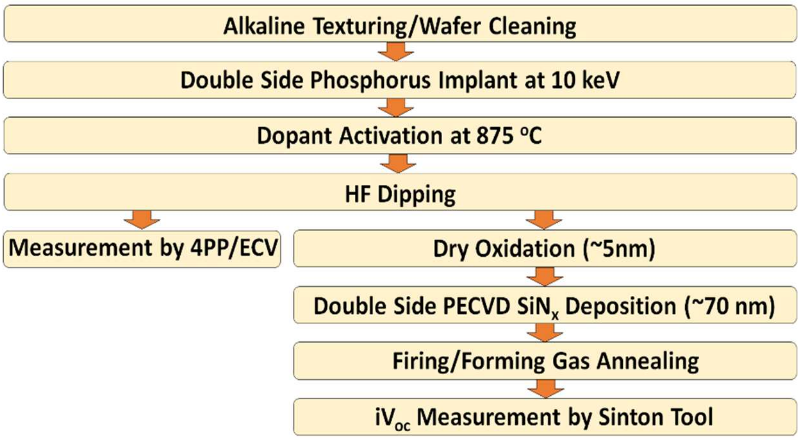

Figure 4.2 Process flow for sample preparation

The schematic of our symmetrical samples prepared for iV$_{oc}$ measurement is shown in *Figure 4.3*.

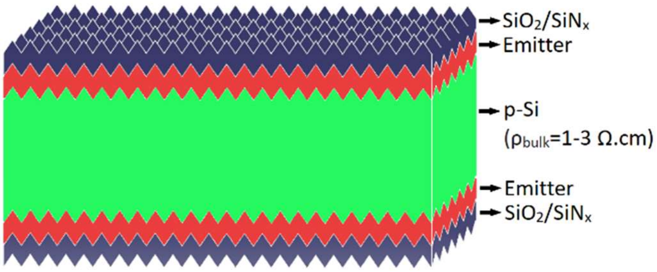

Figure 4.3 The schematic of the symmetrical emitter samples.

4.1.1 Results and Discussion

R$_{sheet}$ values of the samples with various implantation doses and activation temperatures are depicted in Table 5.1. R$_{sheet}$ decrease as the implantation dose and activation temperature increase.

Table 4.1 R_{sheet} *values of the samples measured by 4PP*

Sample Name	*Dose Name*	*Activation Temperature (°C)*	R_{sheet} *(Ω/sq.)*
D0-850	D0	850	120.4±9.5
D0-875		875	105.6±6.3
D0-875		900	93.6±3.6
D1-850	D1	850	90.7±3.9
D1-875		875	77.4±3.0
D1-900		900	73.7±4.6

Figure 4.4 illustrates the active P doping profiles of the samples measured by the ECV method. A higher activation temperature results in a decrease in peak concentration and an increase in junction depth. The trend is similar for both of the emitters but the peak concentrations are higher for the larger dose, D1.

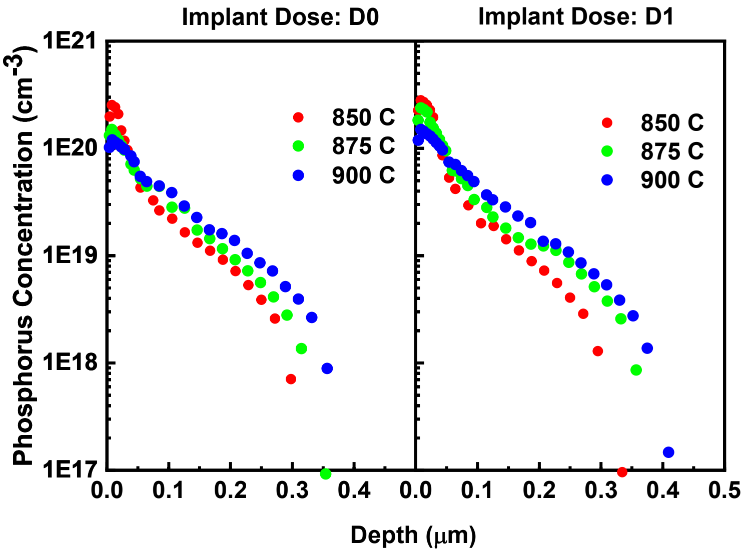

Figure 4.4 ECV profiles of P implanted emitters with doses of D0 (left) and D1 (right), and activation temperatures of 850 °C (red), 875 °C (green), and 900 °C (blue) for 30 minutes.

Figure 4.5 shows the iV_{oc} variation of the symmetrical samples with activation temperature. iV_{oc} of the emitters with a relatively lower dose named D0 significantly decreases with increasing activation temperature. On the other hand, it is slightly dependent on activation temperature for a higher dose, D1. The optimum value was obtained for the emitter with a dose of D1 and an activation temperature of 875 °C.

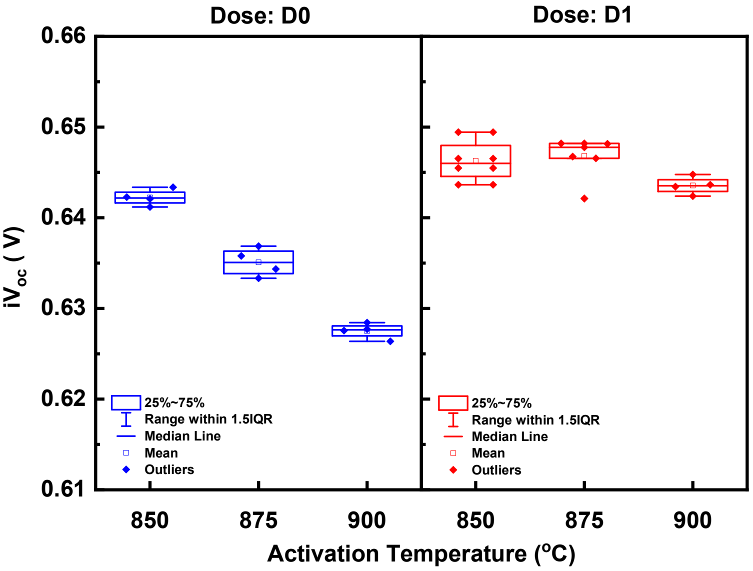

Figure 4.5 iV_{oc} values for the symmetrical emitter samples with implant dose of D0 (blue) and D1 (red) activated at 850 °C, 875 °C, and 900 °C.

In conclusion, we achieved a good control of the doping profile of the implanted emitter by changing the implant dose and subsequent activation temperature. Our results indicated that the iV_{oc} of the emitter implanted with a relatively lower dose, D0, is very sensitive to the activation temperature. The highest average iV_{oc} was 648 mV for the emitter implanted with dose D1 and activation temperature of 875 °C.

4.2 Determination of Phosphorus Doping Profiles by the ECV and ToF-SIMS Methods

Here, we compare the inactive and active P doping profiles on samples that are formed by implant dose of D2 and subsequent annealing at 875 °C on the flat surfaces. The doping parameters were intentionally selected considering the iV_{oc} values obtained in the previous section. For the determination of the total and active doping profile after the annealing process, we applied time-of-flight secondary ion mass spectrometry (ToF-SIMS) and electrochemical capacitance-voltage (ECV) methods, respectively.

For this study, we used nearly polished (saw damage etched) p-Si wafers. The samples were implanted with a certain dose and activated at 875 °C for 30 minutes under N_2 flow in an atmospheric annealing furnace. For the textured samples, the same doping dose was obtained by increasing the ion exposure time proportional to the surface roughness of the wafer. After the activation process, the samples were dipped into an HF solution and deposited with a PECVD: SiN_x layer. Then, the samples were exposed to a fast firing process to mimic the solar cell fabrication steps. Finally, the SiN_x layers were etched away by the HF dipping process. From the ECV and ToF-SIMS graphs in *Figure 4.6*, it is clearly seen that there are inactive dopants at the surface of the wafer. The dose of the dopants is calculated by integrating the profiles from surface to junction, which is 2.25E15 cm^{-2} and 1.14E15 cm^{-2} for the ToF-SIMS and ECV curves, respectively.

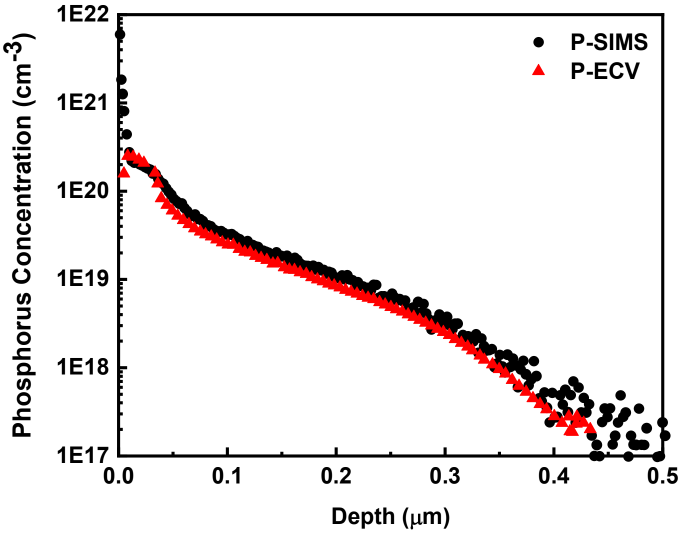

Figure 4.6 The active (red) and total (black) P doping profiles measured by ECV and ToF-SIMS, respectively.

4.3 Simplified Process Flow for the Fabrication of PERC Solar Cells with Ion Implanted Emitter

Applicability of phosphorus implantation for emitter formation specific to PERC solar cells has been already discussed in the literature by different groups [5][39][40]. However, it has not been benefited from the single side doping advantage of this method since additional steps have been included due to the concerns about the surface passivation at the front and rear surfaces. This is because the oxide growing during the activation process is desirable for the passivation of the emitter. On the other hand, it is well-known that the passivation quality of the SiO_2/SiN_x stack layer at the rear surface heavily depends on the surface morphology, unlike Al_2O_3/SiN_x [41][42]. Therefore, in the fabrication of implanted PERC cells passivated with Al_2O_3/SiN_x stack layer, either an oxide formation at the rear surface has been prevented during dopant activation or the rear surface has been polished before dopant activation to create suitable surface morphology for SiO_2 [39][43]. In any case, an additional step has been involved in the process flow, and the single side doping advantage of the ion implantation method has not been utilized. In addition to process simplification, it has been reported that the rear surface morphology influences the performance of bifacial p-Si PERC cells, and the cells with rougher surfaces can be preferable for high albedo values [42][44]. The applicability of a simple process flow for a PERC cell with a textured back surface would pave the way for the method to be applied to bifacial PERC cells to increase light trapping from the back surface. Hence, avoiding the rear surface processing step for the fabrication of PERC cells can fill a critical void in this research area.

In this study, we show a relatively high efficiency as in the literature for the implanted PERC cells fabricated without any additional process steps for the rear surface polishing or protection. For the simplification of the process flow, oxidation during dopant activation step was removed and Al_2O_3/SiN_x stack layer was optimized on the textured rear surface. In the scope of our study, the phosphorus (P) implant dose, the thickness of the Al_2O_3 layer, and the peak temperature for the fast firing process were optimized on the symmetrical samples. The results may facilitate a comparable efficiency of ion implanted PERC solar cells with considerably diminished workload and its corresponding cost compared to the ones in the literature.

4.3.1 Experimental Details

Process flow for the fabricated solar cells and characterization samples are depicted in *Figure 4.7*. Industrial 156.75x156.75 mm^2, p-type, Cz-Si wafers having bulk resistivity of 1-3 Ω.cm and thickness of 180±20 μm underwent potassium hydroxide (KOH) texturing to form random pyramids and subsequently ozone (O_3) cleaning process to remove organic and metallic contamination. Then, the samples were P implanted with two different doses named D1 and D2 by the so-called Bosphorus ion-implantation system manufactured by Dong Guan Plasma Ltd. For the dopant activation, the implanted samples were annealed at 875 °C under nitrogen (N_2) gas flow and dipped into hydrofluoric acid (HF) to remove the thin SiO_2 layer grown during activation. The rear side of the cells was coated with Al_2O_3 in different thicknesses of 5 and 20 nm by a spatial atomic layer deposition (ALD) tool. Then, 120 nm and 75 nm SiN_x:H were deposited by the plasma-enhanced chemical vapor deposition (PECVD) system at the rear and front surfaces, respectively. Afterward, the rear passivation layer was locally ablated by a picosecond laser operating at 532 nm (green) wavelength and 400 kHz pulse repetition rate (f_{rep})[45]. Laser contact openings (LCO) have been created in the form of dashed lines resulting in the removal of 3% of the rear stack passivation layer by the laser system. For the metallization of the cells, the screen printing method was applied. Silver (Ag) and aluminum (Al) metal pastes were printed at the front side and rear side, respectively. Finally, they were co-fired for fire-through of Ag through SiN_x layer at the front side, and local Al:BSF formation at the rear side. The process flow for the sample preparation is shown in *Figure 4.7*.

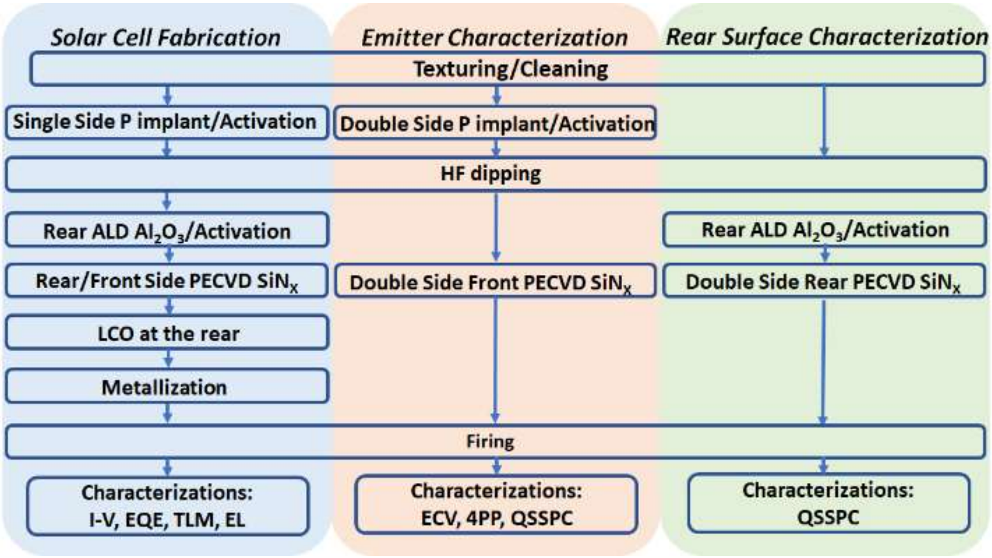

Figure 4.7 Process flow for the cells (left), symmetrical emitter (middle), and symmetrical rear surface (right) characterization samples.

The fabricated cells were characterized by current-voltage (I-V) measurements with a class AAA solar simulator under standard test conditions. The effect of Al_2O_3 thickness at the rear surface and implant dose at the front surface were analyzed by external quantum efficiency (EQE) measurement. For the determination of the contact resistivity of the front metal fingers, the transmission line method (TLM) was applied. The sheet resistances of the emitters were measured by the four-point probe (4PP) and the active dopant profile was obtained by the electrochemical capacitance-voltage (ECV) profiling methods. Implied open circuit voltage (iV_{oc}) values of the symmetrical SiN_x coated emitter and Al_2O_3/SiN_x stack layer coated textured rear surface were measured by quasi-steady state photoconductance (QSSPC) method using a Sinton WCT-120 instrument.

4.3.2 Results and Discussion

Front Side

The sheet resistances of the emitters, which were implanted with doses named D1 and D2, were measured to be 82 Ω/□ and 57 Ω/□ on average, respectively. The corresponding active dopant doses were calculated as 0.85x10^{15} cm^{-2} and 1.48x10^{15} cm^{-2} by numerical integration of the doping profile from surface to junction which were measured by ECV as illustrated in *Figure 4.8*.

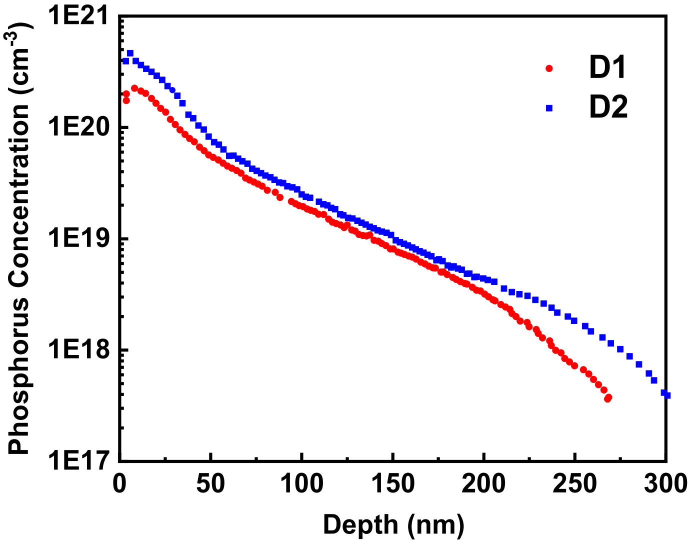

Figure 4.8 Emitter doping profiles named D1 (red) and D2 (blue), which were measured by ECV.

Figure 4.9 shows that iV_{oc} value of implanted emitter increases as the firing peak temperature approaches 710 °C, and it decreases dramatically above that temperature. This can be attributed to the variation in the diffusion kinetics of hydrogen (H) during the firing process [46][47][48]. The results indicate that the implanted emitter is very sensitive to the H diffusion mechanism, which is driven by the firing process. For the symmetrical emitter samples, we obtained iV_{oc} of around 645 mV after the samples were fired at peak temperature of 685 °C which was measured by a thermocouple attached onto a wafer moving on the conveyor belt.

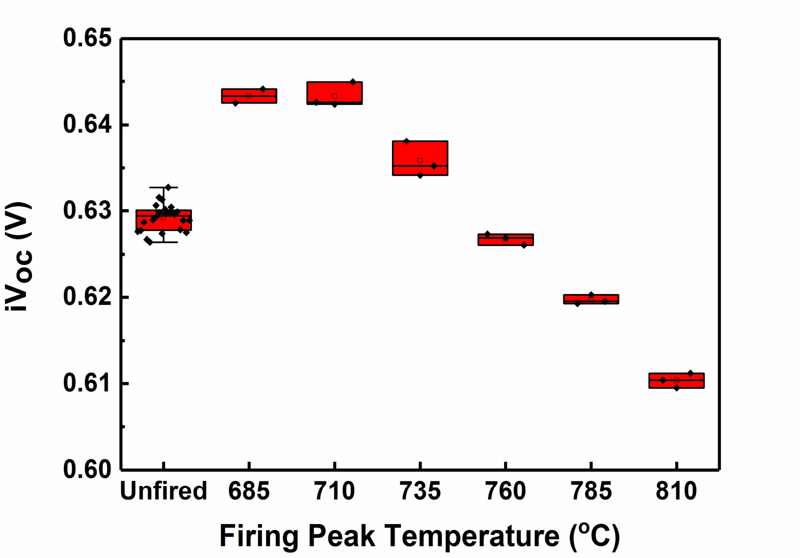

Figure 4.9 Effect of firing peak temperature on iV_{oc} of the symmetrical emitter with a dose of D1 at an illumination of 1 sun.

Rear Side:

In the fabrication of a standard PERC cell with a diffused emitter, a single side etching (SSE) process is applied to remove n^{++} region at the rear side of the wafer. It is expected that the surface recombination of the single side etched wafer will be lower than that of the textured one due to the smaller surface area, which in turn results in a higher V_{oc} [41]. On the other hand, the textured rear surface is desirable for reducing the processing steps for the fabrication of PERC cells. In this section, we studied iV_{oc} value variation of single side etched and textured rear surface for two distinct firing peak temperatures as 685 ºC and 810 ºC. For this, we fabricated two sets of symmetrical samples: one with textured and one with etched surfaces which were subsequently passivated with Al_2O_3/SiN_x stack layer. In the scope of this study, we also investigated the samples with two different Al_2O_3 thickness as 5 and 20 nm. As shown in *Figure 4.10*, not only Si surface structure and thickness of Al_2O_3 layer but also firing peak temperature has a very strong effect on iV_{oc} of the symmetrical rear surfaces coated with Al_2O_3/SiN_x stack passivation layer. The diminishing iV_{oc} with high firing temperature can be related to its effect on H diffusion as discussed for implanted samples. Moreover, the variation in iV_{oc} values with different Al_2O_3 thickness can be due to increasing thermal stability of passivation by decreasing Al_2O_3 thickness for fired Al_2O_3/SiN_x stack [49]. The results indicate that if the firing temperature and Al_2O_3 thickness are optimized, iV_{oc} values can increase up to around 675 mV on a textured rear surface having Al_2O_3/SiN_x stack passivation layer. This is comparable to those of 680 mV on average obtained with etched surfaces and could help for textured surfaces to be utilized as rear side of the cells.

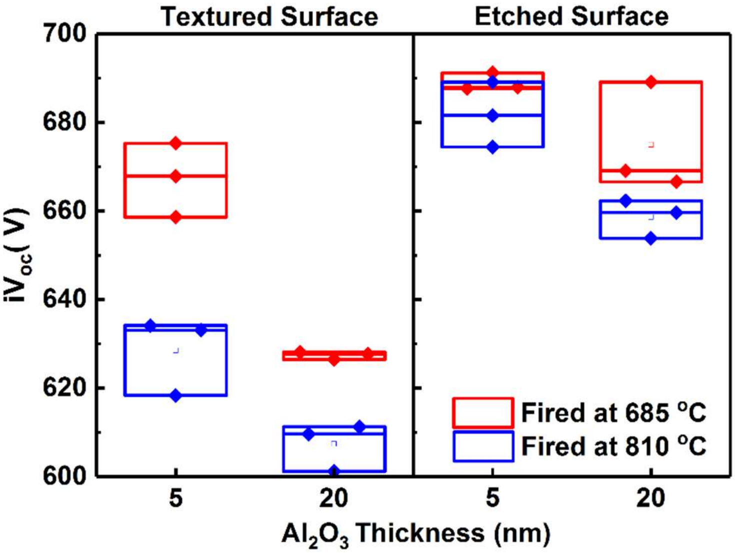

Figure 4.10 iV_{oc} of textured (left) and etched (right) surfaces passivated with either 5 nm or 20 nm Al_2O_3, which are capped with 120 nm SiN_x and fired at either 685 °C (red) or 810 °C (blue).

Solar Cell Characterization

Figure 4.11 shows the process flows applied in fabrication of implanted PERC cells with Al_2O_3/SiN_x rear passivation stack in the literature and our study. The red boxes in the (a) and (b) represent the process steps which were not utilized in our cell fabrication while they have been applied for rear surface processing in the literature [5],[39].

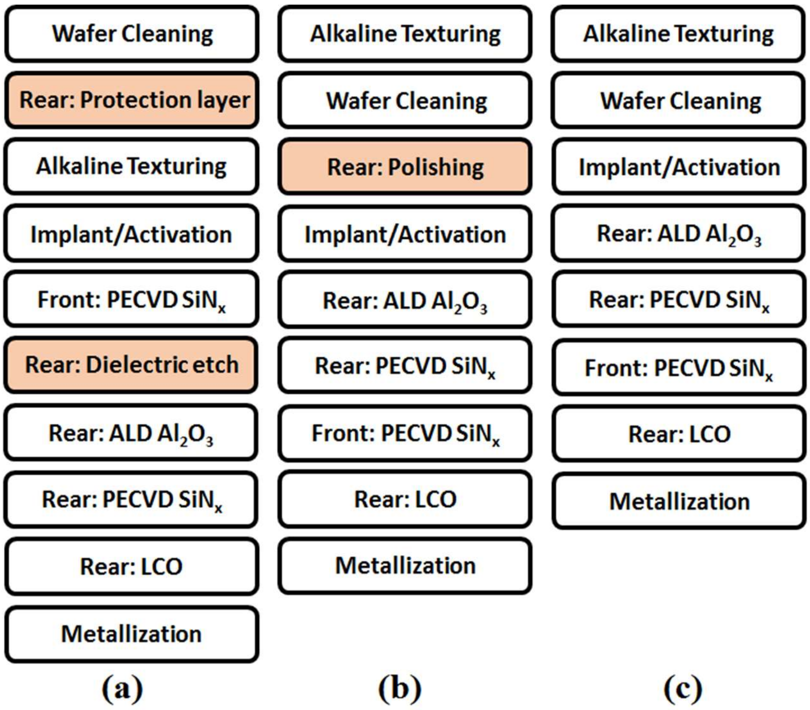

Figure 4.11 (a) and (b) depict the process flows for ion implanted PERC cells with Al_2O_3/SiN_x stack passivation in the literature, which were adapted from [5] and [39], respectively. (c) represents our simplified process flow. The process steps in red boxes were not included in our cell processes.

First Batch: Effect of Implant Dose and Firing Temperature on Cell Performance

In the first batch, the emitters of the PERC cells were implanted with two different doses as D1 and D2 and subsequently activated at 875 °C under N_2 flow. For the surface passivation of the implanted emitters, SiN_x layer was applied. Textured rear surfaces of the cells were identically passivated with 5nm Al_2O_3 capped with 120 nm SiN_x layer. The fabricated cells having two different emitter profiles were exposed to two distinct peak temperatures in the fast-firing process after the metallization. The solar cell parameters measured by solar simulator are given in Table 4.2. The implanted PERC cell with the name of D2-685, which has an implantation dose of D2 and was fired at a peak temperature of 685 °C, demonstrates the highest power conversion efficiency (PCE) of 20.0%. The trend for open circuit voltage (V_{oc}) values obtained on PERC cells by I-V measurement coincides with iV_{oc} values obtained by QSSPC measurement on symmetrical samples for both emitter and rear surfaces illustrated in *Figure 4.9* and *Figure 4.10*, respectively. On the other hand, V_{oc} is expected to be higher for lower phosphorus concentration due to a decrease in Auger recombination. This is however not observed for the fired samples, since the phosphorus doping profile affects the diffusion kinetics of H, which plays a role in the V_{oc} values [50]. The negative effect of firing at a peak temperature of 810 °C is clearly observed in V_{oc} and short circuit current density (J_{sc}) values. Moreover, J_{sc} was improved when the phosphorus implant dose was reduced from D2 to D1. This is due to the loss in short-wavelength response with a higher doping concentration in emitter as illustrated in *Figure 4.12*. Moreover, increasing phosphorus dose resulted in higher fill factor (FF) values, which is apparently due to enhancement in contact formation at the front side as depicted *Figure 4.13*.

Table 4.*2 Cell results from I-V curve showing the effect of implant dose and firing temperature on V_{oc}, J_{sc}, FF and efficiency*

Sample Name	Firing Peak Temp. (°C)	Efficiency (%)	V_{oc} (mV)	J_{sc} (mA/cm^2)	FF (%)
D1-685	685	19.9	648.1	38.6	79.4
D1-810	810	18.9	633.3	37.3	79.9
D2-685	**685**	**20.0**	**647.3**	**38.3**	**80.6**
D2-810	810	19.1	637.5	37.3	80.4

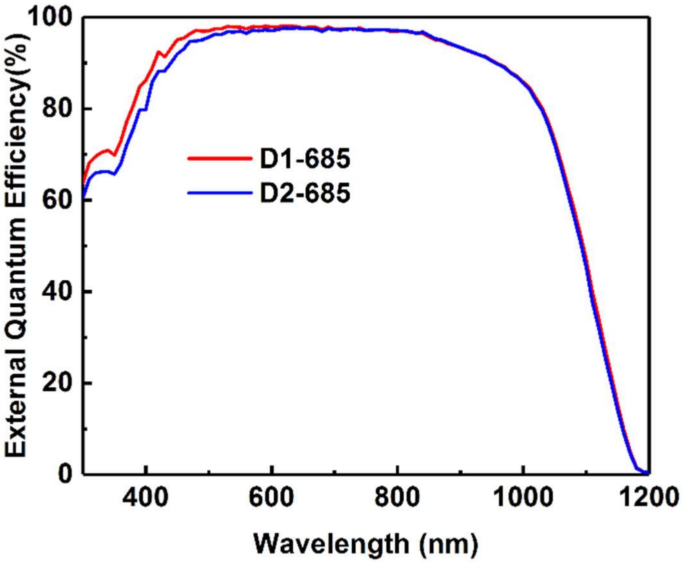

Figure 4.12 EQE graphs of the cells with emitters having implant doses of D1 (red) and D2 (blue), which were fired at a peak temperature of 685 °C

The contact resistivity values between the front metals and emitters measured on the fabricated solar cells are depicted in *Figure 4.13*. The contact resistivity increased with decreasing firing temperature, which is more noticeable for the emitter with a lower dose, D1. Nevertheless, the front contact quality is acceptable for each emitter and firing parameter.

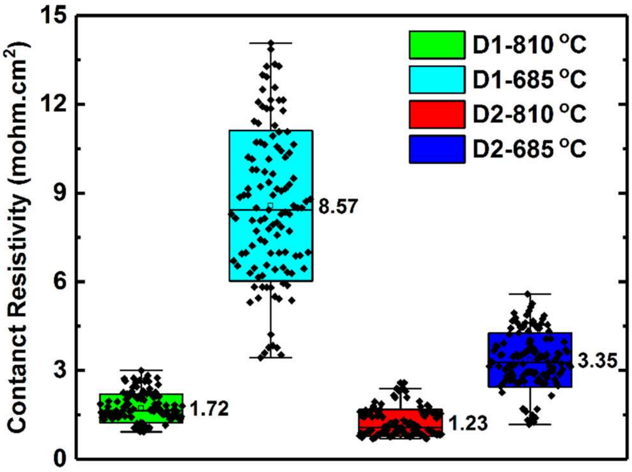

Figure 4.13 Effect of firing temperature on front metal contact and emitter with doses D1 and D2.

Second Batch: Effect of Al_2O_3 Thickness on Cell Performance

In this experiment set, the emitters of the cells were identically implanted with the dose named D2 and passivated with 75 nm SiN_x layer. For the passivation of the rear surface with Al_2O_3/SiN_x stack passivation, we examined two Al_2O_3 thicknesses as 5 nm and 20 nm. As shown in Table 4.3, Al_2O_3 thickness on the textured rear surface significantly affects the solar cell performance. The results show that the V_{oc} values of cell passivated with 20 nm Al_2O_3 are lower than those passivated with 5 nm Al_2O_3, which is consistent with QSSPC measurements on symmetrical samples illustrated *Figure 4.10*.

Table 4.*3 Our ell results from I-V curve showing the effect of Al_2O_3 thickness on V_{oc}, J_{sc}, fill factor (FF) and efficiency.*

Sample Name	Al_2O_3 thickness (nm)	Eff (%)	V_{oc} (mV)	J_{sc} (mA/cm^2)	FF (%)
D2-5	5	19.9	647.1	38.2	80.6
D2-20	20	18.5	628.6	36.5	80.5

Figure 4.14 clearly shows the loss in the current for the sample D2-20, which is due to the poor passivation of 20 nm Al_2O_3, leading to the loss in long-wavelength response. This result agrees with the ones obtained in the I-V measurement.

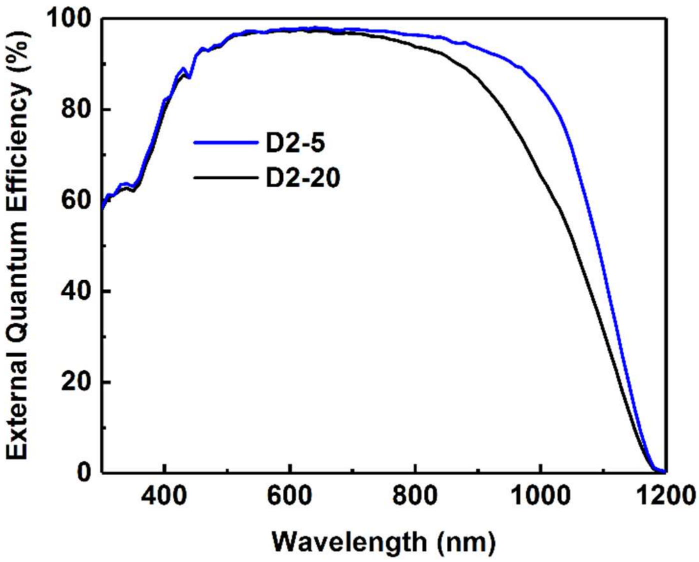

Figure 4.14 EQE graphs of the implanted PERC cells with 5 nm (blue) and 20 nm (black) Al_2O_3 layer capped with 120 nm SiN_x layer at the rear side.

In conclusion, we demonstrated a simplified process flow for the fabrication of ion implanted PERC cells having Al_2O_3/SiN_x stack passivation at the textured rear surface by eliminating the process steps such as rear surface polishing and protection. Our method has resulted in a PCE of 20.0% over the area of 244.3 cm^2. Specifically, we have optimized Al_2O_3 thickness and implantation dose along with the firing peak temperature on the symmetrical samples representing both the rear surface passivated with Al_2O_3/SiN_x stack layer and the emitter passivated with the SiN_x layer of this work can provide guidelines for the fabrication of highly efficient ion implanted PERC with a low workload and cost.

4.4 Optimization of Front and Rear Surface Dielectric Passivation Layers for Ion-Implanted PERC Solar Cells

In the previous section, we demonstrated the applicability of the ion implantation method for the fabrication of PERC solar cells. For the surface passivation and antireflective coating (ARC) at the front surface and capping layer on Al_2O_3 coated rear surface of PERC solar cells, SiN_x:H and SiO_xN_y:H layers are commonly used. Additionally, these passivation layers act as hydrogen (H) sources for the passivation of the silicon bulk defects and are barriers to avoid degradation [51]. The H concentration and the charge density of the dielectric material depend on its stoichiometry, which consequently determines the passivation quality and firing stability [52]. Also, the optical constants such as refractive index and extinction coefficient, thus reflection and absorption characteristics of the material are controlled by stoichiometry.

In this report, we present our study on the optimization of the dielectric layer for the front and rear sides of the ion-implanted PERC solar cells. We achieved a power conversion efficiency of (PCE) of 20.25% for the optimized dielectric layers at the front and rear surface of the PERC solar cell.

4.4.1 Experimental Details

Industrial p-type Cz-Si wafers with bulk resistivity of 1-3 Ω.cm underwent potassium hydroxide (KOH) solution for texturing to form random pyramids. Then, an ozone (O_3) based cleaning process was applied to remove organic and metallic contamination from the surface. Then, the samples were divided into three groups: one with a single side etched for solar cell, one with two sides textured for the symmetrical emitter, and one with two sides is etched for symmetrical rear surface fabrication. The rear surfaces of the wafers were etched to lower the surface area thus reducing surface recombination velocity. For the emitter formation, the front sides of solar cells and the double sides of the symmetrical samples were implanted with phosphorus (P) and annealed at 875 ºC under N_2 flow. After that, the samples were dipped into HF to remove the thin SiO_2 layer grown during the activation process. The rear sides of the cells and double sides of the symmetrical samples were identically coated with 5 nm Al_2O_3 by a spatial atomic layer deposition (ALD) tool. Then, the wafers reserved for the solar were divided into three groups named A1, A2, and A3. We deposited the same dielectric stacks at the front surfaces of the solar cells in group A1 and A2 but changed the one at the rear surfaces. The rear sides of the group A2 and A3 were deposited with the same dielectric stacks but the ones at the front surfaces were different. We also fabricated the symmetrical samples for each dielectric passivation layer on both emitter and etched rear surfaces. The front and rear dielectrics consist of various combinations of SiN_x:H and SiO_xN_y:H layers by the PECVD system. The thicknesses and optical constants of the dielectric layers deposited at the front and the rear surfaces are listed in Table 4.4. For the contact of metal at the rear surface of the solar cells, laser contact openings (LCO) were formed by a picosecond pulsed laser which operates at 532 nm (green) wavelength and 400 kHz pulse repetition rate (f_{rep}). Finally, metallization of the cells was carried out by screen printing, and they were co-fired for fire-through of silver (Ag) through dielectric at the front side and local Al-BSF formation at the rear side. The schematic of the fabricated PERC solar cells and the naming for the dielectric layers are depicted in *Figure 4.15*. The optical constants of the dielectric layers were measured by spectroscopic ellipsometry. The solar cells were characterized by current-voltage (I-V) measurements with a Class AAA solar simulator under standard test conditions. The lifetime measurements were performed on symmetrical samples with the photoconductance decay method (PCD) by the Sinton lifetime tester. The sheet resistances (R_{sheet}) and active dopant profiles of the emitter were measured by the four-point probe (4PP) and electrochemical-capacitance voltage (ECV) methods, respectively.

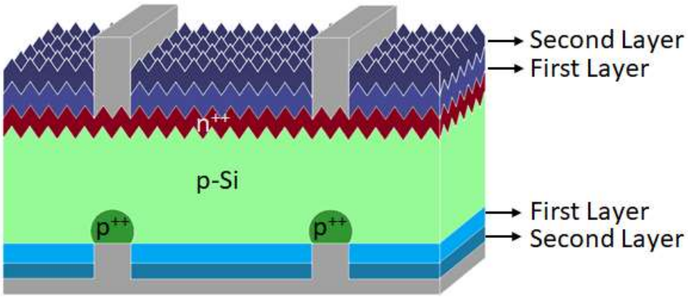

Figure 4.15 The first layer and second layer are components of the dielectric stacks deposited by the PECVD system.

4.4.2 Results and Discussion

R_{sheet} values of the emitters, which were identically implanted and activated, were measured around 56.9 ± 2.1 Ω/sq. The phosphorus doping profile named D2 is given in *Figure 4.8* (see Section 4.3.2).

The optical constants and thicknesses measured by spectroscopic ellipsometry are given in Table 4.4.

Table 4.4 *The thicknesses and optical constants of dielectric layers measured by spectroscopic ellipsometry*

Dielectric Name	***Layer***	***Material***	***n @632 nm***	***Thickness (nm)***
H1	First	SiN_x	2.18	21
	Second	SiN_x	1.99	55
H2	First	SiN_x	2.18	25
	Second	SiN_x	1.99	95
H3	First	SiN_x	1.96	120
	Second	-	-	-
H4	First	SiN_x	2.04	25
	Second	SiO_xN_y	1.73	64

The reflectance and absorbance of the dielectric ARC layers, H1 and H4, which were simulated from the optical constants and thicknesses of the samples, are depicted in *Figure 4.16.* The dielectric layer, H4, has a lower reflectance and absorbance in the UV spectrum, which in turn enhances the short circuit current density (J_{sc}).

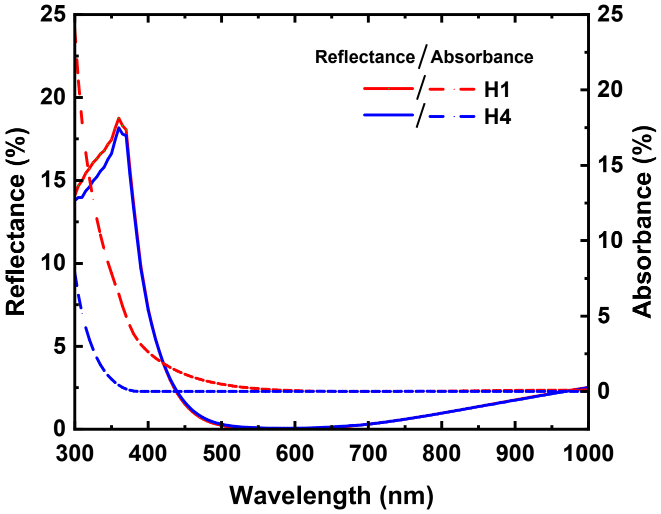

Figure 4.16 Reflectance and absorbance curves simulated from the optical constants and thicknesses of ARC layers named H1 (red) and H4 (blue) (simulated by OPAL2)

Figure 4.17 illustrates the iV_{oc} values of symmetrically etched p-Si wafers passivated with the dielectric stacks named Al_2O_3/H2 and Al_2O_3/H3. The iV_{oc} values of the samples were measured after the fast-firing process with a similar firing recipe of the fabricated solar cells to mimic hydrogen (H) release from dielectric layers to Si bulk. The results suggest the passivation of the Al_2O_3/H2 stack on the p-Si is poorer than that of the Al_2O_3/H3 stack. This can be due to an excessive H release from the first SiNx layer in the dielectric stack, which may result in the degradation of Si bulk.

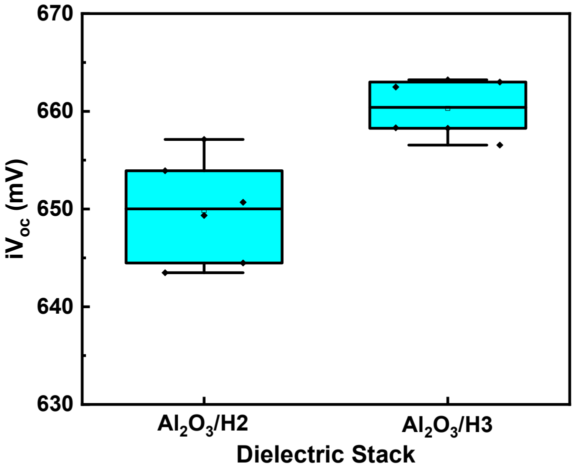

Figure 4.17 iV_{oc} values of symmetrically etched p-Si wafers passivated with dielectric stacks named H2 (magenta) and H3 (blue)

The solar cell parameters such as open-circuit voltage (V_{oc}) and short circuit current density (J_{sc}), fill factor (FF) and efficiency values measured by the solar simulator for the three groups of implanted PERC cells having different dielectric layers at the front and rear sides are shown in *Figure 4.18*. The solar cell groups named A1, A2 and A3, with different dielectric layers are described in Table 4.4. The increase in J_{sc} and V_{oc} for the sample group A2 compared to A1 is assumed to be due to the improvement of the rear dielectric layer since the front dielectric layers are identical. The enhancement can be attributed to better passivation of H3. When group A2 and group A3 are compared, the Al_2O_3 layers at the rear surfaces were capped with identical SiN_x:H layers named H4 while the front sides were deposited with either H1 or H4. The increase in J_{sc} values for group A3 is due to lower reflectance and absorbance of H4 at the front side as shown in *Figure 4.16*. Additionally, the increase in V_{oc} can be attributed to improved passivation of the emitter with H4 compared to H2.

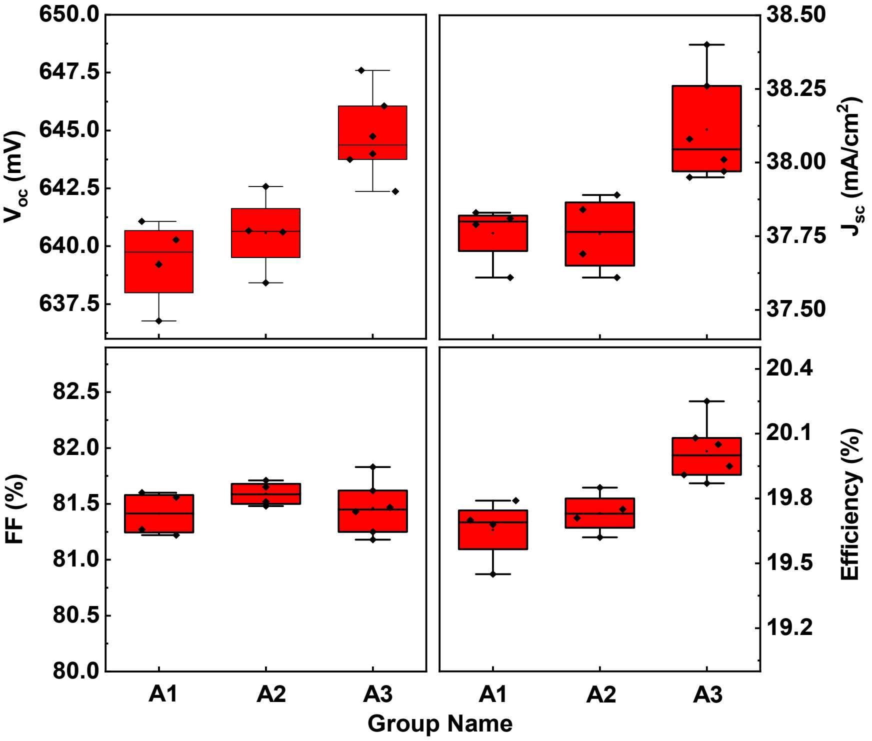

Figure 4.18 J_{sc} and V_{oc} values of the implanted PERC cells of three groups with different front and rear dielectric layers

The highest cell efficiencies from each group are depicted in Table 4.5. The maximum cell efficiency in group A3 is 20.25 % while that in group A1 is 19.79 %. The increase in V_{oc} can be attributed to improved passivation of front and rear surfaces. This is also confirmed with improvement in the iV_{oc} values of the rear surface passivated with H3. The increase in J_{sc} is due to the lower reflectance and absorbance as shown in *Figure 4.16*.

Table 4.5 *The measured solar cell parameters of the best cells from each group*

Group	*Front Dielectric*	*Rear Dielectric*	V_{oc} (mV)	J_{sc} (mA/cm^2)	*FF* (%)	η (%)
A1	H1	H2	641.07	37.83	81.60	19.79
A2	H1	H3	642.58	37.89	81.52	19.85
A3	H4	H3	647.60	38.40	81.43	**20.25**

Figure 4.19 demonstrates EQE graphs of the cells from each group. The better response in the IR region for A2 and A3 compared to A1 explains the improvement of rear dielectric layer. Similarly, the better response in the UV region for A3 compared to A1 and A2 proves the improvement for the ARC layer.

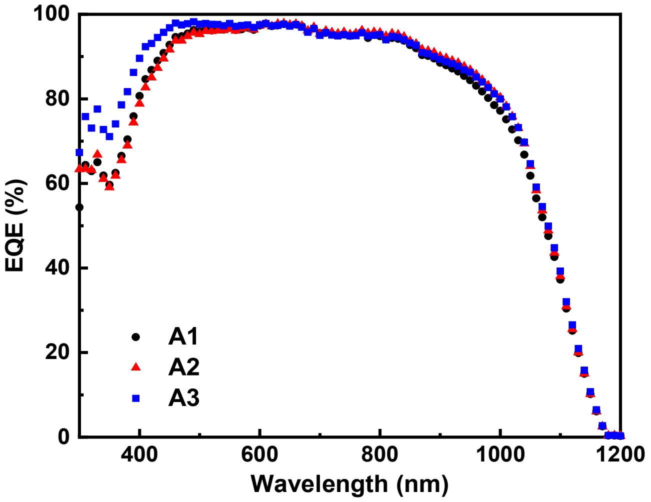

Figure 4.19 EQE graphs of the PERC cells with different front and rear dielectric layers

In conclusion, the front and the rear dielectric layer stacks have a significant effect on the ion implanted PERC solar cells. The cell performance can be improved by varying their stoichiometry, thus optical and electrical properties. The optical gain with the optimized ARC was illustrated with the reflectance and absorbance simulation results of the dielectrics, which are consistent with the EQE curves measured from the fabricated PERC solar cells. Additionally, the effect of the rear dielectric stack on the passivation was shown by iV_{oc}, EQE and J-V measurements. With the optimum dielectric stacks, we obtained a maximum of 20.25% PCE on the industrial size ion implanted PERC solar cells.

4.5 Summary

In the first section of this chapter, we analysed the doping profile of the implanted emitter by changing the implant dose and subsequent activation temperature. Our results indicated that the iV_{oc} of the emitter implanted with a relatively lower dose is very sensitive to the activation temperature. The highest average iV_{oc} was 648 mV for the emitter implanted with dose D2 and activation temperature of 875 ℃ [53].

In the second section, we presented the ECV and ToF-SIMS profiles to compare the activated dopant concentration and the total amount of phosphorus in the wafers.

In the third section, we demonstrated a simplified process flow for the fabrication of ion implanted PERC cells having Al_2O_3/SiN_x stack passivation at the textured rear surface by eliminating the process steps such as rear surface polishing and protection. Our method has resulted in a PCE of 20.0% over the area of 244.3 cm^2. Specifically, we have optimized Al_2O_3 thickness and implantation dose along with the firing peak temperature on the symmetrical samples representing both the rear surface passivated with Al_2O_3/SiN_x stack layer and the emitter passivated with the SiN_x layer. The obtained results of this work can provide guidelines for the fabrication of highly efficient ion implanted PERC with lowering the workload and cost in cell fabrication [38].

In the last section, we optimized the dielectric layers for the front and rear sides of the ion-implanted PERC solar cells. The implanted PERC cell with optimized dielectric layers showed a maximum efficiency of 20.25%.

CHAPTER 5

PASSIVATED EMITTER AND REAR TOTALLY DIFFUSED SOLAR CELLS

Passivated emitter and rear totally diffused (PERT) solar cells have been evolved from passivated emitter and rear locally diffused (PERL) type solar cells. At the beginning of the 1990s, PERL was introduced as an alternative concept to reduce the recombination losses in the metal and silicon interface [54]. In PERL solar cell design as shown in *Figure 5.1*, highly doped regions are formed under the metal contact to minimize the recombination losses in the metal silicon interface at the rear side [55].

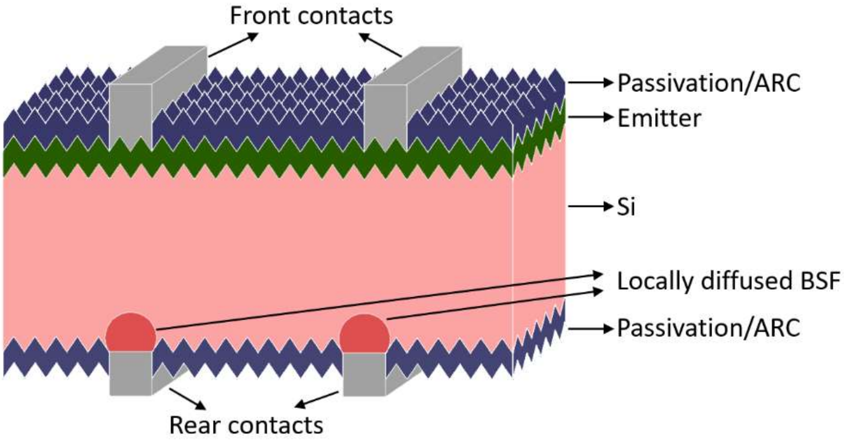

Figure 5.1 The schematic of a PERL solar cell (adapted from [55].)

In this design, a fully diffused junction is formed at the rear side which is subsequently passivated with a dielectric material. Shortly after the introduction of the PERL structure, PERT came to the fore with similar concerns for reducing the recombination on the backside. Unlike the PERL, the rear side of the cell is totally diffused in this design. The emitter of the PERT cells can be at the front and rear sides with the local metal contacts [56]. The schematic of a typical PERT solar cell is given in *Figure 5.2*.

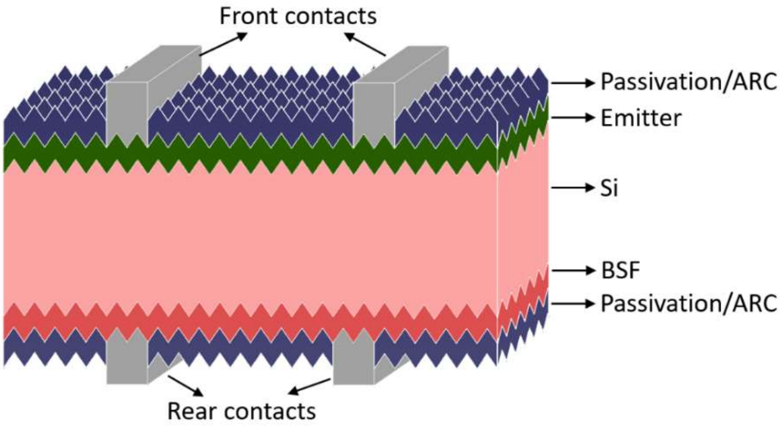

Figure 5.2 The schematic of a PERT solar cell (adapted from [56])

Conventional PERC solar cells are produced on p-type wafers; however, it is forecast that n-type wafers will increase their share in the near future due to their higher bulk lifetime. Silicon heterojunction (SHJ), passivating contacts, interdigitated back contact (IBC), and passivating emitter rear totally diffused (PERT) solar cells are the mainstream technologies, which are quite applicable on n-Si wafers. In addition, bifacial solar cells, which are capable of absorbing irradiation from their front and rear sides, become more attractive since their potential to generate more power from a single solar cell [57]. The use of light from both sides of the cell also allows the vertical mounting of the solar panels, which brings about some advantages. The irradiance received by vertically mounted modules typically has two peaks on a certain day appearing one in the morning and one in the afternoon. This can lead to a higher energy yield depending on the various parameters such as the latitude, albedo (the light reflected from the ground) and diffuse light from the sky and the ground [58]. Moreover, the vertical mounting of the panels can solve the soling and snow coverage problems [59]. For both vertical and horizontal mounting of solar panels with a certain tilt angle, the bifaciality factor is a very critical parameter for higher performance. As the albedo increases the bifaciality gains more and more importance [60][61][62]. The bifaciality factor of a conventional PERC solar cell is typically around 0.7; however, it can readily exceed 0.9 for SHJ, passivating contact and PERT solar cells. When the cell process flows are considered, the current PERC solar cell production lines seem to be more convenient to be adapted for PERT solar cell fabrication due to more similar processing. PERT solar cells have been already extensively studied in the literature with various fabrication methods [63][64][65][66][67][68][69][70][71][72][73][74][75][76][77].

In the following sections of this chapter, we present the experimental results of fully and partially ion-implanted PERT solar cells.

5.1 Fully Ion Implanted n-PERT Solar Cells: Separate and Co-activation of Boron with Phosphorus Dopants

N-type wafers take advantage of a higher minority carrier lifetime than p-type wafers and a lack of light-induced degradation due to the absence of boron-oxygen (B-O) complexes and their resistance to metal impurities [78]. Thus, n-PERT solar cells are quite promising designs for their high-efficiency potential. Although the price of n-type wafers has been estimated 8% more expensive than p-type due to the difference in brick cost [79], it is projected that the market share of n-type solar cells will increase in the solar energy market [80].

Boron (B) and phosphorus (P) atoms are typical dopants implanted for formation of emitter and back surface field in n-Si solar cells, respectively. Following ion implantation, an annealing process is required for the electrical activation of the dopants introduced into Si. While implanted B atoms are usually activated above 1000 ^{o}C for dissolution of dislocation loops, P atoms are activated below 900 ^{o}C [6][81][82][83]. Electrical activation of implanted P can be carried out simultaneously with B dopants at high temperatures or separately at lower temperatures. Co-activation of P with B is convenient to reduce the number of process steps for solar cell fabrication; however, it has been shown that separate activation steps are necessary to reach higher cell efficiencies [83][84].

Here, we investigate the effect of separate activation of P at a low thermal budget and its co-activation with B at a high thermal budget on iV_{oc} values of the symmetrical samples and the performance of n-PERT solar cells. For this study, we fabricated four batches of samples including either symmetrical samples or n-PERT solar cells. In the first batch, the effect of the activation and firing temperatures on the iV_{oc} values of symmetrically P implanted and SiN_x passivated n-Si wafers is discussed. In the second batch, we show how high and low thermal budgets for P activation influence n-PERT solar cells. In the third batch, we investigated the effect of Al_2O_3/SiN_x stack layer deposited on the n^{++} region of n-PERT solar cells before IBC solar cell studies. This is critical for the IBC solar cells since p^{++} and n^{++} regions at the same surface of the device are passivated with an identical passivation stack. It is also known that Al_2O_3/SiN_x has superior passivation on p^{++}, which constitutes the larger fraction of the rear surface of n-IBC solar cells. Therefore, we tested the Al_2O_3/SiN_x on n^{++} of n-PERT solar cells which is fabricated relatively than IBC. In the last batch, the performances of n-PERT solar cells fabricated on two different wafer brands were compared.

5.1.1 Experimental Details

Alkaline textured and ozone (O_3) cleaned industrial 156.75x156.75 mm^2 n-type Cz wafers with bulk resistivity of 1-3 Ω.cm were used as substrates.

First Batch: P implantation with identical doses at an energy of 10 keV was performed on either one side or the double sides. Following the implantation process, surface cleaning was performed again to remove contaminants that can come from the sample holder, sample handling, or the implantation process itself. Then, the samples were separated into two groups to be activated at either 875 °C or 1050 °C under nitrogen flow for 30 minutes. Similarly, a group of unimplanted textured wafers was also annealed at 875 °C and 1050 °C to investigate the effect of annealing conditions on the bulk n-type Si. After all the implanted and unimplanted samples were dipped into HF to remove unintentionally grown thermal oxide during activation, double side implanted samples were coated with PECVD:SiN_x layers and exposed to a firing process in a conveyor belt furnace to release H atoms from SiN_x:H layer to the Si bulk. The temperature of the wafers was measured by a thermocouple attached to an identical wafer moving with the same conveyor speed. Symmetrical samples were used for iV_{oc} measurements after every process step with the photo-conductance decay (PCD) method using a Sinton tool. Additionally, photoluminescence (PL) images of the fired samples were taken by the Semilab PLI-1001 tool. Sheet resistance (R_{sheet}) and doping profile measurements were performed on single side implanted samples by the four-point probe and electrochemical capacitance-voltage (ECV) methods, respectively.

Second Batch: The process flows for the cell fabrication with separate and co-activation are shown in *Figure 5.3*. For the metallization of the samples, AgAl on the p^{++} and Ag on the n^{++} side were screen printed. Then, the samples were exposed to a fast-firing process for fire-through on the metal pastes through dielectric layers.

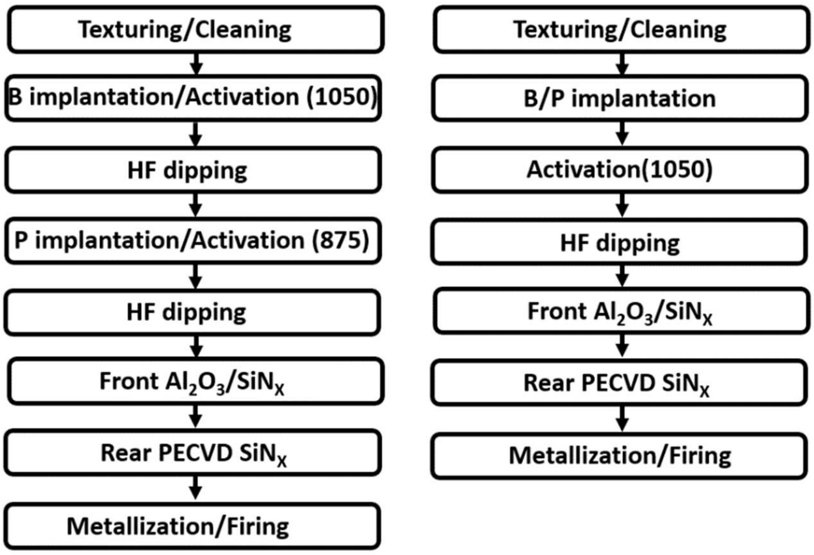

Figure 5.3 Process flows for the fabrication of separately activated (left) and co-activated (right) n-PERT solar cells.

Third Batch: For the cell fabrication, in addition to the separate activation process flow given in *Figure 5.3*, we also included deposition of 2 nm or 4 nm ALD:Al_2O_3 on n^{++} before the deposition of SiN_x.

Fourth Batch: We fabricated n-PERT solar cells to compare their performance on two different wafer brands. The solar cells were fabricated with the same process flow as the third batch, which resulted in the highest solar cell performance. Thus, we applied separate annealing processes for activation of B and P. Also, the n^{++} region was passivated with a 2 nm Al_2O_3 and 75 nm SiN_x stack layer.

5.1.2 Results and Discussion

First Batch: Effect of Activation Temperature of Implanted Phosphorus on iV_{oc} Variations During Firing Process

Table 5.1 represents R_{sheet} values measured on single side implanted and activated n-type Si wafers. The results given in the table are an average of 25 points measured on the identical wafers for each parameter. For a similar implantation dose, activation at an annealing temperature of 875 °C and 1050 °C leads to R_{sheet} values of 54.3 and 37.3 Ω/sq., respectively.

Table 5.1 *R_{sheet} values of the samples measured by four-point-probe.*

Sample Name	Activation Temperature (°C)	Sheet resistance (Ω/sq.)
D1-875	875	54.3±1.7
D1-1050	1050	37.3±1.3

Figure 5.4 shows the measured ECV profiles of the samples named D1-875 and D1-1050, which were activated at 875 °C and 1050 °C for 30 minutes, respectively. An increase in annealing peak temperature from 875 °C to 1050 °C leads to a serious decrease in peak doping concentration from 2.32×10^{20} cm^{-3} to 5.06×10^{19} cm^{-3} and a deeper junction for P atoms in n-type Si wafers.

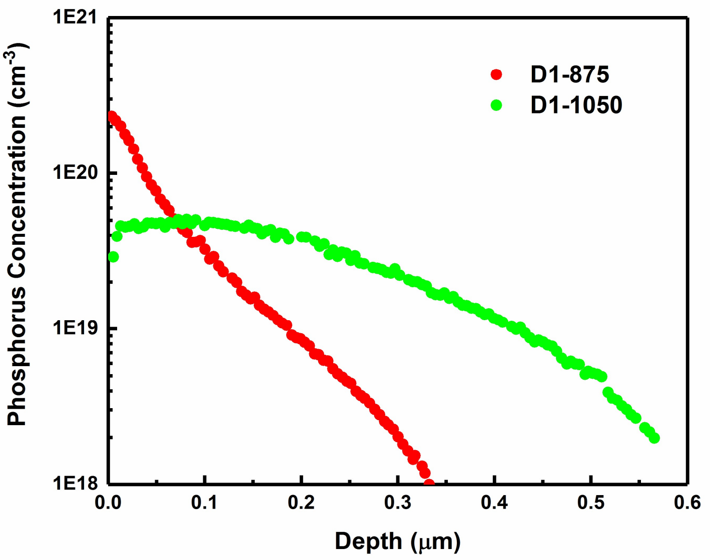

Figure 5.4 Doping profiles of P implanted n-Si, which were activated at 875 ºC (red) and 1050 ºC (green) for 30 minutes.

Figure 5.5 depicts the effect of the doping profile obtained by two distinct activation temperatures as 875 ºC and 1050 ºC on iV_{oc} values of the P implanted n-Si symmetrical samples ($n^{+}nn^{+}$) measured after activation, SiN_x deposition, and firing processes. After the activation process (red boxes), the measured average iV_{oc} values of the samples annealed at 1050 ºC are lower than those activated at 875 ºC. This may be mainly due to the degradation of the bulk lifetime of the Si wafer after the high-temperature annealing process [82]. Following the deposition of SiN_x, the samples were exposed to the firing process at a peak temperature of 810 ºC, leading to an increase of iV_{oc} values of D1-875 while decreasing in those of D1-1050 compared to their initial values (green boxes). It has been discussed in the literature that H release from SiN_x:H increases significantly above 700 ºC [46][47]. Thus, degradation may be related to excessive H diffusion into Si, pronounced with the lower surface doping concentration [50].

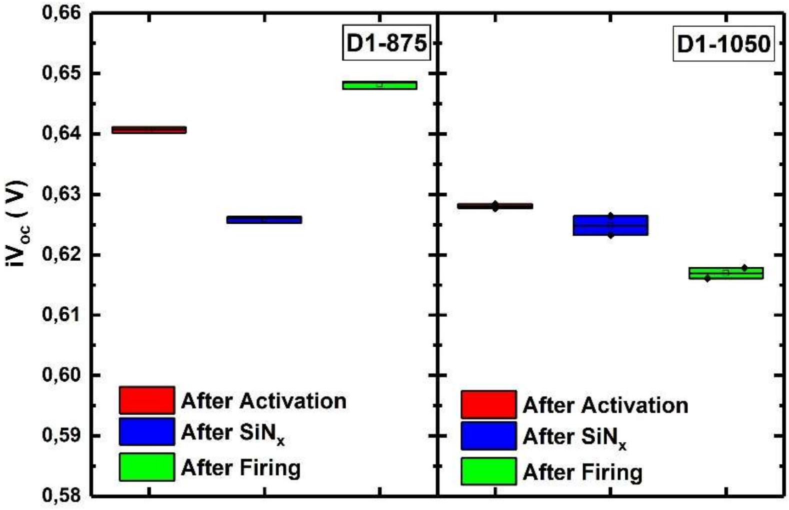

Figure 5.5 iV$_{oc}$ values of the samples after activation, SiN$_x$ deposition, and firing processes.

As illustrated in *Figure 5.6*, PL images of the fired samples also confirm the iV$_{oc}$ results. The increase in defect density results in a lower PL density; that is, we can interpret that the sample annealed at a higher activation temperature has a higher recombination rate, thus a lower iV$_{oc}$.

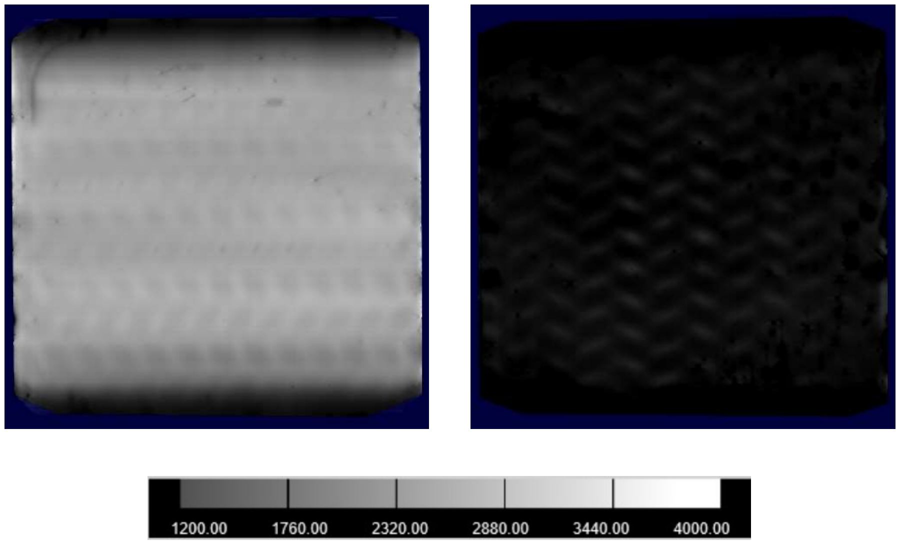
D1-875 **D1-1050**

Figure 5.6 PL images of the samples named D1-875 and D1-1050 after firing process at a peak temperature of 810 °C.

Moreover, we extensively studied the effect of firing peak temperatures on iV_{oc} of the implanted and unimplanted symmetrical samples. As can be seen in *Figure 5.7*, the trend of iV_{oc} variation according to the firing peak temperature is different for the two doping profiles. This can be also attributed to changes in the H diffusion mechanism due to different doping profiles [50]. iV_{oc} decreases with an increase in firing peak temperature for the deeper doping profile with lower surface doping concentration; while it initially increases and then decreases after a certain peak temperature around 735 °C for the shallower doping profile with higher surface doping concentration. Nevertheless, the iV_{oc} value of P implanted n-Si is higher for activation temperature of 875 °C for any firing temperature.

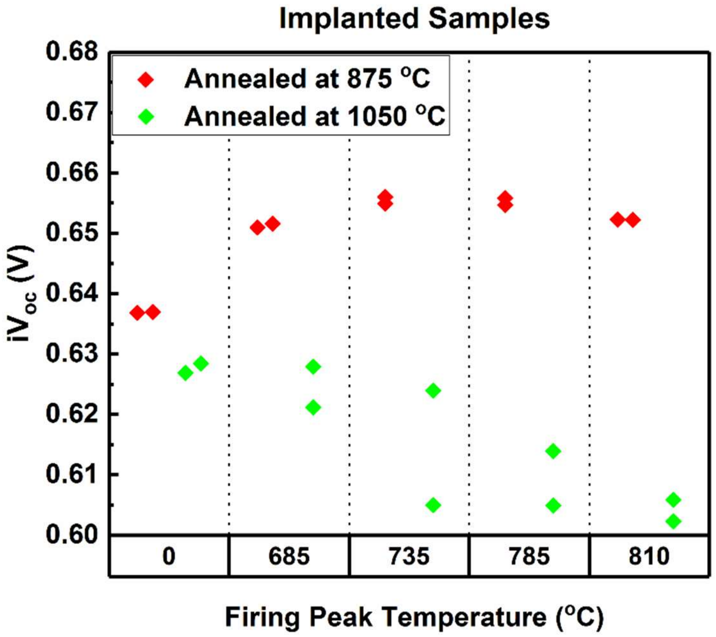

Figure 5.7 Effect of firing peak temperature on iV_{oc} values of P implanted n-type Si wafers, which were activated at 875 °C (red) and 1050 °C (green)

In the literature, it has been discussed that the dissolution of oxygen precipitates in crystal Si at temperatures above 1000 °C results in the formation of metastable defects, thus a decrease in a bulk lifetime [85]. To investigate the effect of low and high-temperature annealing on the bulk quality of the wafers, we repeated the same experiment on unimplanted n-Si. *Figure 5.8* illustrates the firing dependence of iV_{oc} of the n-type wafers annealed at high and low temperatures. Although the wafers annealed at 1050 °C become susceptible to high firing temperatures, the decrease in iV_{oc} values of the unimplanted wafers with increasing firing peak temperature is not as significant as that of implanted wafers.

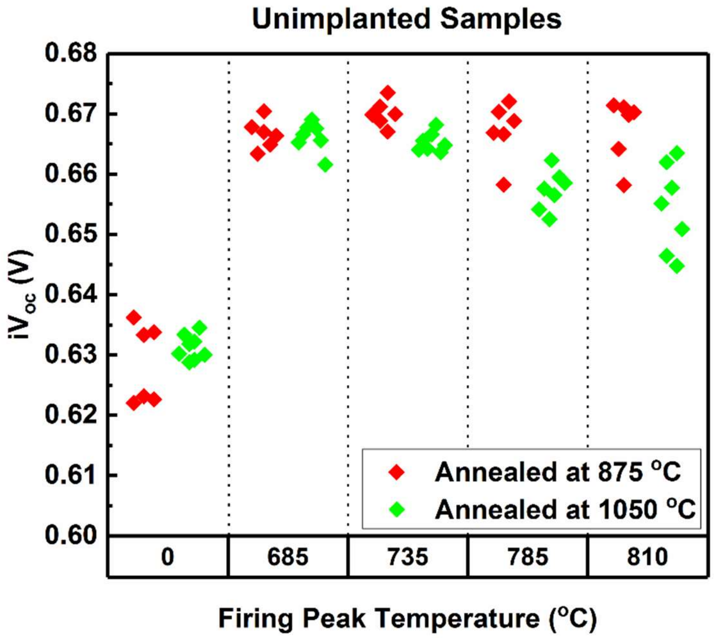

Figure 5.8 Effect of firing peak temperature on iV_{oc} values of unimplanted n-type Si wafers, which were annealed at 875 °C (red) and 1050 °C (green)

Second Batch: Comparison of n-PERT Solar Cells with Separately or- Co-Activated Phosphorus Implanted Back Surface Field (BSF)

Table 5.2 shows the solar cell parameters obtained on the fabricated n-PERT solar cells by a Class AAA solar simulator. Our results suggest that the V_{oc} and J_{sc} values are higher for separately activated cells, which is also consistent with the symmetrical lifetime samples. FF values of separately activated solar cells are relatively lower than the co-activated ones since the deeper doping of phosphorus is expected to have a lower contact resistivity. Our best solar cell showed an efficiency of 17.77% with the bifaciality factor of 0.96.

Table 5.2 *The solar cell parameters measured from front and rear sides of the best cells from each group*

Activation	*Measured side*	V_{oc} (mV)	J_{sc} (mA/cm^2)	*FF* (%)	η (%)	Bifaciality factor
Separate	Front	624.49	37.66	75.57	17.77	0.96
	Rear	623.75	36.40	75.17	17.07	
Co-activation	Front	615.55	36.95	76.46	17.39	0.88
	Rear	612.14	32.64	76.80	15.34	

Figure 5.9 shows the contact resistivity values obtained on the fabricated solar cells after they were cut into stripes for TLM measurement. It is seen from the graph that the contact resistivity between Ag and n^{++} shows a wide range of variation over the wafer and has a mean value that is significantly higher than the co-activated samples. The lower FF values for the co-activated samples can be explained by the lower contact resistivity of Ag and n^{++}. It has been already discussed that the contact resistivity decreases as the doping level gets deeper [34]

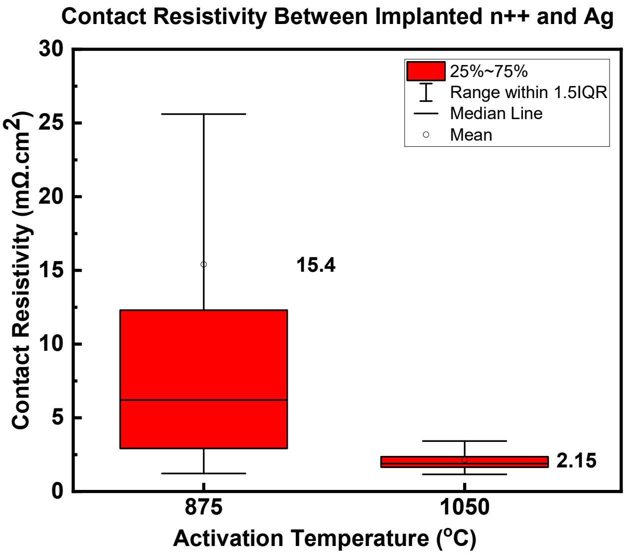

Figure 5.9 Effect of activation temperature on the contact resistivity between screen printed Ag and implanted n^{++}

The high contact resistivity between screen-printed Ag and BSF results in a significant loss in FF values of the fully implanted n-PERT solar cells when the P is activated separately at a relatively lower thermal budget than B. It is speculated that the moving charged particles, most likely H may be one of the main reasons for increasing contact resistance[86][87]. H is mostly provided by the SiN_x:H dielectric layer into Si and can be manipulated with some parameters like SiN_x stoichiometry, firing peak temperature, doping profile, defect density, and another dielectric layer in the interface of SiN_x and n^{++}.

Third Batch: Towards N-Type Interdigitated Back Contact Solar Cells: Passivation of n^{++} and p^{++} Regions with Al_2O_3/SiN_x Stack Layer

Since n^{++} and p^{++} regions are placed at the same surface of the interdigitated back contact (IBC) solar cells, they are passivated with the same passivation layer. In the case of n-type IBC solar cells, emitter (p^{++}) constitutes the larger fraction of the rear surface. It is also known that Al_2O_3/SiN_x stack layer is superior passivation on the p^{++} region. Thus, passivation of n^{++} with the same stack is also required in the case of IBC solar cells. Here, we investigate the effect of Al_2O_3 within the Al_2O_3/SiN_x stack layer on the passivation of n^{++} region on n-PERT solar cells. In this context, we fabricated a batch of fully ion-implanted n-PERT solar cells which have separately activated BSF. The process flow is similar to the separately activated one in *Figure 5.3*, except for the rear surface passivation layer. Here, we deposited ALD:Al_2O_3:H with thicknesses of 2 nm or 4 nm beneath the PECVD SiN_x:H on the n^{++} region.

Our process flow in this experiment is similar to the separately activated one in *Figure 5.3*, except for the rear surface passivation layer. Here, we deposited ALD Al_2O_3 with a thickness of 2 nm or 4 nm beneath the PECVD SiN_x:H on the n^{++} region. In Table 5.3, we compared the cell results in this batch and the previous one without the Al_2O_3 layer in the interface of n^{++} and SiN_x:H. Each group includes two identical samples.

According to our IV results, it is clear that the solar cells with both 2 nm and 4 nm Al_2O_3 layer beneath the SiN_x layer on the n^{++} region have higher efficiency compared to the ones in the previous batch. The main improvement is due to the higher FF values in this batch. This can be attributed to the change in the kinetics of H release from SiN_x to Si since Al_2O_3 layer acts as an H source and H barrier [88]. The excessive H can inactivate the dopants below the metals and leads to a poorer contact. In the existence on Al_2O_3 layer, the amount of H beneath the metal contact and BSF may be lower. Besides, V_{oc} and J_{sc} values in the second batch are very similar to the previous set, indicating a comparable passivation of Al_2O_3/SiN_x stack with SiN_x on n^{++}. The best result was obtained for the passivation with 2 nm Al_2O_3 and SiN_x stack on n^{++}. The highest efficiency was measured as 19.2% with bifaciality of 88%.

Table 5.3 *I-V results of the fully implanted n-PERT solar cells*

Passivation Layer on n^{++} and Sample Name	*Measured Side*	V_{oc} (mV)	J_{sc} (mA/cm^2)	*FF* (%)	η (%)
Only SiN_x-1	Front	624.49	37.66	75.57	17.77
	Rear	623.75	36.40	75.17	17.07
Al_2O_3(2 nm)/SiN_x-1	Front	626.46	37.79	81.12	**19.20**
	Rear	624.32	33.68	80.33	16.89
Al_2O_3 (2 nm)/SiN_x-2	Front	624.32	37.73	81.11	19.16
	Rear	623.58	33.49	81.11	16.95
Al_2O_3 (4 nm)/SiN_x-1	Front	621.53	37.53	80.95	18.88
	Rear	618.42	33.34	80.36	16.90
Al_2O_3 (4 nm)/SiN_x-2	Front	621.59	37.48	81.10	18.89
	Rear	618.78	34.12	80.63	17.02

Figure 5.10 illustrates the contact resistivity values measured on the stripes cut from fabricated n-PERT solar cells. The red and green boxes represent the metal contacts of n^{++} and p^{++} regions, respectively. It can be inferred from the graph that the Al_2O_3 layer in the interface of implanted n^{++} and SiN_x:H layer significantly enhances the metal contacts. The improvement in FF of the solar cells compared to the ones in the previous batch can be attributed to the enhancement of the metal contacts in the n^{++} region.

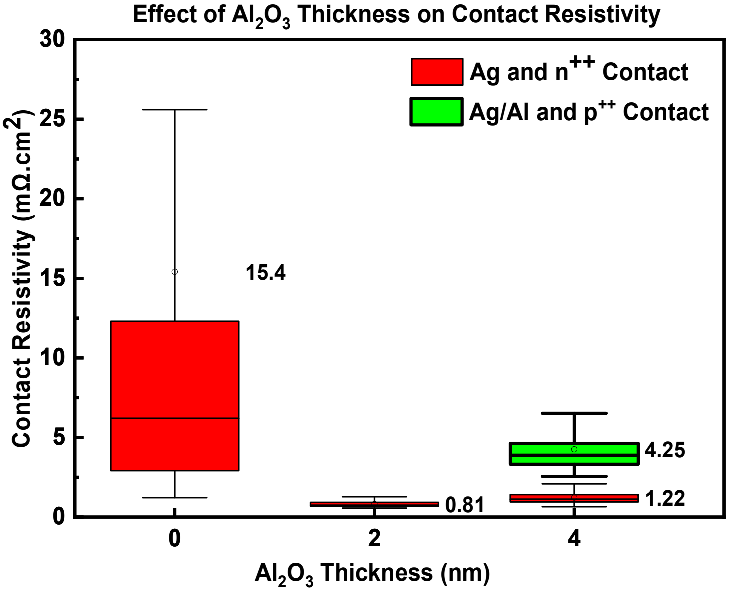

Figure 5.10 Effect of Al_2O_3 thickness on the contact resistivity on screen printed metal and implanted Si

Fourth Batch: Comparison of Fully Ion-Implanted PERT Solar Cells Made of n-Si Wafer from Different Vendors

The average R_{sheet} values of the emitter and BSF on n-Si wafers were measured as 100.6 Ω/sq and 33.4 Ω/sq, respectively. The corresponding ECV graphs are given in *Figure 5.11*. Active dopant doses were calculated as 1.16E15 cm^{-2} for B and 1.76E15 cm^{-2} for P.

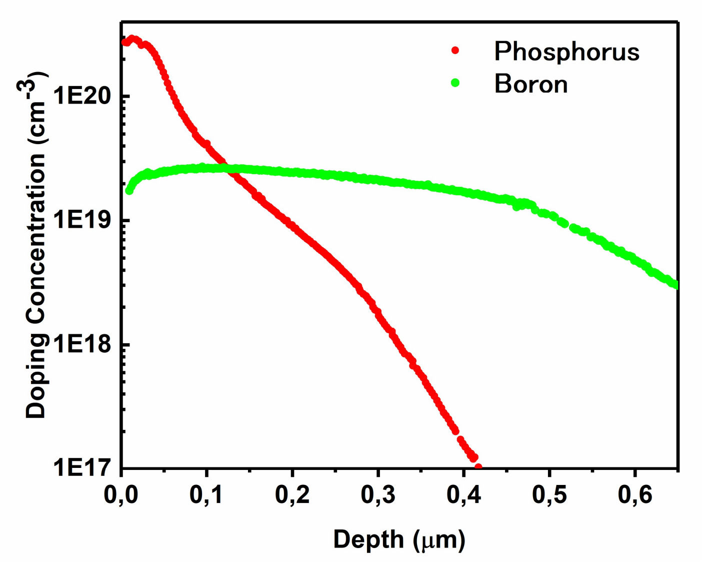

Figure 5.11 ECV graphs of implanted emitter (green) and BSF (red)

The iV_{oc} values measured on the symmetrically implanted and passivated n-type wafers from the two companies are shown in *Figure 5.12*. The average iV_{oc} for the emitter samples is around 624 mV and 623 mV for V2 (named V2-B) and V1 (named V1-B) wafers, respectively. Additionally, the average iV_{oc} values of the BSF samples are measured as 641 mV for V2 and 642 mV for V1 wafers.

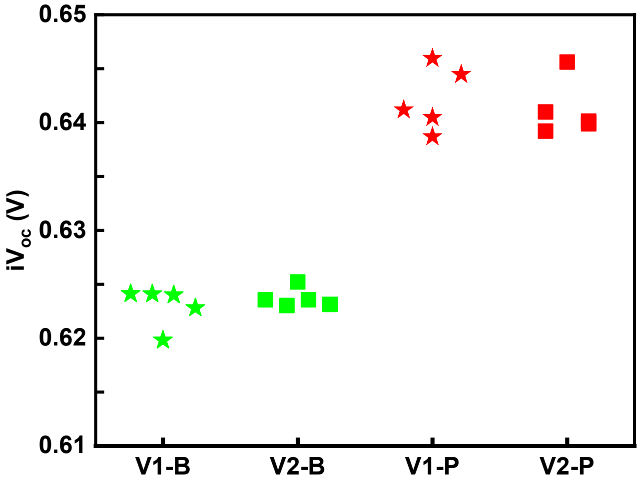

Figure 5.12 iV_{oc} of symmetrically implanted and passivated emitter (green) and BSF (red) formed on V1 (star) and V2 (square) wafers.

The solar cell parameters obtained by I-V measurement are given in Table 5.4.

Table 5.4 *The solar cell parameters measured by the solar simulator on the bifacial n-PERT cells fabricated on V1(named V1-1 and V1-2) and V2 (named V2-1 and V2-2) wafers*

Sample Name	*Measured Side*	V_{oc} (mV)	Jsc (mA/cm^2)	FF (%)	PCE (%)
V1-1	Front	629.5	38.1	80.4	**19.3**
	Rear	625.4	33.5	80.0	16.8
V1-2	Front	628.7	38.2	80.5	**19.3**
	Rear	625.0	33.5	80.1	16.8
V2-1	Front	629.5	38.1	80.1	19.2
	Rear	625.7	32.8	79.8	16.3
V2-2	Front	630.4	37.9	79.8	19.1
	Rear	626.0	33.0	79.2	16.4

V_{oc} values are measured as around 630.0 mV at the front side of the solar cells made of V1 and V2 wafers. This implies a similar wafer quality for the two brands. The front efficiency of the champion cells is around 19.3% and 19.2% for the fabricated cells from V1 and V2 wafers, respectively. The 0.1% difference in the efficiency of the solar cells from the two wafer brands is due to a difference in fill factor (FF). This can be due to unalike metallization quality for the cells.

In conclusion, we studied the effect of separate and co-activation of P with B atoms on iV_{oc} values of symmetrically P-implanted and passivated n-type c-Si. Our results showed that. iV_{oc} values of the samples activated at 1050 °C significantly decrease while those for the samples activated at 875 °C increase at a typical firing peak temperature which is generally applied for fire-through contact formation. Also, iV_{oc} values of P implanted and unimplanted c-Si, which were activated at both high and low temperatures showed a strong dependence on peak firing temperature. Moreover, the I-V results of the n-PERT solar cells having either separately or co-activated P implanted back surface field were also consistent with the results of symmetrical samples. Finally, we fabricated fully ion implanted n-PERT solar cells and symmetrical samples on the n-Si wafers obtained from two different vendors to compare their quality. The highest front photo-conversion efficiencies are measured as 19.3% and 19.2% with bifaciality (η_{rear}/η_{front}) of 86.8% and 85.1% for the solar cells made of V1 and V2 wafers, respectively. The V_{oc} values of the solar cells and iV_{oc} values of the symmetrical emitter and BSF samples fabricated on n-Si wafers from the two companies are almost equal, implying similar wafer qualities from the device point of view.

5.2 Determination of Boron Doping Profiles by the ECV and ToF-SIMS Methods

Here, we compare the inactive and active B doping profiles on samples which are formed on the nearly polished (saw damage etched) n-Si wafers. The samples were implanted with a certain dose and activated at 1050 °C for 30 minutes under N_2 flow in an atmospheric annealing furnace. For the textured samples, the same doping dose was obtained by increasing the ion exposure time proportional to the surface roughness of the wafer. After the activation process, the samples were dipped into an HF solution and deposited with a PECVD: SiN_x layer. Finally, following a fast firing process, the SiN_x layers were etched away by the HF dipping process. From the ECV and ToF-SIMS graphs in *Figure 5.13*, it is clearly seen that there are inactive dopants at the surface of the wafer, which is quite lower compared to P-implanted samples which were typically activated at 875 °C in this thesis. The dose of the dopants is calculated by integrating the profiles from surface to junction, which is 1.27E15 cm^{-2} and 1.20E15 cm^{-2} for the ToF-SIMS and ECV curves, respectively. For the textured samples, the same doping dose is obtained by increasing the ion exposure time proportional to the surface roughness of the wafer.

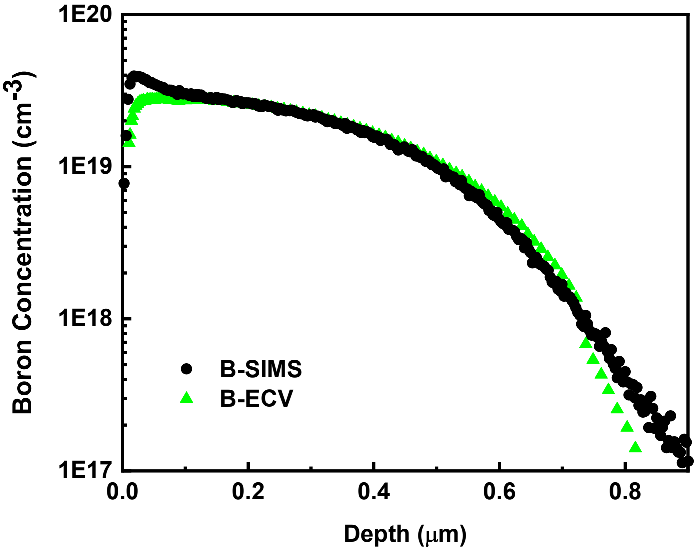

Figure 5.13 The active (green) and total (black) B doping profiles measured by ECV and ToF-SIMS, respectively.

5.3 Bifacial N-PERT Solar Cells Fabricated by Alternative Industrial Manufacturing Methods

One of the challenges for the fabrication of the PERT solar cells is the existence of the two doping steps for the rear and front surfaces which necessitates doping of one side while protecting the other at least once. On the other hand, single side doping methods such as ion implantation can help reduce the process complexity.

The p^{++} region in PERT solar cell is typically formed by B doped by various methods like ion implantation and high temperature diffusion furnaces. The thermal budget for activation of the implanted B atoms is relatively higher than the diffusion process. This high temperature annealing for activation after the B implantation process is harmful for the bulk lifetime of the Si wafer due to the formation of oxygen precipitation. The n^{++} region is typically created by P doping, which can be conducted by ion implantation or diffusion furnaces. Luckily, the implanted P can be activated at lower annealing temperatures around 850 °C similar to typical $POCl_3$ diffusion processes.

In this study, we applied five alternative process flows for the fabrication n-PERT solar cells with different complexities and compare the cell performances for each method.

5.3.1 Experimental Details

The solar cells and symmetrical samples for lifetime measurements were fabricated on Czochralski n-type Si solar wafers with base resistivity of 1.7±0.1 Ω.cm and thickness of 180 µm. Alkaline texturing/O_3 cleaning and chemical etching processes were performed by Rena Batchtex and Rena Inpilot systems, respectively. For the single side etching (SSE) process following the BBr_3 diffusion to remove the p^{++} region at the rear surface of the wafer, we used a chemical solution consisting of the mixture of $HF/HNO_3/H_2SO_4$/Deionized(DI) water, which was followed by KOH/DI water and HF/HCI/DI water. The surfaces of the samples were etched with the same recipe applied on the sample named E1 reported by Koçak Bütüner et.al in ODTÜ-GÜNAM [89]. High temperature P and B diffusion processes were conducted in atmospheric furnaces. The B diffused p^{++} on n-Si and P diffused n^{++} on textured p-Si were measured as 100 Ω/sq and 55 Ω/sq by the four-point probe, respectively. B implantation processes were performed at 7.5 keV and activated at 1050 °C while P was implanted at 10 keV and activated at 875 °C. The resulting sheet resistance of B implanted p^{++} was measured as 80 Ω/sq on n-Si and P implanted n^{++} was measured as 55 Ω/sq on textured p-Si. Deposition of Al_2O_3 was performed at 200 °C by spatial ALD tool and activated at 425 °C under N_2 flow. SiN_x with a refractive index of 1.96 at a wavelength of 632 nm and thickness of 75 nm was deposited as passivation and anti-reflective coating by the PECVD system. For the metallization, Ag/Al and Ag metal pasted were screen printed on the p^{++} and n^{++} sides, respectively and they were co-fired by a conveyor belt furnace. As a barrier layer to doping in some groups of samples, SiO_xN_y was deposited by the PECVD system and they were removed in HF solution after the process was completed. For the bifacial n-PERT solar cell fabrication, we applied five alternative process flows as shown in *Figure 5.14*. The complexity of manufacturing of the cells is getting more complex from left to right (from Group-A to Group-E). Besides the solar cells, we also fabricated symmetrical samples for iV_{oc} measurements. In this context, we compare B implantation and B diffusion processes on textured Si wafers which were passivated with (4nm) Al_2O_3/(75nm) SiN_x and subsequently exposed to a fast-firing process. For the comparison of P-implant and P-diffusion processes, the samples were prepared on chemically etched surfaces that were passivated with either SiN_x or (2nm) Al_2O_3/(75nm) SiN_x stack layers. The samples were finally exposed to fast firing processes as the symmetrical B samples.

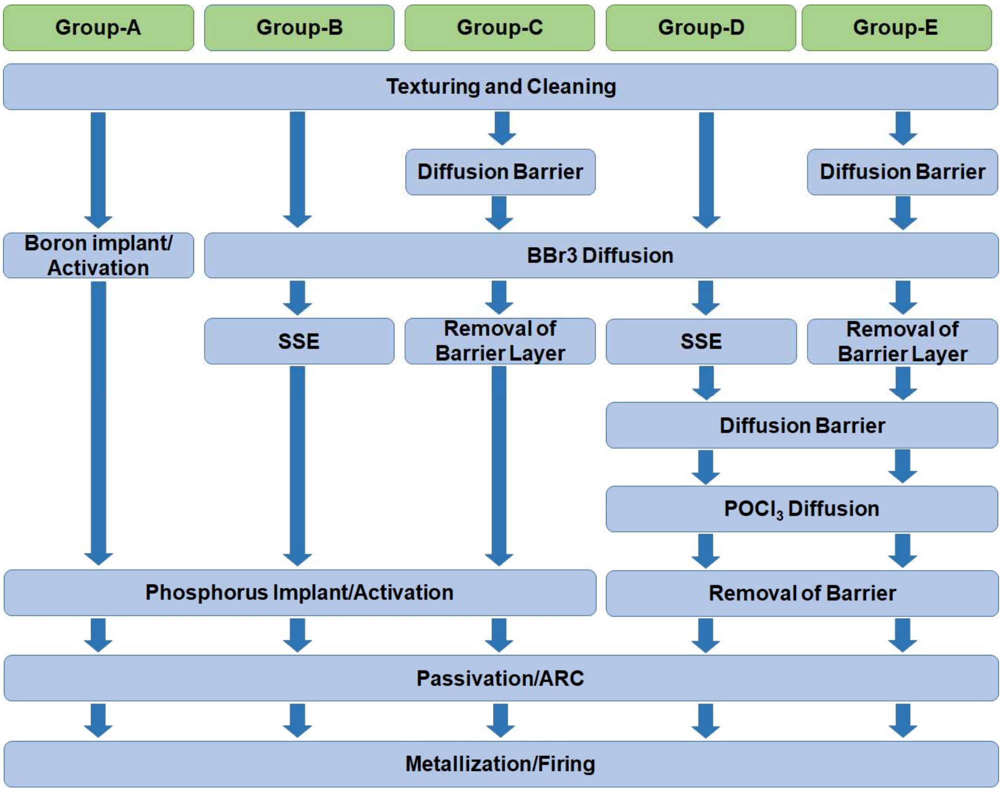

Figure 5.14 The alternative process flows for bifacial n-PERT solar cells

5.3.2 Results and Discussion

iV_{oc} values measured on symmetrical samples for B and P which were doped by either diffusion or implantation methods are given in *Figure 5.15*. B emitters formed by the diffusion method on textured n-Si wafers have higher iV_{oc} values than the ones by the ion implantation method. On the other hand, P doped BSF regions on the chemically etched surfaces have higher iV_{oc} values when formed by the ion implantation method rather than the diffusion method. Moreover, the passivation of n^{++} by Al_2O_3/SiN_x stack layer can yield a higher iV_{oc} compared to the only SiN_x layer especially when the n^{++} is formed by the diffusion method.

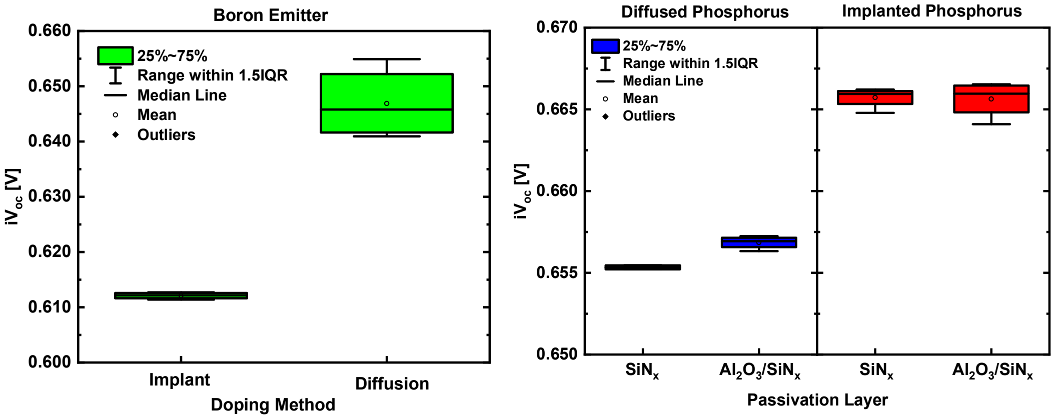

Figure 5.15 iV_{oc} values measured for B doped emitter on the textured surfaces (left) and P doped BSF on the etched surfaces (right) formed by either diffusion or implantation methods

The measured solar cell parameters such as V_{oc}, J_{sc}, FF and efficiency values obtained from I-V measurement for n-PERT solar cells from each group are given in *Figure 5.16*. For each group, various firing recipes were tested and the best result from each group are reported. The fully diffused PERT cells suffer from low FF which is mainly due to the requirement for edge isolation. It was observed that they improve significantly when their edges are isolated by a nanosecond laser. This necessitates fine edge protection during diffusion of dopants or an additional process for edge isolation. On the other hand, fully ion implanted solar cells suffer from low V_{oc} values which are due to poor emitter quality of B implanted n-Si as can be seen in *Figure 5.15*. The highest performance was obtained for the n-PERT solar cells with B diffused emitter and P implanted BSF in Group-B, showing an efficiency of 20.54% from the front side with a bifaciality factor of 0.89. When evaluated in terms of process complexity, it has a relatively lower workload compared to other process flows, except for group A in this study.

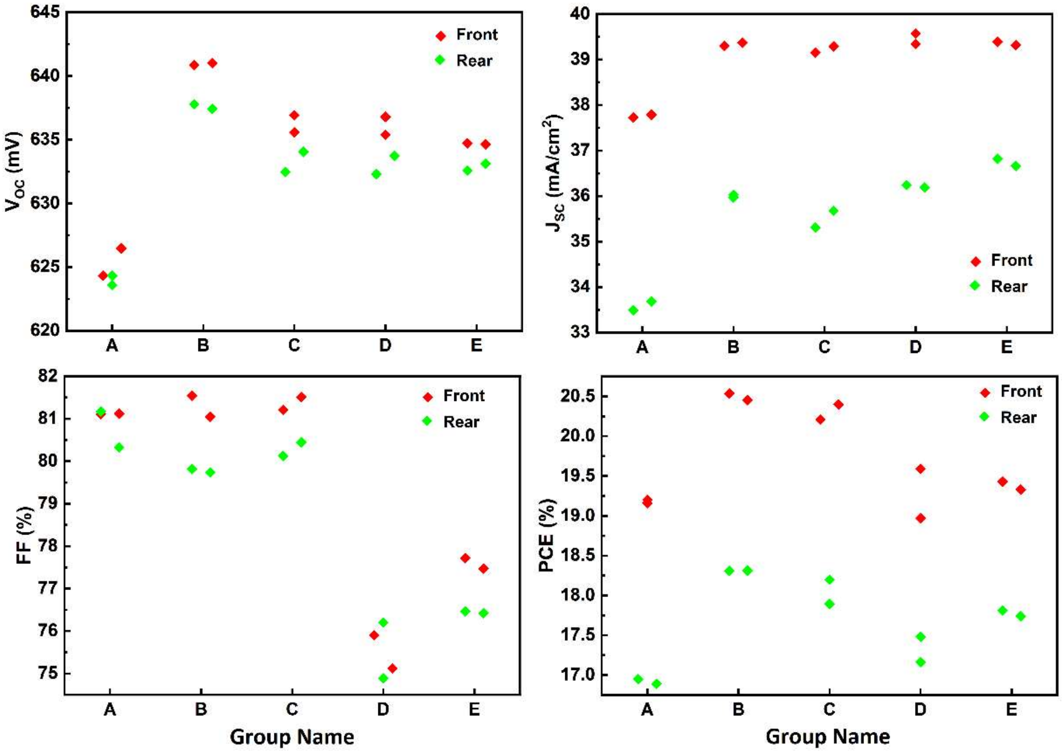

Figure 5.16 V_{oc}, J_{sc}, FF and efficiency values measured from the front and rear sides of the bifacial n-PERT solar cells in each group.

Figure 5.17 shows the reflectance graphs of the fabricated solar cells from the front and rear surfaces. Since the chemical etching process is not perfectly uniform throughout the wafer, the reflectance from the midpoint and a point close to the edge differs. It should be noted that the SiN_x layers at the front sides of the cells were slightly thicker than the ones at the textured rear surfaces, resulting in a higher reflectance at the wavelengths below 500 nm. The average weighted reflectance values of 10 different spots measured at the front sides of the cells with textured and chemically etched surfaces are 4.43% and 4.41%, respectively. On the other hand, they were calculated as 4.02% and 6.01% for the textured and etched rear surfaces, respectively.

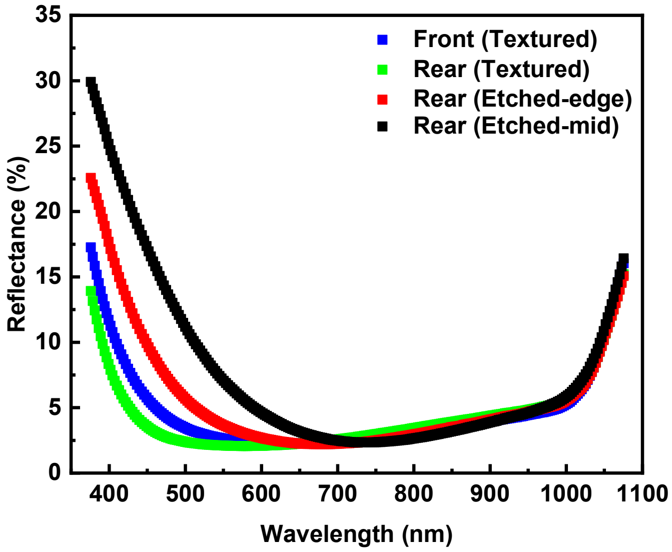

Figure 5.17 Reflectance graphs of the front and rear surfaces on the n-PERT solar cells

In conclusion, we presented five alternative process flows and compared the cell performance fabricated by various process flows. For the emitter and back surface field (BSF) formation, we utilized either diffusion or ion implantation methods. Our results showed that B diffused emitter compared to implanted one yields a significantly higher V_{oc} on the fabricated devices. The cells with diffused emitter and either diffused or implanted BSF have similar V_{oc} values for rear textured surfaces; however, the cells with single side etched rear surfaces and implanted BSF have approximately 5 mV higher V_{oc} compared to others. We obtained a higher performance on fabricated n-PERT solar cells with relatively lower process complexities, thus for the ones with B-diffused emitter and P-implanted BSF. The champion solar cell with a B-diffused emitter and a P-implanted BSF on a single side etched surface has a PCE of 20.54% from the front side with a bifaciality factor of 0.89.

5.4 Summary

In the first section, we studied the effect of implanted P profile on iV_{oc} variations during the firing process of n-type Si wafers. In this context, unimplanted and symmetrically P implanted textured n-Si wafers were annealed at 875 °C and 1050 °C resulting in two distinct doping profiles. The results indicate that the trend of iV_{oc} variation during the firing process depends on the annealing temperature of the samples, especially the implanted ones. P implanted samples activated at 875 °C lead to higher iV_{oc} values for any firing peak temperature; therefore, the separate activation of P with B at a lower annealing temperature is necessary during the fabrication of an n-type Si solar cell. Moreover, we showed that separate activation is beneficial to cell V_{oc}, which is consistent with the iV_{oc} measurements of the symmetrical samples, however, it is detrimental to FF due to poor contact of Ag with n^{++} on the fully implanted n-PERT solar cells. Furthermore, the contact resistivity can be significantly reduced with thin Al_2O_3 deposition in the interface of SiN_x:H and n^{++}. Furthermore, we investigated the performances of the fully ion-implanted bifacial n-PERT solar cells made of wafers from two different wafers suppliers named V1 and V2. The measured V_{oc} values of the cells and iV_{oc} values of the symmetrical emitter and BSF samples were almost equal for the wafers from the suppliers, which implies similar wafer qualities from the device perspective. Efficiencies of the fabricated solar cells slightly differ due to the variance in FF, which may be due to the difference in resistive losses of the cells. The highest efficiencies obtained at the front sides of the cells fabricated on the n-Si wafers from vendors V1 and V2 were 19.30% and 19.20%, respectively [90].

In the second section, we discussed the ECV and ToF-SIMS results to determine the active and inactive dopant ratio after the activation of implanted B atoms.

In the last section, we presented alternative industrially feasible methods for the fabrication of n-PERT solar cells. Also, we demonstrated the measured solar cell parameters of the devices fabricated with the proposed process flows. N-PERT solar cells with relatively fewer process complexities have significantly higher efficiencies. The best cell, which has a B-diffused emitter and P-implanted BSF on a single side etched surface has a PCE of 20.54% from the front side with a bifaciality factor of 0.89.

CHAPTER 6

INTERDIGITATED BACK CONTACT SOLAR CELLS

The first back contact (BC) solar cell paper, which was published by M.D. Lammert and R.J. Schwartz, in the literature, dates back to 1975 when the researchers were thinking of utilizing light concentrators to increase the solar efficiency since the cost per unit area of concentrators was cheaper than that of the solar cells. However, they realized that the efficiency of devices decreases significantly at high illumination intensities. Then, they proposed that the solar cell efficiency can be increased by reducing the internal series resistance caused by mainly thin front surface diffused layers. There are two ways of decreasing the internal series resistance:

- The number of metal grids can be increased by keeping them narrow and closely spaced; however, the incoming light will be reflected by the metals in this case.
- Both base and emitter polarities can be placed at the backside of the cell, which is named as back contact solar cell so that the metal design can be flexible regardless of optical loss [91][92].

Ever since the first back contact solar cell publication, different back contact designs have been studied. All these different types can be classified under three main categories as emitter wrap-through (EWT), metallization wrap-through (MWT) and back junction-back contact (BJ-BC) which is also named interdigitated back contact (IBC) solar cell.

In front contact solar cells, the emitter/front surface field (FSF), metal fingers and bus bars collecting electrons/holes are located near the front surface. The MWT back contact solar cells are very similar to the standard front contact cell design except for the bus bars connected to the fingers collecting the carriers at the front surface. In MWT, the bus bars are linked to the fingers from the backside of the cell while emitter/FSF and metal fingers are still placed on the front surface. In the case of EWT designs, there is no metal on the front surface of the cell but the emitter/FSF is still near the front surface. However, BJ-BC solar cell designs are void of any metals and emitters on the front side. In the scope of this thesis, BJ-BC solar cell, which is also called interdigitated back contact (IBC) solar cell, is investigated [93].

Advantages of Back Contact Solar Cells

- Higher short-circuit current (J_{SC}) of the cell can be obtained due to the absence of metal grids on the front side.
- Light trapping and surface passivation can be optimized better than the front contact solar cells since the low front contact resistance is not an issue as in front contact cells.
- Placing both contact polarities at the backside brings about a significant improvement in series resistance since the metal finger width is not limited by light shading.
- The ease of interconnection of the cells to assemble the module is also important. Back contact solar cells are very feasible in terms of module production since the cells can be placed next to each other without giving any space between the cells for wiring. This is also desired in terms of the total area efficiency of the module.

Challenges to Back Contact Solar Cells

- p^{++} and n^{++} doping patterns and opposing electrodes at the backside of the cell are very close and they can shunt if the masks are misaligned during the doping or metallization process.
- Minority carrier lifetime in back contact solar cells comes into question since they have to travel not only down the backside of the cell but also a lateral distance towards to emitter. Therefore, the quality of base silicon gains more importance.

- Process complexity is one of the major shortcomings of back contact solar cells due to the patterning steps at the backside.

In the following sections of this chapter, the experimental and simulation results of the fully ion-implanted n-type and p-type IBC solar cells are discussed. Within this context, we present simplified process flows for the IBC cell fabrication using a hard mask during the ion implantation process to form patterned p^+ and n^+ regions. Moreover, we compare IBC solar cells with and without FFE on p and n base wafers. Furthermore, we discuss the importance of bulk lifetime and front surface passivation on our simulation results.

6.1 Ion Implanted N-Type IBC Solar Cells With Front Floating Emitter

In IBC solar cell structure, lateral transport of photo-generated carriers is required since the BSF and emitter are periodically interdigitated at the rear surface of the device. Thus, the distance between two BSF regions is restricted by the diffusion length of the minority carrier. IBC solar cells with a front floating emitter (FFE), named "Mercury", are proposed to enhance the lateral transport of minority carriers. Thus, the Mercury cell concept enables flexibility for the design of the rear side with larger BSF width, which is desired to overcome alignment issues in cell fabrication. The FFE acts as a path where the minority carriers are injected when created above the BSF region. The minority carriers in the FFE are re-injected into bulk when they are above the emitter region and collected by the emitter. The total current flow to the emitter will be the addition of minorities injected from FFE to the emitter and the direct diffusion of minorities in the base to the emitter. Additionally, the pumping of minorities from bulk to FFE where they are the majority will help reduce carrier levels, thus lowering the recombination rate in the bulk [94].

Here, we investigate the FFE on n-type fully implanted IBC solar cells. Firstly, we show the behavior of the effective lifetime of unimplanted textured n-type Si at various thermal budgets. Secondly, the effective lifetime n-Si wafers with implanted

FFE regions are discussed. Finally, we present the results of the IBC solar cells fabricated with ion-implanted FFE in this study.

6.1.1 Experimental Details

The industrial n-type Cz-Si solar wafers with base resistivity between 2.1-2.3 Ω.cm were textured with an alkaline solution to reduce the reflectivity and their surfaces were exposed to an ozone-based (O_3) surface cleaning process.

For the investigation of the annealing temperature on n-Si wafers without implantation processes, the samples were exposed to annealing processes at 875 °C or 1050 °C under N_2 flow for 30 minutes. One group of samples was also separated as a reference without annealing treatment. Then, the samples were dipped into HF solution and rinsed in deionized (DI) water. The surfaces of the samples were passivated with 2 nm of Al_2O_3 by a spatial atomic layer deposition (ALD) tool. Al_2O_3 layers were activated at 425 °C under N_2 ambient in an atmospheric furnace.

For the comparison of the sample with and without FFE on n-Si wafers passivated with two different dielectrics, two groups of samples were prepared. One group of wafers was double-side doped with B by the ion implantation method and they were annealed at 1050 °C. The sheet resistance and active doping profile of the FFE region on textured n-Si were measured by the four-point probe and electrochemical capacitance-voltage methods, respectively. The second group of textured wafers was not implanted. Later, each group of samples was passivated with either SiN_x/SiO_xN_y or $Al_2O_3/SiN_x/SiO_xN_y$ stack layers. SiN_x/SiO_xN_y stack, named H4 and extensively described in Table 4.4, was deposited by the PECVD system. Al_2O_3 layers were deposited with the thickness of 4 nm and were activated at 425 °C under N_2 ambient in an atmospheric furnace. Finally, the samples were fired by a conveyor belt furnace to mimic the cell process.

For the fabrication of the IBC solar cells with and without FFE, the activation of the dopants was separately performed at 1050 °C and 875 °C for B and P, respectively.

The process parameters and the ECV profiles of the emitter and BSF regions were given in Chapter 5.1. The passivation layers were deposited following a HF dipping and rinsing process. The front side of the cells with FFE was passivated with Al_2O_3/H4. The Al_2O_3 layer was deposited with a thickness of 4 nm by the ALD method. On the other hand, the front side of the IBC cells without FFE was deposited with only H4 by the PECVD tool. The rear surface of each cell was identically passivated with an Al_2O_3/H4 stack in which the thickness of Al_2O_3 was 2 nm. For the metallization process, after Ag/Al and Ag metal pastes were screen printed on the p^{++} and n^{++} regions, respectively, a fast firing process was applied for the fire through of the metals through the dielectric layers by a conveyor belt furnace. The process flows for the fabrication along with the schematic representation of fully ion implanted n-IBC solar cells with and without FFE are shown in *Figure 6.1*. The active area of the cells were approximately 12 cm^2 with slight variation depending on the design.

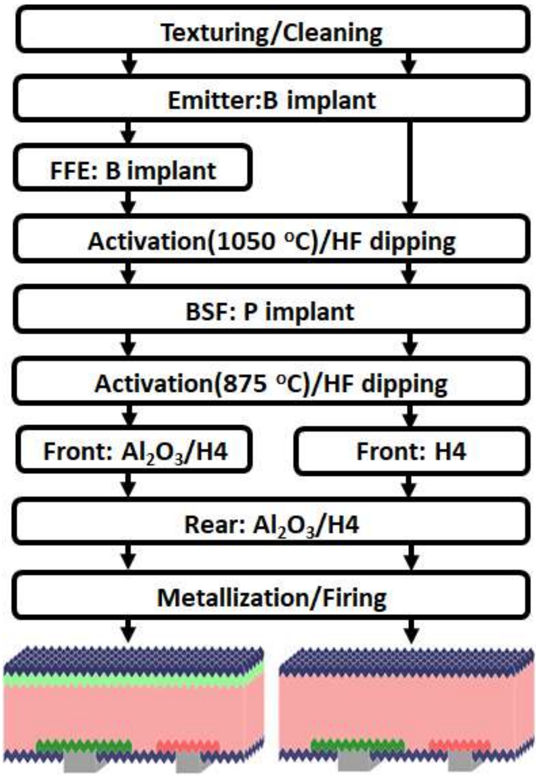

Figure 6.1 Process flows and schematics of fully ion implanted n-IBC solar cell with FFE (left) and without FFE (right). H4 is described in

The emitter, BSF and gap defined at the rear side of the IBC solar cell is shown in *Figure 6.2*.

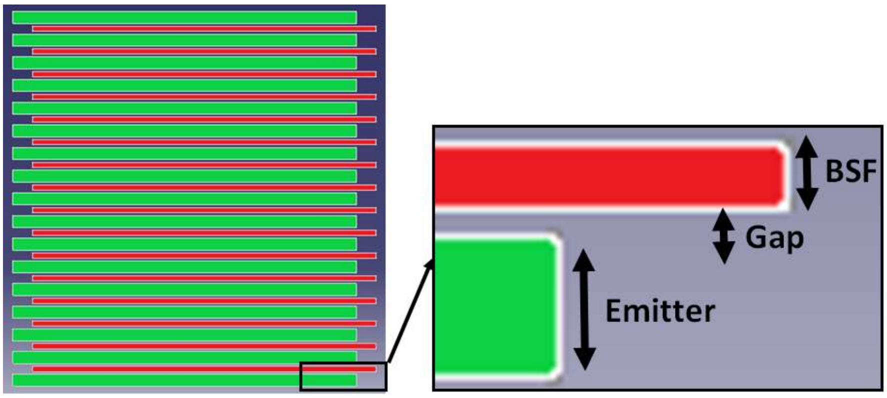

Figure 6.2 Emitter, BSF and gap defined for the IBC solar cell

Measurement Methods:

The front and rear sides of the fabricated solar cells were characterized with SunsVoc and IV measurements. In the SunsVoc measurement, the IBC solar cells were placed on a PCB as shown in *Figure 6.3* since two of the busbars are at the rear surface.

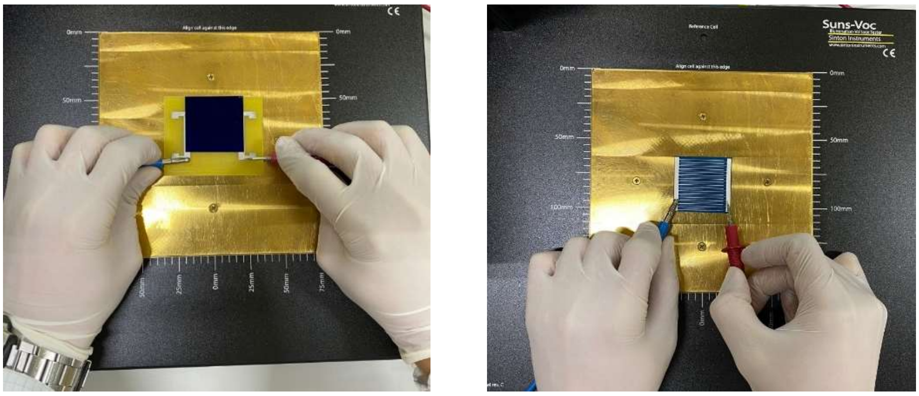

Figure 6.3 SunsVoc measurement from the front (left) and rear side (right) of the IBC solar cell

The I-V measurements of the solar cells were conducted on the front and rear sides. For the front side measurement, a special chuck designed for IBC solar cells was used.

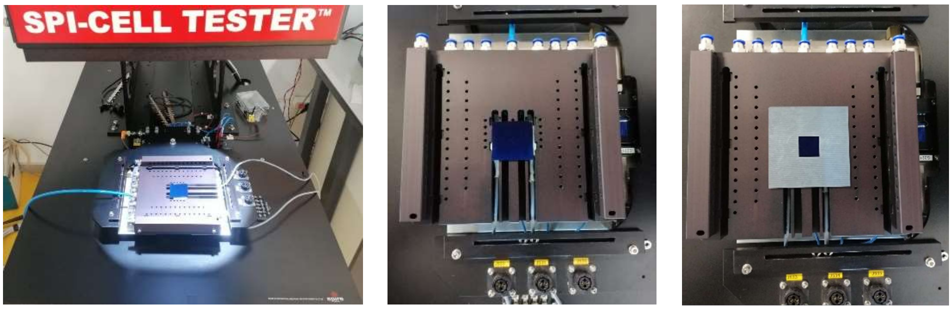

Figure 6.4 I-V measurement setup for IBC solar cells

6.1.1 Results and Discussion

Figure 6.5 illustrates the influence of annealing temperatures on the effective lifetime of textured n-Si wafers, which were passivated by 2 nm Al_2O_3 deposited by the ALD tool. The samples annealed at 875 °C have almost two times higher effective lifetime than unannealed ones. Here it should be noted that the unannealed sample was exposed to heat treatment during the activation of Al_2O_3 at 425 °C. The increase of τ_{eff} can be attributed to the annihilation of metastable defects [85]. Annealing at 1050 °C, on the other hand, leads to a reduction in the effective lifetime, most likely due to the formation of oxygen precipitation in the bulk [85]. Nevertheless, the values are still reasonable for the fabrication of IBC solar cells with high efficiency. The highest effective lifetime was measured above 6 ms for the n-Si wafer annealed at 875 °C and passivated with Al_2O_3.

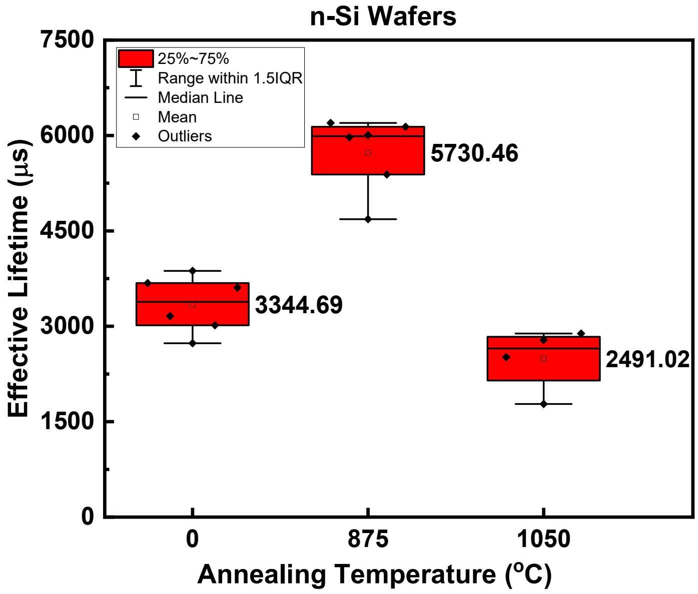

Figure 6.5 Effective lifetime on n-Si wafers annealed at either 875 °C or 1050 °C along with a unannealed reference.

In *Figure 6.6*, ECV profiles of FFE with a sheet resistance of around 230 Ω.sq is given. The active dopant dose calculated by numerical integration of the ECV profile from the surface to junction is 3.96E14 cm^{-2}.

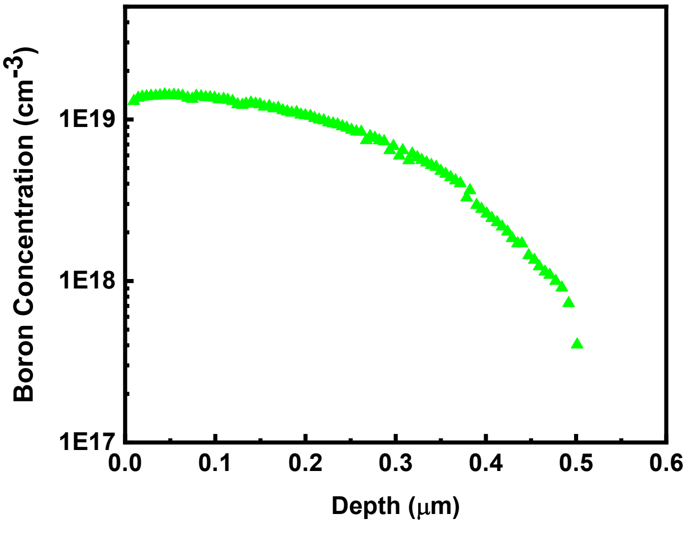

Figure 6.6 ECV profile of FFE formed by B implantation at 5 keV and subsequent annealing at 1050 °C for 30 minutes under N2 ambient.

In *Figure 6.7*, we compare the effective lifetime of the textured n-Si wafers with and without FFE, which were passivated with either Al_2O_3/H4 or H4 stack layers and subsequently exposed to a fast firing process. From the graphs, it can be deduced that the implanted FFE in n-Si wafers significantly reduces the effective lifetime. When we compare the passivation layers on FFE samples, Al_2O_3/H4 to a lower effective lifetime compared to H4 stack layer. On the other hand, it is vice versa for the samples without FFE. The highest effective lifetime was obtained as 728.2 µs on average for n-Si wafers having no FFE and passivated with H4 passivation stack.

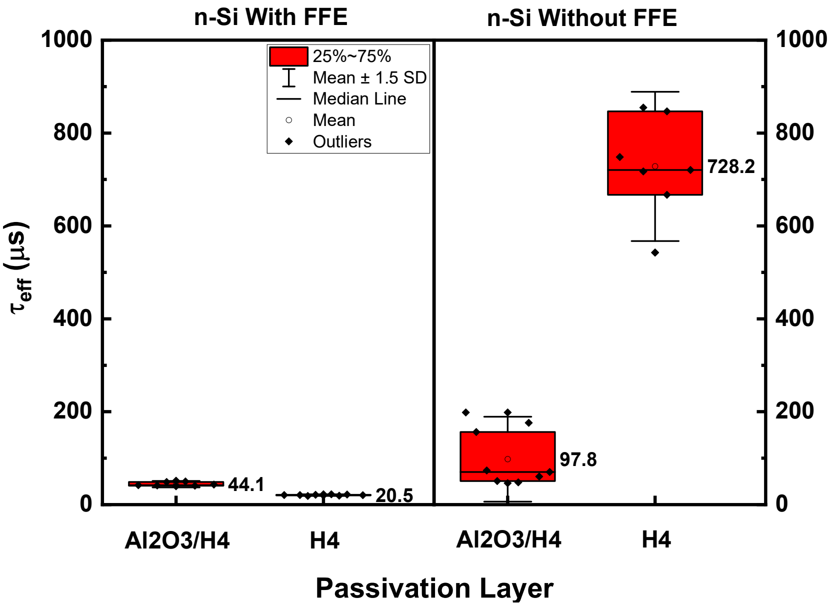

Figure 6.7 Effective lifetime values of n-Si wafers with and without boron implanted FFE, which were passivated with either Al_2O_3/H4 or H4 stack layers.

V_{oc} and pseudo (pFF) values measured by SunVoc at the front surface of n-IBC solar cells with and without FFE are given in Table 6.1. The samples without FFE have significantly higher V_{oc} than the ones with FFE. This is consistent with the effective lifetime results on symmetrical samples which are shown in *Figure 6.7*. Similar values of V_{oc} for the various metal fraction can be attributed to the fact that the values of $J_{o,emitters}$ are as high as $J_{o,metal}$.

Table 6.1 *Effect of FFE on Voc and pFF measured by SunsVoc*

Front Surface	*Metal Fraction (%)*	V_{oc} by SunsVoc (mV)	*pFF* (%)
No FFE	20	632.60	81.80
	30	634.52	82.03
	40	633.79	82.08
With FFE	20	613.30	81.51
	30	614.12	81.22
	40	Not available	

Figure 6.8 illustrates the I-V curves of n-IBC solar cells with FFE and without FFE at the front surface. V_{oc} values measured by continuous simulator are in the same trend with the SunsVoc measurement. However, for IBC solar cells, the temperature rises under continuous light exposure, since the I-V measuring chuck cannot be metal to avoid shunting opposite polarities during measurement. This results in lower V_{oc} values in the case of measurement under continuous light. Relatively lower J_{sc} values for the samples with FFE can be also explained by the poor passivation. The reason for the low FF is mainly due to R_{series} and peripheral effect since the pFF value, which excludes the R_{series} of the solar cell, was measured above 80% by the SunsVoc method. The effect of edges was also confirmed by shadowing the edges of the devices. When the edges of the solar cells were covered with a hard mask during the I-V measurement, then FF values increase to 70.0% and 73.5% for samples without FFE and with FFE, respectively. In this case, the corresponding efficiencies for the one without and with FFE are calculated as 17.28% and 14.46%, respectively.

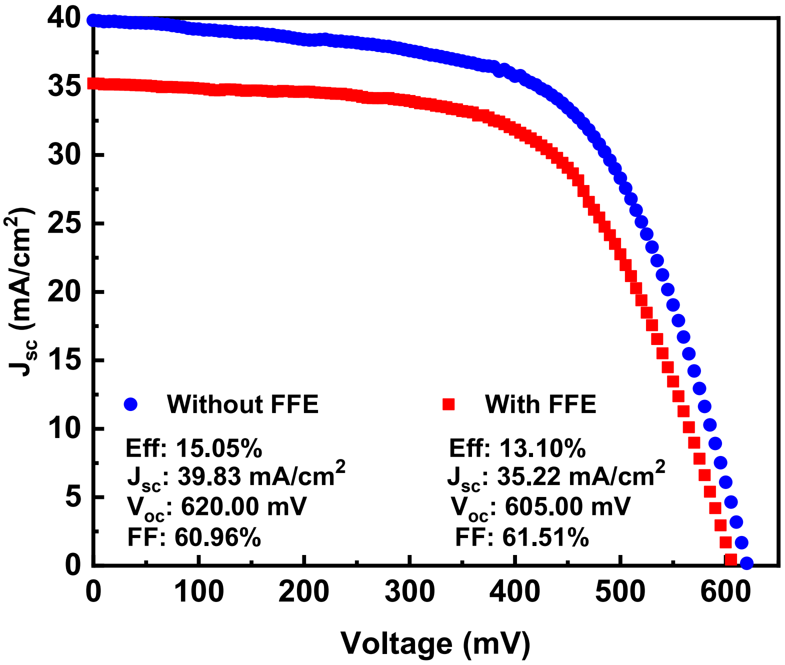

Figure 6.8 I-V curves of n-IBC solar cells with FFE (red) and without FFE (blue)

Quokka Simulation of n-IBC Solar Cells

We also performed a device simulation by Quokka 2 program to investigate the effect of τ_{bulk} and $J_{o,front}$ values on the performance of an IBC solar cell. The simulation was based on the measured values on our samples, except $J_{o,metal}$. The parameters applied in this study are given in Table 6.2.

Table 6.2 *The parameters used in Quokka 2 simulations*

Quokka2 Parameters		**Value**
Main	Cell Thickness	180 µm
	Width	1150 µm
Front Surface	Boundary type	variable
	Sheet resistance	600 Ω/sq (for conductive boundary)
	Doping type	p-type (for conductive boundary)
	$J_{o,front}$	variable
Bulk	Doping type	n-type
	Resistivity	2 Ω.cm
	Bulk lifetime	variable
Rear (Emitter)	Emitter width	1200 µm
	$J_{o,emitter}$	780 fA/cm^2
	$J_{o,emitter\ metal}$	780 fA/cm^2
	Contact resistivity	4E-03 Ω cm^2
	Contact Opening	240 µm
Rear (BSF)	BSF width	500 µm
	$J_{o,bsf}$	271 fA/cm^2
	$J_{o,bsf\ metal}$	600 fA/cm^2 [95]
	Contact resistivity	1E-13 Ω.cm^2
	Contact Opening	100 µm
Rear (Gap)	Gap width	300 µm
	$J_{o,gap}$	10 fA/cm^2

Figure 6.9 shows the dependence of V_{oc}, J_{sc}, FF and efficiency values of the n-IBC with FFE on the τ_{bulk} and $J_{o,front}$ values. The stars with red color on the graphs are the results that can be obtained from our solar cells with the measured τ_{bulk} and $J_{o,front}$ on our symmetrical samples. According to simulation results, our n-IBC solar cells with FFE can exceed 21% if the τ_{bulk} and $J_{o,front}$ values are improved on the current design and parameters.

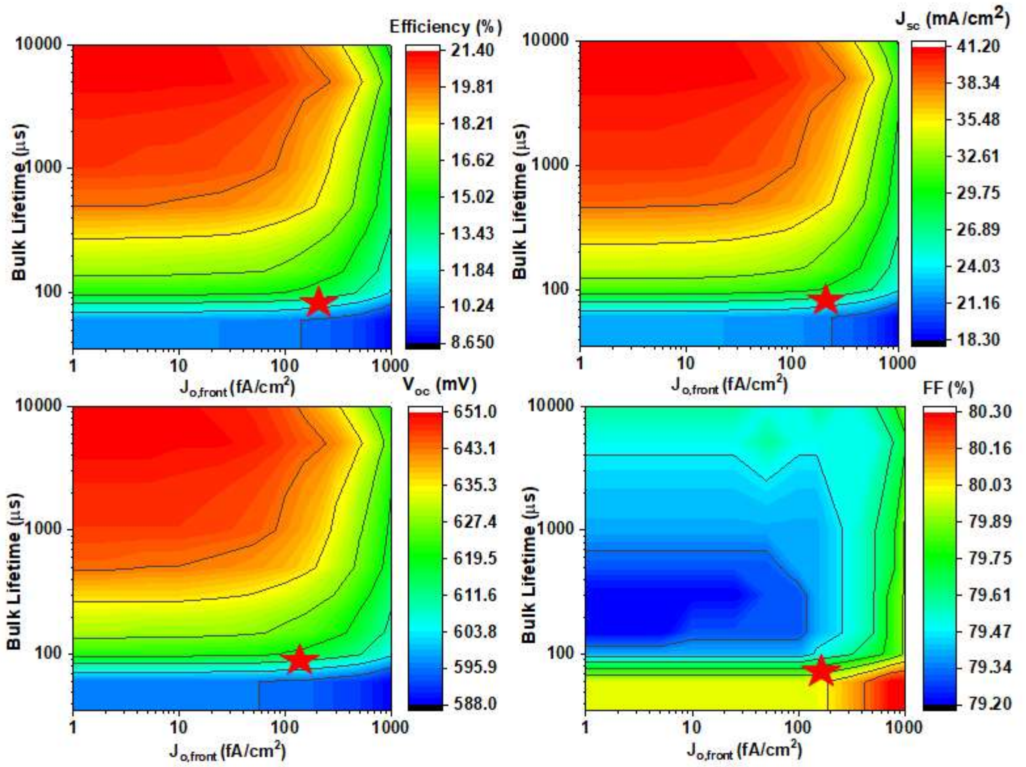

Figure 6.9 Simulation results showing the effect of τ_{bulk} and $J_{o,front}$ on the solar cell parameters of n-IBC with FFE. The stars with red color represent measured τ_{bulk} and $J_{o,front}$ on our samples.

Similarly, it is possible to obtain an efficiency of 21% if the τ_{bulk} and $J_{o,front}$ values are improved for the solar cells without FFE as shown in *Figure 6.10*. The stars with yellow color on the graphs are the results that can be obtained from our solar cells with the measured τ_{bulk} and $J_{o,front}$ on our symmetrical samples. The simulation results show a similar trend to the fabricated ones except for the FF values since the peripheral effect is ignored in the simulation. Also, series resistance and shunt resistance values are not defined based on the fabricated cells.

Furthermore, if we compare the simulation results, the sensitivity of V_{oc}, J_{sc}, and efficiency values to variation of τ_{bulk} and $J_{o,front}$ is very significant for the cells without FFE.

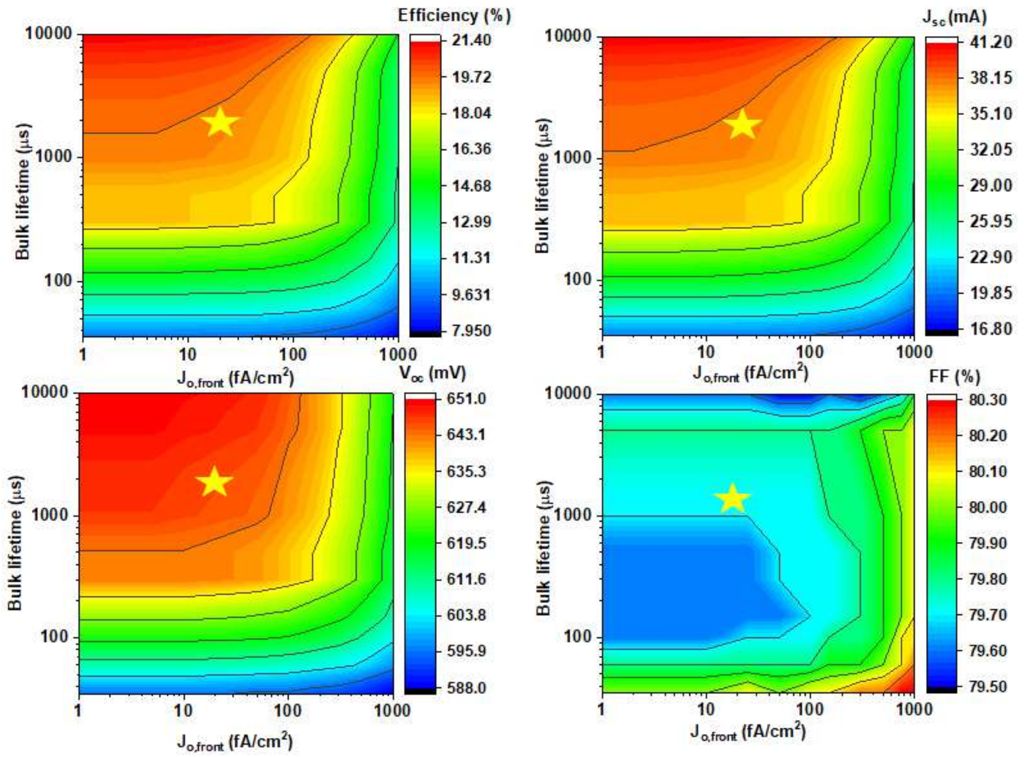

Figure 6.10 Simulation results showing the effect of τ_{bulk} and $J_{o,front}$ on the solar cell parameters of n-IBC without FFE. The yellow with red color represent measured τ_{bulk} and $J_{o,front}$ on our samples.

6.2 Ion Implanted P-Type IBC Solar Cells With/Without FFE

Boron (B) atoms are activated above 1050 °C while phosphorus (P) can be activated at around 875 °C. Thus, a p-type IBC solar cell with a P emitter and Al BSF is an alternative structure fabricated with a lower thermal budget. In this scope, we investigate the p-type IBC solar cells with various cell designs in terms of rear geometry and front surface doping named FFE. Firstly, we compare the effective lifetime of textured p-type Si with and without FFE passivated with either SiO_xN_y or Al_2O_3/SiO_xN_y dielectric layers. Secondly, we present the I-V results of the p-IBC solar cells with two different designs on the rear side.

6.2.1 Experimenal Details

The industrial p-type Cz-Si solar wafers with base resistivity between 1.1-1.2 Ω.cm were alkaline textured and cleaned with ozone (O_3)-based solution.

For the comparison of symmetrical samples with FFE and without FFE, we fabricated two groups of samples on textured p-Si wafers with and without FFE, which were passivated with either $Al_2O_3/SiN_x/SiO_xN_y$ or SiN_x/SiO_xN_y stack layers. The Al_2O_3 layer with a thickness of 5 nm was deposited by a spatial ALD tool; SiN_x/SiO_xN_y stack, named H4 in Table 4.4, was deposited by the PECVD system. For the formation of FFE, the samples were double side P implanted and subsequently activated at 875 °C under N_2 ambient in an atmospheric furnace. The samples were always dipped into HF solution and rinsed before the deposition of passivation layers. The sheet resistance and active doping profile of the FFE region were measured by the four-point probe and electrochemical capacitance-voltage methods, respectively.

For the fabrication of the IBC, P atoms were implanted through a hard mask in the emitter region. The P atoms were activated at 875 °C under N_2 ambient in an atmospheric furnace. The process parameters and ECV profile of the emitters were given with the name D2 in Chapter 4.3. Later, the front and rear surfaces of the samples were deposited with a dielectric stack named H4 for anti-reflectivity and passivation. For the laser contact opening between the emitters, a picosecond laser was used to ablate the dielectric layer with a width of 60 µm. For the metallization process, Al and Ag metal pastes were screen printed on the laser ablated region and n^{++} regions, respectively. Finally, the solar cells were exposed to a fast firing process by a conveyor belt furnace. The process flow and the schematic of a p-IBC solar cell with FFE are shown in *Figure 6.11*.

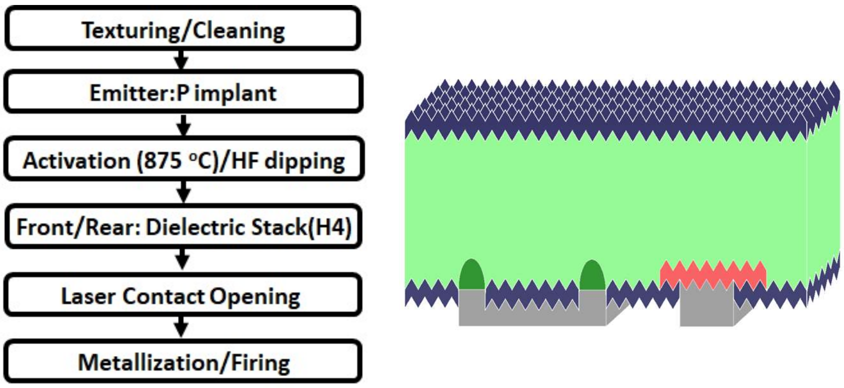

Figure 6.11 Process flow (left) and schematic (right) of a fully ion implanted p-IBC solar cell without FFE.

The width for the emitter, BSF and gap for two different designs of the fabricated IBC solar cells are given in Table 6.3.

Table 6.3 *The emitter, BSF and gap width for the IBC solar cell designs in this stud*

Design Name	Emitter Width (mm)	BSF LCO (mm)	Gap Width (mm)
1	1.20	0.50	0.30
2	1.80	0.90	0.28

6.2.2 Result and Discussion

In *Figure 6.6*, the ECV profile of FFE with a sheet resistance of around 740 Ω.sq measured on p-Si wafers is given. The active dopant dose calculated by numerical integration of the ECV profile from the surface to junction is 3.7E13 cm^{-2}.

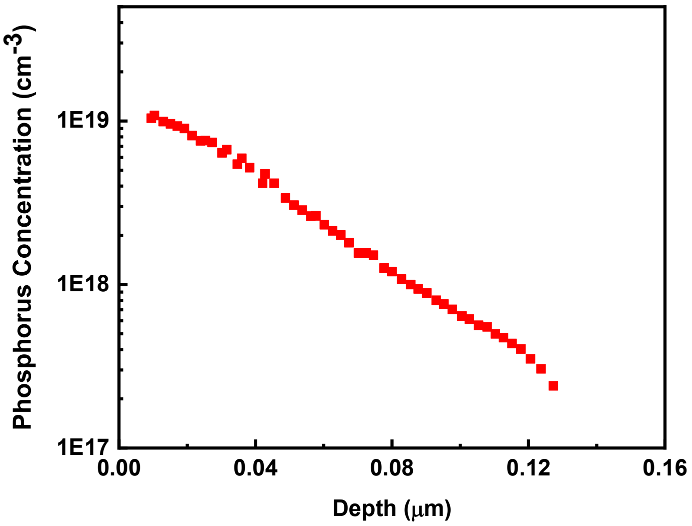

Figure 6.12 ECV profile of FFE formed by P implantation at 10 keV and subsequent annealing at 875 °C for 30 minutes under N2 ambient.

In *Figure 6.13* we compare the effective lifetime of the textured p-Si wafers with and without FFE, which were passivated with either Al_2O_3/H4 stack or H4 stack and subsequently exposed to a fast firing process. From the graphs, it can be seen that the implanted FFE in p-Si wafers significantly reduces the effective lifetime. Our results suggest that Al_2O_3/H4 leads to a lower effective lifetime compared to H4 stack layer on the textured p-Si with and without FFE. The maximum effective lifetime was obtained as 129.3 μs on average for the samples on p-Si without FFE passivated with H4 passivation stack.

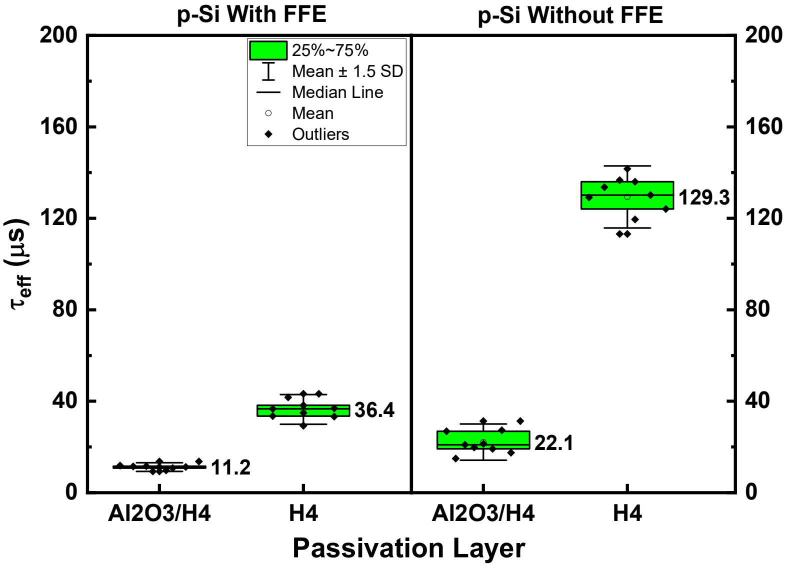

Figure 6.13 Effective lifetime values of p-Si wafers with and without P implanted FFE, which were passivated with either Al_2O_3/H4 or H4 stacks.

Based on the lifetime results of the textured p-Si samples representing the front of the device, the fabricated solar cells were passivated with H4 stack. *Figure 6.14* shows the V_{oc} values measured from the front and rear sides by the SunsVoc method on the fabricated p-IBC solar cells with two different rear designs. The V_{oc} trend is in decrease with increasing metal fraction from both front and rear side measurements. The decrease in V_{oc} with increasing metal fraction can be attributed to the decrease in photo-generated carrier when measured from the rear side. On the other hand, the variation for the front side measurement may be due to the different I_0 values of metal for different metal fraction. Compared to the non-metallized regions, metal interface is more likely to be recombinative, resulting in a decrease in V_{oc}. On the other hand, other effects such as misalignment may also play a role in V_{oc} variation since the sample with a metal fraction of 30% has a higher V_{oc} compared to the one with a metal fraction of 20% in group Desing-2.

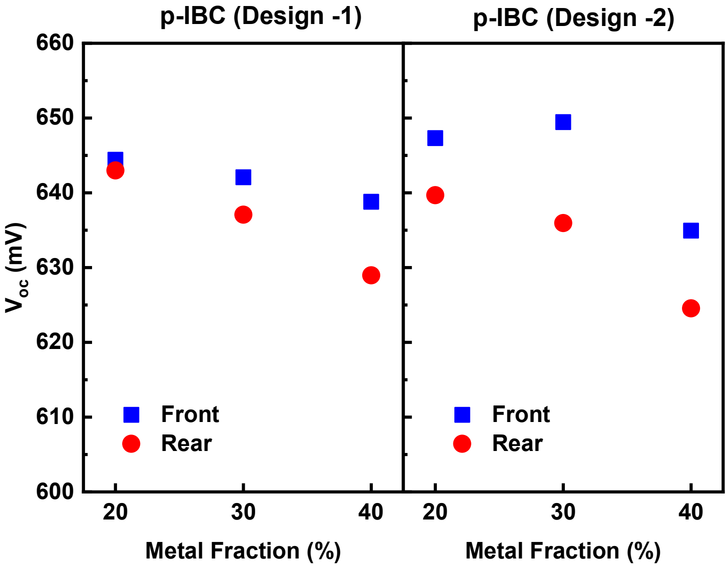

Figure 6.14 V_{oc} values measured from the front (blue) and rear (red) sides by the SunsVoc method on the fabricated p-IBC solar cells with Design 1 (left) and Design-2 (right)

In Table 6.4, the I-V measurement results of the solar cell with a metal fraction of 30% in Desing-1, which were measured from the front and rear sides by the solar simulator, are given. The highest efficiency was measured as 15.60% from the front side of the cell with bifaciality factor of 0.81.

Table 6.4 *I-V measurement results of p-IBC solar cells with and without FFE*

Sample Name	*Measured Side*	V_{oc} (mV)	J_{sc} *(mA/cm²)*	*FF (%)*	*Eff. (%)*	*Bifaciality factor*
p-IBC	Front	645	39.43	61.36	**15.60**	0.81
	Rear	630	31.73	63.52	12.70	

6.3 Summary

In this chapter, we presented the applicability of the ion implantation method for simplification of IBC solar cell manufacturing by patterned doping through a hard mask. In the first section, ion implanted n-type IBC solar cells with Mercury design were discussed. We showed that the effective lifetime of unimplanted n-Si wafers increases when annealed at 875 ºC but starts to degrade when annealed at 1050 ºC. We also demonstrated that the boron implanted FFE results in a significant reduction in the lifetime of n-Si. Our results suggest that the n-type IBC solar cell without FFE region passivated with H4 stack has the highest effective lifetime. The maximum efficiency was obtained as 13.76% with a bifaciality factor of 1.08. We also discussed our Quokka2 simulation results based on parameters we measured from our samples. The trend of experimental data for the cells with and without FFE was consistent with our simulation results, except for FF which is strongly affected by the edges during the IV measurement.

In the second section, we presented the results of p-type IBC solar cells with and without FFE. The process flow for the fabrication of p-type IBC solar cells was simplified as ion implanted PERC solar cells with a relatively lower thermal budget since we replaces B implant with Al-Si alloy. We measured a PCE of 15.60% at the front side of the champion solar cell.

CHAPTER 7

CONCLUSIONS AND OUTLOOK

This thesis aimed to demonstrate the applicability of the ion implantation doping method to the fabrication of homojunction crystalline silicon solar cells to reduce the process complexities thanks to its patterned doping with a hard mask and single-side doping capabilities. Besides the alternative process simplifications for PERC, PERT, and IBC solar cells, their performance improvement was also discussed. The most distinguishing outcomes of each solar cells type studied in this work can be explained as follows:

In the chapter reserved for ion-implanted PERC solar cells, the simplified process flow for the fabrication of the device having Al_2O_3/SiN_x stack passivation at the rear surface was presented. The maximum power conversion efficiency was measured as 20.0% on PERC cells with the size of M2. Although P implantation has been already applied to PERC solar cells in the literature, the single side doping advantage of this method was not benefited since extra process steps have been included due to the concerns about the passivation of the front and rear surfaces. Moreover, the textured rear surface of PERC solar cell as a product of simplified process flow can also pave the way for the improvement in light trapping when applied for bifacial design, especially at high albedo. In addition, the dielectric layers (the ARC layer at the front surface and the capping layer on the Al_2O_3 passivated etched rear surface) were also optimized for further improvement of ion implanted PERC solar cells. The maximum efficiency in this section was 20.3% for the champion cell.

In the chapter on PERT solar cells, B and P implantation were studied together on the same process batch due to the requirement of p^{++} and n^{++} regions on the same wafer. While P atoms are activated at around 875 ^{o}C, B atoms are activated at a higher thermal around 1050 ^{o}C. Our results suggested that the separate activation of

P at the low thermal budget resulted in higher iV_{oc} and V_{oc} values on the symmetrical samples and solar cells, respectively. Moreover, we proposed alternative process flows with the various workloads for the fabrication of n-PERT solar cells by utilizing the ion implantation and diffusion methods. The highest PCE was measured as 20.5% on the device having relatively simple process flow with B diffusion and P implantation for formation of emitter and BSF, respectively.

In the chapter on IBC solar cells, we demonstrated how to simplify a very complex fabrication process flow by using a hard mask to form the doping pattern during the ion implantation method. FFE in IBC solar cells enhances the lateral transport of the minority carriers so that the BSF regions can be wider, which brings about flexibility in the processing of the doping and metallization. We showed that FFE formed by the ion implantation method resulted in a decrease in the performance of both n-type and p-type IBC solar cells compared to the ones without FFE. We also presented a p-IBC solar cells fabricated by flowing the same process flow with ion implanted PERC cells. The emitter was formed by P implantation and the BSF was formed in the laser ablated region by Al/Si alloy during the fast firing process. The highest efficiency of p-IBC solar cells was 15.6%. We also briefly discussed our Quokka2 simulation results based on parameters we measured from our samples.

According to the results of this thesis, several studies to be done in the future are as the following:

Bifacial PERC solar cells with etched rear surfaces are already available in the industry. The ion-implanted PERC solar cells with a simple process flow can have the advantage of a textured rear surface in terms of light trapping, especially for high albedo. The solar cell design and process optimization in this thesis will be applied to the bifacial PERC solar cells.

N-PERT solar cells with various fabrication methods were presented in the scope of this thesis. The results showed that the B implantation for emitter formation in n-Si wafers should be studied further to have lower $J_{o,emitter}$ values. Alternatively, BF2 implantation will be also investigated since it can be activated at a lower thermal budget and have the potential for low J_o values.

For the IBC solar cells, $J_{o,front}$ will be reduced with further optimization of doping and passivation processes to increase the efficiency of the device with FFE since our simulation results showed that IBC cells are less sensitive to bulk lifetime and J_o values when they have FFE emitters. Also, we showed that the effect of edges is very significant in IBC solar cells. All the optimized parameters on small area IBC solar cells will be applied to fabricate large area devices.

REFERENCES

[1] N. Kannan and D. Vakeesan, “Solar energy for future world: - A review,” *Renew. Sustain. Energy Rev.*, vol. 62, pp. 1092–1105, 2016, doi: 10.1016/j.rser.2016.05.022.

[2] M. Green *et al.*, “Solar cell efficiency tables (version 40),” *Ieee Trans Fuzzy Syst*, vol. 20, no. 6, pp. 1114–1129, 2012, doi: 10.1002/pip.

[3] E. C. Douglas and R. V. D’Aiello, “A Study of the Factors which Control the Efficiency of Ion-Implanted Silicon Solar Cells,” *IEEE Trans. Electron Devices*, vol. 27, no. 4, pp. 792–802, 1980, doi: 10.1109/T-ED.1980.19938.

[4] C. E. Dubé *et al.*, “High efficiency selective emitter cells using patterned ion implantation,” *Energy Procedia*, vol. 8, pp. 706–711, 2011, doi: 10.1016/j.egypro.2011.06.205.

[5] T. Dullweber, R. Hesse, V. Bhosle, and C. Dubé, “Ion-implanted PERC solar cells with Al2O3/SiN x rear passivation,” *Energy Procedia*, vol. 38, pp. 430–435, 2013, doi: 10.1016/j.egypro.2013.07.300.

[6] A. Lanterne *et al.*, “High efficiency fully implanted and co-annealed bifacial n-type solar cells,” *Energy Procedia*, vol. 38, pp. 283–288, 2013, doi: 10.1016/j.egypro.2013.07.279.

[7] R. Müller, C. Reichel, J. Benick, and M. Hermle, “Ion implantation for all-alumina IBC solar cells with floating emitter,” *Energy Procedia*, vol. 55, pp. 265–271, 2014, doi: 10.1016/j.egypro.2014.08.078.

[8] Y. Huang *et al.*, “Solar Energy Materials and Solar Cells Fully screen-printed bifacial large area 22 . 6 % N-type Si solar cell with lightly doped ion-implanted boron emitter and tunnel oxide passivated rear contact,” *Sol. Energy Mater. Sol. Cells*, vol. 214, no. December 2019, p. 110585, 2020, doi: 10.1016/j.solmat.2020.110585.

[9] J. D. Plummer, M. D. Deal, and P. B. Griffin, *Silicon VLSI Technology: Fundamentals, Practice and Modeling*. Pearson, 2000.

[10] R. Müller, “Ion Implantation for High-Efficiency Silicon Solar Cells,” Fraunhofer, 2016.

[11] A. H. M. Smets, K. Jäger, O. Isabella, R. A. van Swaaij, and M. Zeman, “Solar Cell Parameters and Equivalent Circuit,” *Sol. energy Phys. Eng. Photovolt. conversion, Technol. Syst.*, pp. 113–121, 2016, [Online]. Available: https://ocw.tudelft.nl/wp-content/uploads/solar_energy_section_9_1_9_3.pdf.

[12] J. Ziegler, J. P. Biersack, and U. Littmark, *The Stopping Range of Ions in Solids*. New York: Pergamon Press, 1985.

[13] S. Decoster, A. Vantomme, and U. Wahl, “Ion implantation in Ge : Structural and electrical investigation of the induced lattice damage study of the lattice location of implanted impurities .,” 2009.

[14] J. Slotte *et al.*, “Fluence, flux, and implantation temperature dependence of ion-implantation-induced defect production in 4H-SiC,” *J. Appl. Phys.*, vol. 97, no. 3, 2005, doi: 10.1063/1.1844618.

[15] J. Li and K. S. Jones, “311 defects in silicon: The source of the loops,” *Appl. Phys. Lett.*, vol. 73, no. 25, pp. 3748–3750, 1998, doi: 10.1063/1.122882.

[16] F. Cristiano, “Ion Implantation-Induced extended defects : structural investigations and impact on Ultra-Shallow Junction properties,” Université Paul Sabatier Toulouse III, 2013.

[17] J. Kim, J. W. Wilkins, and F. S. Khan, “Extended Si |P[311|P] defects,” *Phys. Rev. B - Condens. Matter Mater. Phys.*, vol. 55, no. 24, pp. 16186–16197, 1997, doi: 10.1103/PhysRevB.55.16186.

[18] D. D. McNamara, “How do eclogites deform in subduction and collision zones? An Alpine study,” University of Liverpool, 2009.

[19] G. Arora and D. S. Aidhy, “Machine learning enabled prediction of stacking fault energies in concentrated alloys,” *Metals (Basel).*, vol. 10, no. 8, pp. 1–17, 2020, doi: 10.3390/met10081072.

[20] J. W. J. Morris, “Chapter 4 : Defects in Crystals,” *Mater. Sci. Eng. An Introd.*, pp. 76–107, 2013, [Online]. Available: http://www.mse.berkeley.edu/groups/morris/MSE205/Extras/defects.pdf.

[21] F. E. Rougieux, N. E. Grant, and D. Macdonald, “Thermal deactivation of lifetime- limiting grown-in point defects in n-type Czochralski silicon wafers,” *Phys. Status Solidi - Rapid Res. Lett.*, vol. 7, no. 9, pp. 616–618, 2013, doi: 10.1002/pssr.201308053.

[22] H. Mehrer, *Diffusion in Solids: Fundamentals, Methods, Materials, Diffusion-Controlled Processes*. Springer.

[23] C. T. J, *VLSI Technology*, 2nd ed. McGraw-Hill Book Co., 1988.

[24] B. Crowder, *Ion Implantation in Semiconductors and Other Materials*, 1st ed. Springer US, 1973.

[25] F. Cristiano, “Ion Implantation-Induced extended defects : structural investigations and impact on Ultra-Shallow Junction properties To cite this version : Habilitation à Diriger des Recherches Ion Implantation - Induced extended defects : structural investigations and ,” 2013.

[26] S. T. Dunham *et al.*, “Modeling of Dopant Diffusion in Silicon,” *IEICE Trans. Electron*, vol. E82-C, no. 6, pp. 800–812, 1999.

[27] *Athena User's Manual*, September. 2013.

[28] S. Guha, *Multijunction Solar Cells and Modules*. 2000.

[29] C. Chellaswamy and R. Ramesh, "An optimal parameter extraction and crack identification method for solar photovoltaic modules," *ARPN J. Eng. Appl. Sci.*, vol. 11, no. 24, pp. 14468–14481, 2016.

[30] "Double Diode Model." https://www.pveducation.org/pvcdrom/characterisation/double-diode-model.

[31] G. Kökbudak, E. Orhan, F. Es, E. Semiz, and R. Turan, "Optimization of Silicon Nitride (SiN X) Anti-reflective coating (arc) and passivation layers using industrial plasma enhanced chemical vapor deposition (pecvd) for perc type solar cells," *PVCon 2018 - Int. Conf. Photovolt. Sci. Technol.*, 2018, doi: 10.1109/PVCon.2018.8523918.

[32] R. A. Sinton and A. Cuevas, "Contactless determination of current-voltage characteristics and minority-carrier lifetimes in semiconductors from quasi-steady-state photoconductance data," *Appl. Phys. Lett.*, vol. 69, no. 17, pp. 2510–2512, 1996, doi: 10.1063/1.117723.

[33] E. Özmen, "Investigation of Screen-Printed and Evaporated Metal Contacts on Boron Implanted Emitter," Middle East Technical University, 2021.

[34] E. Özmen *et al.*, "Effect of Doping Profile on Contact Resistivty Between Screen Printed Ag/Al and Implanted Boron Emitter," *38th Eur. Photovolt. Sol. Energy Conf. Exhib.*, no. November, pp. 268–270, 2021, doi: 10.4229/EUPVSEC20212021-2CV.1.21.

[35] T. Dullweber and J. Schmidt, "Industrial Silicon Solar Cells Applying the Passivated Emitter and Rear Cell (PERC) Concept-A Review," *IEEE J. Photovoltaics*, vol. 6, no. 5, pp. 1366–1381, 2016, doi: 10.1109/JPHOTOV.2016.2571627.

[36] S. Dauwe, L. Mittelstädt, A. Metz, and R. Hezel, "Experimental evidence of parasitic shunting in silicon nitride rear surface passivated solar cells," *Prog. Photovoltaics Res. Appl.*, vol. 10, no. 4, pp. 271–278, 2002, doi: 10.1002/pip.420.

[37] A. Siddiqui, G. Bektaş, H. Nasser, R. Turan, and M. Usman, "Impact of Ion Implantation and Annealing Parameters on Bifacial Perc and Pert Solar Cell Performance," *Sustain. Energy Technol. Assessments*, vol. 53, no. July, 2022, doi: 10.1016/j.seta.2022.102583.

[38] G. Bektaş *et al.*, "Simplified process flow for the fabrication of PERC solar cells with ion implanted emitter," *Renew. Energy*, vol. 179, pp. 2295–2299, 2021, doi: 10.1016/j.renene.2021.08.054.

[39] J. Wu, Y. Liu, X. Wang, and G. Xing, "Application of ion implanted emitter

in PERC solar cells," *2015 IEEE 42nd Photovolt. Spec. Conf. PVSC 2015*, 2015, doi: 10.1109/PVSC.2015.7356046.

[40] Y. Hwang *et al.*, "Effect of laser damage etching on i-PERC solar cells," *Renew. Energy*, vol. 79, no. 1, pp. 131–134, 2015, doi: 10.1016/j.renene.2014.10.067.

[41] C. Kranz *et al.*, "Impact Of The Rear Surface Roughness On Industrial-Type Perc Solar Cells," pp. 557–560, doi: 10.4229/27thEUPVSEC2012-2AO.1.5.

[42] H. B. Tang, S. Ma, Y. Lv, Z. P. Li, and W. Z. Shen, "Optimization of rear surface roughness and metal grid design in industrial bifacial PERC solar cells," *Sol. Energy Mater. Sol. Cells*, vol. 216, no. July, 2020, doi: 10.1016/j.solmat.2020.110712.

[43] T. Dullweber, R. Hesse, V. Bhosle, and C. Dubé, "Ion-implanted PERC solar cells with Al2O3/SiN x rear passivation," *Energy Procedia*, vol. 38, pp. 430–435, 2013, doi: 10.1016/j.egypro.2013.07.300.

[44] N. Wöhrle *et al.*, "Industrial biperc solar cells with varied rear side characteristics under bifacial illumination," *35th EUPVSEC*, pp. 596–601, 2018.

[45] H. Asav, G. Bektas, A. E. Kececi, G. Kokbudak, B. Arikan, and R. Turan, "Comparative Evaluation of Rear Local Contact Patterns for P-Type Mono Crystalline Silicon PERC Solar Cell," *2020 2nd Int. Conf. Photovolt. Sci. Technol. PVCon 2020*, pp. 2020–2023, 2020, doi: 10.1109/PVCon51547.2020.9757782.

[46] S. Wilking, S. Ebert, A. Herguth, and G. Hahn, "Influence of hydrogen effusion from hydrogenated silicon nitride layers on the regeneration of boron-oxygen related defects in crystalline silicon," *J. Appl. Phys.*, vol. 114, no. 19, 2013, doi: 10.1063/1.4833243.

[47] R. Eberle, W. Kwapil, F. Schindler, S. W. Glunz, and M. C. Schubert, "Firing temperature profile impact on light induced degradation in multicrystalline silicon," *Energy Procedia*, vol. 124, pp. 712–717, 2017, doi: 10.1016/j.egypro.2017.09.082.

[48] C. Vargas *et al.*, "Carrier-Induced Degradation in Multicrystalline Silicon: Dependence on the Silicon Nitride Passivation Layer and Hydrogen Released during Firing," *IEEE J. Photovoltaics*, vol. 8, no. 2, pp. 413–420, 2018, doi: 10.1109/JPHOTOV.2017.2783851.

[49] J. Schmidt, B. Veith, F. Werner, D. Zielke, and R. Brendel, "Silicon surface passivation by ultrathin Al2O3 films and Al2O3/SiNx stacks," in *Conference Record of the IEEE Photovoltaic Specialists Conference*, 2010, pp. 885–890, doi: 10.1109/PVSC.2010.5614132.

[50] D. Chen *et al.*, "Hydrogen induced degradation: A possible mechanism for

light- and elevated temperature- induced degradation in n-type silicon," *Sol. Energy Mater. Sol. Cells*, vol. 185, pp. 174–182, 2018, doi: 10.1016/j.solmat.2018.05.034.

[51] Y. Wan, K. R. McIntosh, and A. F. Thomson, "Characterisation and optimisation of PECVD SiNx as an antireflection coating and passivation layer for silicon solar cells," *AIP Adv.*, vol. 3, no. 3, 2013, doi: 10.1063/1.4795108.

[52] S. Duttagupta, F. Lin, M. Wilson, M. Boreland, B. Hoex, and A. Aberle, "Extremely low surface recombination velocities on low-resistivity n-type and p-type crystalline silicon using dynamically deposited remote plasma silicon nitride film," *Prog. Photovolt Res. Appl.*, vol. 22, pp. 641–647, 2014, doi: 10.1002/pip.2320.

[53] G. Bektaş, A. E. Keçeci, S. Koçak Bütüner, and R. Turan, "Optimization of phosphorus implant dose and activation temperature for emitter formation of p-type silicon solar cells," in *38th European Photovoltaic Solar Energy Conference and Exhibition*, 2021, pp. 286–287, doi: 10.4229/EUPVSEC20212021-2CV.1.39.

[54] M. A. Green, "Recent Advances In Sılıcon Solar Cell Performance," in *10Th European Photovoltaic Solar Energy Conference &-12 April 1991 Lisbon, Portugal*, 1991, no. April, pp. 250–251.

[55] L. Tous *et al.*, "Evaluation of advanced p-PERL and n-PERT large area silicon solar cells with 20.5% energy conversion efficiencies," *Prog. Photovoltaics Res. Appl.*, vol. 23, no. 5, pp. 660–670, 2014, doi: doi.org/10.1002/pip.2478.

[56] J. Zhao, A. Wang, X. Dai, M. A. Green, and S. R. Wenham, "Improvements in Silicon Solar Cell Performance," in *The Conference Record of the Twenty-Second IEEE Photovoltaic Specialists Conference - 1991*, pp. 399–402, doi: 10.1109/PVSC.1991.169246.

[57] A. Cuevas, A. Luque, J. Eguren, and J. del Alamo, "50 Per cent more output power from an albedo-collecting flat panel using bifacial solar cells," *Sol. Energy*, vol. 29, no. 5, pp. 419–420, 1982, doi: 10.1016/0038-092X(82)90078-0.

[58] S. Guo, T. M. Walsh, and M. Peters, "Vertically mounted bifacial photovoltaic modules: A global analysis," *Energy*, vol. 61, pp. 447–454, 2013, doi: 10.1016/j.energy.2013.08.040.

[59] A. Abdallah, D. Martinez, B. Figgis, and O. El Daif, "Performance of Silicon Heterojunction Photovoltaic modules in Qatar climatic conditions," *Renew. Energy*, vol. 97, pp. 860–865, 2016, doi: 10.1016/j.renene.2016.06.044.

[60] H. B. Tang, S. Ma, Y. Lv, Z. P. Li, and W. Z. Shen, "Solar Energy Materials and Solar Cells Optimization of rear surface roughness and metal grid design

in industrial bifacial PERC solar cells," vol. 216, no. July, 2020, doi: 10.1016/j.solmat.2020.110712.

[61] M. H. Saw, Y. S. Khoo, J. P. Singh, and Y. Wang, "Enhancing optical performance of bifacial PV modules," *Energy Procedia*, vol. 124, pp. 484–494, 2017, doi: 10.1016/j.egypro.2017.09.285.

[62] T. C. R. Russell, R. Saive, A. Augusto, S. G. Bowden, and H. A. Atwater, "The Influence of Spectral Albedo on Bifacial Solar Cells: A Theoretical and Experimental Study," *IEEE J. Photovoltaics*, vol. 7, no. 6, pp. 1611–1618, 2017, doi: 10.1109/JPHOTOV.2017.2756068.

[63] N. Wehmeier *et al.*, "21.0%-efficient screen-printed n-PERT back-junction silicon solar cell with plasma-deposited boron diffusion source," *Sol. Energy Mater. Sol. Cells*, vol. 158, pp. 50–54, 2016, doi: 10.1016/j.solmat.2016.05.054.

[64] G. Von Gastrow *et al.*, "Recombination processes in passivated boron-implanted black silicon emitters," *J. Appl. Phys.*, vol. 121, no. 18, 2017, doi: 10.1063/1.4983297.

[65] Y. Li, H. Shen, Z. Hou, Q. Wei, Z. C. Ni, and D. Hu, "Formation of emitter by boron spin-on doping from SiO2 nanosphere and properties of the related n-PERT solar cells," *Sol. Energy*, vol. 225, no. July, pp. 317–322, 2021, doi: 10.1016/j.solener.2021.07.033.

[66] H. Huang *et al.*, "Effective passivation of p+ and n+ emitters using SiO2/Al2O3/SiNx stacks: Surface passivation mechanisms and application to industrial p-PERT bifacial Si solar cells," *Sol. Energy Mater. Sol. Cells*, vol. 186, no. 123, pp. 356–364, 2018, doi: 10.1016/j.solmat.2018.07.007.

[67] S. Yamaguchi *et al.*, " Effects of SiN x refractive index and SiO 2 thickness on polarization-type potential-induced degradation in front-emitter n-type crystalline-silicon photovoltaic cell modules ," *Energy Sci. Eng.*, no. January, 2022, doi: 10.1002/ese3.1135.

[68] Q. Wei, S. Zhang, S. Yu, J. Lu, W. Lian, and Z. Ni, "High efficiency n-PERT solar cells by B/P co-diffusion method," *Energy Procedia*, vol. 124, pp. 700–705, 2017, doi: 10.1016/j.egypro.2017.09.345.

[69] B. Yu *et al.*, "Impact of Boron Doping Concentration on Tunnel Oxide Passivated Contact in Front Surface for N-Type Poly-Si Based Passivated Contact Bifacial Solar Cells," *IEEE J. Photovoltaics*, pp. 1–9, 2022, doi: 10.1109/JPHOTOV.2022.3151328.

[70] Z. W. Peng, T. Buck, L. J. Koduvelikulathu, V. D. Mihailetchi, and R. Kopecek, "Industrial Screen-Printed n-PERT-RJ Solar Cells: Efficiencies beyond 22% and Open-Circuit Voltages Approaching 700 mV," *IEEE J. Photovoltaics*, vol. 9, no. 5, pp. 1166–1174, 2019, doi:

10.1109/JPHOTOV.2019.2919117.

[71] W. Luo *et al.*, “Investigation of potential-induced degradation in n-PERT bifacial silicon photovoltaic modules with a glass/glass structure,” *IEEE J. Photovoltaics*, vol. 8, no. 1, pp. 16–22, 2018, doi: 10.1109/JPHOTOV.2017.2762587.

[72] J. Shi *et al.*, “Mass production and modeling of high efficiency n-PERT solar cells with ion implanted BSF/selective-BSF,” *Sol. Energy*, vol. 142, pp. 87–90, 2017, doi: 10.1016/j.solener.2016.11.043.

[73] R. C. G. Naber *et al.*, “N-Pert Solar Cells With Passivated Contact Technology Based on Lpcvd Polysilicon and Fire-Through Contact Metallization,” *32nd Eur. Photovolt. Sol. Energy Conf. Exhib.*, vol. 1, no. June, pp. 430–433, 2016.

[74] B. Mojrová, C. Comparotto, R. Kopecek, and V. D. Mihailetchi, “Optimization of Boron Diffusion for Screen Printed n-PERT Solar Cells,” *Energy Procedia*, vol. 92, pp. 474–478, 2016, doi: 10.1016/j.egypro.2016.07.129.

[75] D. A. R. Barkhouse, O. Gunawan, T. Gokmen, T. K. Todorov, and D. B. Mitzi, “Yield predictions for photovoltaic power plants:empirical validation,recent advances and remaining uncertainties,” *Prog. Photovoltaics Res. Appl.*, vol. 20, no. 1, pp. 6–11, 2015, doi: 10.1002/pip.

[76] S. Singh *et al.*, “Large area co-plated bifacial n-PERT cells with polysilicon passivating contacts on both sides,” *Prog. Photovoltaics Res. Appl.*, no. July 2021, pp. 1–11, 2022, doi: 10.1002/pip.3548.

[77] Z. W. Peng, M. Nakahara, T. Buck, and R. Kopecek, “Towards 22% efficiency n -PERT rear junction solar cells with screen printed Al point back contact,” *AIP Conf. Proc.*, vol. 1999, no. August 2018, 2018, doi: 10.1063/1.5049309.

[78] A. B *et al.*, “Emerging frontiers of N-Type silicon material for photovoltaic applications: The impurity-defect interactions,” *Front. Nanosci. Nanotechnol.*, vol. 1, no. 1, pp. 2–12, 2015, doi: 10.15761/fnn.1000102.

[79] N. L. Chang, M. Wright, R. Egan, and B. Hallam, “The Technical and Economic Viability of Replacing n-type with p-type Wafers for Silicon Heterojunction Solar Cells,” *Cell Reports Phys. Sci.*, vol. 1, no. 6, p. 100069, 2020, doi: 10.1016/j.xcrp.2020.100069.

[80] VDMA, “Update ITRPV 2020 Results 2019 including maturity report 2020.” 2020.

[81] J. Krugener *et al.*, “Electrical and structural analysis of crystal defects after high-temperature rapid thermal annealing of highly boron ion-implanted emitters,” *IEEE J. Photovoltaics*, vol. 5, no. 1, pp. 166–173, 2015, doi:

10.1109/JPHOTOV.2014.2365468.

[82] H. Boo *et al.*, “Effect of high-temperature annealing on ion-implanted silicon solar cells,” *Int. J. Photoenergy*, vol. 2012, 2012, doi: 10.1155/2012/921908.

[83] A. Lanterne, J. Le Perchec, S. Gall, M. Coig, A. Tauzin, and Y. Veschetti, “20.5% efficiency on large area N-type PERT cells by ion implantation,” *Energy Procedia*, vol. 55, pp. 437–443, 2014, doi: 10.1016/j.egypro.2014.08.006.

[84] F. Kiefer *et al.*, “Bifacial, fully screen-printed n-PERT solar cells with BF2 and B implanted emitters,” *Sol. Energy Mater. Sol. Cells*, vol. 157, pp. 326–330, 2016, doi: 10.1016/j.solmat.2016.05.028.

[85] A. Youssef *et al.*, “Tabula Rasa for n - Cz silicon - based photovoltaics,” no. July, pp. 1–8, 2018, doi: 10.1002/pip.3068.

[86] C. Chan *et al.*, “Instability of Increased Contact Resistance in Silicon Solar Cells Following Post-Firing Thermal Processes,” *Sol. RRL*, vol. 1, no. 11, pp. 3–7, 2017, doi: 10.1002/solr.201700129.

[87] P. Hamer *et al.*, “Hydrogen induced contact resistance in PERC solar cells,” *Sol. Energy Mater. Sol. Cells*, vol. 184, no. April, pp. 91–97, 2018, doi: 10.1016/j.solmat.2018.04.036.

[88] L. Helmich, D. C. Walter, D. Bredemeier, and J. Schmidt, “Atomic-Layer-Deposited Al2O3 as Effective Barrier against the Diffusion of Hydrogen from SiNx:H Layers into Crystalline Silicon during Rapid Thermal Annealing,” *Phys. Status Solidi - Rapid Res. Lett.*, vol. 14, no. 12, pp. 1–5, 2020, doi: 10.1002/pssr.202000367.

[89] S. Koçak Bütüner *et al.*, “Effect of surface morphology on passivation quality of Al2O3/SiNx stack layer for PERC solar cell,” in *38th European Photovoltaic Solar Energy Conference and Exhibition*, 2021, pp. 291–292, doi: 10.4229/EUPVSEC20212021-2CV.1.42.

[90] G. Bektaş *et al.*, “Comparison of Electrical Performances of Fully Ion Implanted n-PERT Solar Cells Made of Different n-Type Wafer Feedstocks,” in *38th European Photovoltaic Solar Energy Conference and Exhibition*, 2021, pp. 281–282, doi: 10.4229/EUPVSEC20212021-2CV.1.35.

[91] R. J. Schwartz and M. . Lammert, “Silicon solar cells for high concentration applications,” in *1975 International Electron Devices Meeting*, 1975, pp. 350–352, doi: 10.1109/IEDM.1975.188896.

[92] R. J. Schwartz and M. . Lammert, “The interdigitated back contact solar cell:silicon solar cell for use in concentrated sunlight,” in *IEEE Transactions on Electron Devices*, 1977, pp. 337–342, doi: 10.1109/T-ED.1977.18738.

[93] E. Van Kerschaver and G. Beaucarne, “Back-contact solar cells: a review,”

Prog. Photovoltaics Res. Appl., vol. 14, no. 2, 2005, [Online]. Available: https://doi.org/10.1002/pip.657.

[94] I. Cesar *et al.*, “Mercury: A back junction back contact front floating emitter cell with novel design for high efficiency and simplified processing,” *Energy Procedia*, vol. 55, no. 0, pp. 633–642, 2014, doi: 10.1016/j.egypro.2014.08.037.

[95] D. Inns, “Understanding Metal Induced Recombination Losses in Silicon Solar Cells with Screen Printed Silver Contacts,” *Energy Procedia*, vol. 98, pp. 23–29, 2016, doi: 10.1016/j.egypro.2016.10.077.

CURRICULUM VITAE

PERSONAL INFORMATION

Surname, Name: Bektaş, Gence
Nationality: Turkish (TC)
Date and Place of Birth: 12 March 1988, Şabanözü
email: gencebektas@gmail.com

EDUCATION

Degree	Institution	Year of Graduation
MS	METU Micro and Nanotechnology	2017
BS	METU Department of Physics	2011
High School	Aydınlıkevler High School, Ankara	2005

WORK EXPERIENCE

Year	Place	Enrollment
2021-Present	ODTÜ-GÜNAM	Lead Researcher
2020-Present	ODTÜ	Lecturer
2018-2020	ODTÜ	Scientific Research Specialist
2012-2014	MEGETEK	Integrated Logistics Support Specialist

FOREIGN LANGUAGES

Advanced English

PUBLICATIONS

1. N. Dasilva-Villanueva, B. Arıkan, H.H. Canar, D.F. Marrón, B.-K. Hong, A.E. Keçeci, S. Koçak Bütüner, G. Bektaş, R. Turan, and del C. Carlos, "High carrier lifetimes in UMG multicrystalline wafers after P-diffusion compatible with high-efficiency cell structures", submitted for publication.

2. A. Siddiqui, G. Bektaş, H. Nasser, R. Turan, and M. Usman, "Impact of Ion Implantation and Annealing Parameters on Bifacial Perc and Pert Solar Cell Performance," *Sustain. Energy Technol. Assessments*, vol. 53, 2022, doi: 10.1016/j.seta.2022.102583.

3. G. Bektaş, G. Kökbudak, A.E. Keçeci, S.K. Bütüner, H. Asav, E.H. Çiftpınar, H.H. Canar, B. Arıkan, and R. Turan, "Simplified process flow for the fabrication of PERC solar cells with ion implanted emitter," *Renew. Energy*, vol. 179, pp. 2295–2299, 2021.

4. G. Bektaş, H.H. Canar, A.E. Keçeci, H. Asav, S. Seyrek, S. Koçak Bütüner, R. Turan, "Optimization of Front and Rear Surface Dielectric Passivation Layers For Ion Implanted PERC Solar Cells," submitted for publication in *AIP Conference Proceedings*.

5. G. Bektaş, E.H. Çiftpınar, S.K. Bütüner, A.E. Keçeci, H.H. Canar, G. Kökbudak, H. Asav, and R. Turan, "Effect of Implanted Phosphorus Profile on the iVoc Variations During the Firing Process of n-type Si," accepted for publication in *AIP Conference Proceedings*.

6. H. Asav, G. Bektaş, A. E. Kececi, G. Kokbudak, B. Arikan, and R. Turan, "Comparative Evaluation of Rear Local Contact Patterns for P-Type Mono Crystalline Silicon PERC Solar Cell," *2020 2nd Int. Conf. Photovolt. Sci. Technol. PVCon 2020*, pp. 2020–2023, 2020.

7. G. Bektaş, H. Asav, H.H. Canar, O. Aydin, A.E. Keçeci, S. Ozdemir, S. Koçak Bütüner, S. Seyrek, F. Es, and R. Turan, "Comparison of Electrical Performances of Fully Ion Implanted n-PERT Solar Cells Made of Different n-Type Wafer Feedstocks," in *38th Eur. Photovolt. Sol. Energy Conf. Exhib.* (2021), pp. 281–282

8. E. Özmen, S. Seyrek, G. Bektaş, H.H. Canar, S. Koçak Bütüner, H. Asav, A.E. Keçeci, and R. Turan, "Effect of Doping Profile on Contact Resistivty Between Screen Printed Ag/Al and Implanted Boron Emitter," 38th Eur. Photovolt. Sol. Energy Conf. Exhib. 268 (2021).

9. A.E. Keçeci, G. Bektaş, E.H. Çiftpınar, S. Koçak Bütüner, H. Asav, G. Kökbudak, H.H. Canar, B. Arıkan, and R. Turan, “Performance Enhancement of PERC Solar Cell with SiOxNy Back Surface Passivation by Low Temperature Annealing Process,” in *38th Eur. Photovolt. Sol. Energy Conf. Exhib.* (2021), pp. 257–260.

10. S. Koçak Bütüner, G. Bektaş, G. Kökbudak, M. Borra Zolfaghari, H. Asav, A.E. Keçeci, B. Arıkan, and R. Turan, “Effect of surface morphology on passivation quality of Al2O3/SiNx stack layer for PERC solar cell,” in *38th Eur. Photovolt. Sol. Energy Conf. Exhib.* (2021), pp. 291–292.

11. H. Asav, A.E. Keçeci, G. Bektaş, S. Koçak Bütüner, G. Kökbudak, H.H. Canar, B. Arıkan, and R. Turan, “Selective Emitter Formation via Laser Doping With Picosecond Pulsed Laser For High-Efficiency PERC Solar Cells,” in *38th Eur. Photovolt. Sol. Energy Conf. Exhib.* (2021), pp. 271–273.